AN ABSTRACT OF THE THESIS OF

Aaron Jesse Fillo for the degree of Master of Science in Mechanical Engineering presented on December 2, 2016

Title: The Global Consumption Speeds of Premixed Large-Hydrocarbon Fuel/Air Turbulent Bunsen Flames

Abstract approved: _____

David L. Blunck

Large-hydrocarbon fuels are used for ground and air transportation because of their high energy-density and will be for the foreseeable future. However, combustion of large-hydrocarbon fuels in a turbulent environment is poorly understood and difficult to predict. The turbulent flame speed, which is the velocity at which a flame front propagates through a turbulent fuel and air mixture, is a key property in turbulent combustion. The turbulent flame speed can be used as a model input parameter for turbulent combustion simulations. However, turbulent flame speeds for large-hydrocarbon fuels are largely unknown. These values are needed to improve combustion models and enhance understanding of the physics and chemistry that control turbulent combustion of large-hydrocarbon fuels.

The objective of this study is to measure the turbulent flame speed of large-hydrocarbon fuels and to identify key physics in the turbulent combustion of these fuels. This is motivated by the use of the turbulent flame speeds in modeling combustion in practical devices and the significant use of large-hydrocarbons in these devices. This research has broad implications for society and industry; both the Federal Aviation Administration and gas turbine engine companies have called for research on the turbulent flame speeds of large-hydrocarbon fuels.

The turbulent flame speed in this work is defined as the global consumption speed, and is measured for three fuels on a turbulent Bunsen burner. The Reynolds number,

Abstract (Continued)

turbulence intensity, preheat temperature, and equivalent ratio can be independently controlled using the burner. A conventional Jet-A fuel, known as A2, is used as a reference because of its common use in commercial and military aviation. A2 is compared to bi-modal and quadra-modal blends referred to as C1 and C5, respectively. These fuels are selected as they have similar heat releases and laminar flame speeds. Time-averaged line of site images of OH*, CH*, and CO_2* chemiluminescence are used to determine an the average flame front area. This flame area is used to determine the global consumption speed. The global consumption speed is measured for Reynolds number and equivalence ratio ranging between 5.000-10.000 and 0.7-1, respectively. Turbulence intensities are varied between 10% and 20% of the bulk flow velocity.

The global consumption speed increases with turbulence intensity and Reynolds number for all fuels. Global consumption speeds for A2 and C5 match within 5% at all conditions. Conversely, the global consumption speed of C1 is up to 22% lower than A2 or C5. These results indicate the global consumption speed is sensitive to turbulent velocity fluctuations, bulk flow velocity, and fuel chemistry. These results together suggest the global consumption speed is additionally sensitive to flame stretch.

Dimensional analysis is used to isolate and identify sensitivities of the global consumption speed to turbulent velocity fluctuations, bulk flow velocity, global stretch rate, and fuel chemistry. A clear sensitivity to fuel chemistry is observed and is affected by aromatic and alkane content. A2 and C5 have higher global consumptions speeds and increased stability; these fuels have shorter average hydrocarbon chain lengths and higher aromatic content than C1. In addition, the global consumption speed is highly sensitive to turbulence intensity of the flow; the turbulent flame speed increases an average of 30% for all fuels between the minimum and maximum turbulence intensity cases. Results are attributed to a strong sensitivity of the global consumption speed to flame stretch and a strong coupling of turbulence and fuel chemistry effects. These conclusions agree with the available literature and provide a foundational understanding of the sensitivities of the global consumption speed for large-hydrocarbon fuels.

The Global Consumption Speeds of Premixed Large-Hydrocarbon Fuel/Air
Turbulent Bunsen Flames

by
Aaron Jesse Fillo

A THESIS

Submitted to

Oregon State University

in partial fulfillment of
the requirements for the
degree of

Master of Science

Presented December 2, 2016
Commencement June 2017

Master of Science thesis of <u>Aaron Jesse Fillo</u> presented on <u>December 2, 2016.</u>

APPROVED:

_____

Major Professor, representing Mechanical Engineering

_____

Head of the School of Mechanical, Industrial, and Manufacturing Engineering

_____

Dean of the Graduate School

I understand that my thesis will become part of the permanent collection of Oregon State University libraries. My signature below authorizes release of my thesis to any reader upon request.

_____

Aaron Jesse Fillo, Author

ACKNOWLEDGEMENTS

I would like to thank Dr. Tim Lieuwen and colleagues for the burner specifications; Dr. Scott Stouffer (University of Dayton Research Institute) and the Air Force Research Laboratory (AFRL) for the vaporizer design; Dr. Tim Edwards from AFRL for supplying the fuel samples of Jet-A, C1, and C5; Dr. Hai Wang and Rui Xu for sharing the HyChem mechanisms; and Dr. Fokion N. Egolfopoulos for sharing experimental validation result for laminar flame speeds. Dr. David Blunck, thank you for giving me an opportunity to join the CIRE Lab, and thank you for helping to guide me through the trials and tribulations of graduate school.

To my colleagues in the CIRE Lab, thank you for your friendship and support. To Jonathan Bonebrake, thank you for assisting with data collection and thank you for banging your head against this wall of research along with me; I could not have broken through without you. To Mick Carter, Morgan Mayer, Bruck Sameshima, and Ian Walters thank you for for assistance with data collection and maintenance. To Joshua Ray Allen, and Bradley Anderson thank you for your assistance with fabrication and assembly.

To my friends and family thank you for being patient with me. I would rather have been with you than working. To my wife Alex, you have been my partner though this challenging process and I cannot thank you enough. To Drs. Joshua Gess, Kyle Niemeyer, and Bryony DuPont, thank you for pointing out that even if this thesis is never read, anything worth doing is worth doing right. To my dad, and Robin thank you for proof reading this mess.

Finally, to the Farrands, Katie, Josh, Chloe, and Peter. You four have always let me ramble on about science and engineering but never let it go to my head. Peter and Chloe, you helped teach me how to teach, there is no better gift you could have given me. Thank you all. . .

TABLE OF CONTENTS

TABLE OF CONTENTS (Continued)

LIST OF FIGURES

LIST OF FIGURES (Continued)

LIST OF TABLES

LIST OF SYMBOLS

Roman Symbols

S_L	Laminar Flame Speed	m/s
S_T	Turbulent Flame Speed	m/s
$\dot{m}'''$	Volumetric Mass Consumption Rate	kg/(s $-$ m^3)
$\dot{m}''$	Mass Flow per Unit Area	kg/(s $-$ m^2)
$\dot{m}''$	Mass Flow Rate	kg/s
T	Temperature	K
P	Pressure	atm
Y	Mass Fraction	kg/kg
D	Molecular Diffusivity	m^2/s
t	time	s
U	Velocity; Uncertainty	m/s; Of Value
u'	Fluctuating Velocity	m/s
I_0	Stretch Factor	s^{-1}
A	Flame Area	m^2
$v_{s,tangential}$	Local Velocity Tangential to Flame	m/s
V_f	Instantaneous Local Displacement Speed	m/s
w	Mean Instantaneous Velocity	m/s
n	Unit Normal Vector	m
R_f	Radius at the flame base	m
l	Characteristic Length Scale	m
l_T	Taylor Length Scale	m
c	Progress Variable Contour	Unitless
f	Focal-Ratio	Dimensionless
Le	Lewis Number	Dimensionless
I	Turbulence Intensity	Dimensionless
Re	Reynolds Number	Dimensionless
Ka	Karlovitz Number	Dimensionless

LIST OF SYMBOLS (Continued)

Greek Symbols

α	Thermal Diffusivity; Half Flame Angle	m^2/s; rad
ρ	Density	kg/m^3
ν	Oxidizer-fuel Mass Ratio; Kinematic Viscosity	kg/kg; m^2/s
ϕ	Equivalence Ratio	Dimensionless
δ_L	Flame Thickness	m
κ	Stretch Rate	s^{-1}
Σ	Flamelet surface area per unit volume	m^{-1}
τ	Characteristic Time Scale	s
∇	Lagrangian Operator	

Subscripts

u	Unburned Gasses	
b	Burned Gasses	
F	Fuel	
$flame$	Flame	
$flow$	Unburned Flow	
B	Bias Uncertainty	
P	Precision Uncertainty	
$Inst.$	Instrumentation	
$Img.$	Imaging	
$Pilot$	Pilot Flame	
D	Nominal Burner Diameter	12 mm
$adiabatic$	Adiabatic Reaction Assumption	
max	Max Stretch Condition	
0	Zero Stretch or Bulk referencer	
rms	Root Mean Square	
LC	Local Consumption	
LD	Local Displacement	
GC	Global Consumption	
GD	Global Displacement	
$\langle c \rangle$	Derived from Progress Variable Contour	

Other Notation

$\overline{(\ )}$ Average Over Reaction Zone

$\langle\ \rangle$ Vector Quantity

For Mom and Kevy...

"I may not have gone where I intended to go, but I think I have ended up where I needed to be."

Douglas Adams

Chapter 1

Introduction

In 2014 the United States consumed 18.49 million barrels of oil a day, 70 percent of which was used in transportation [1]. Reducing this dependence on fossil fuel technologies is critical to the nation's security, economic stability, and environmental stewardship. Oil is a politically volatile, increasingly scarce resource that releases greenhouse gases when combusted and, as a result, is not sustainable at its current rate of consumption.

Reactions in internal combustion and gas turbine engines operate at elevated temperatures and pressures, and are primarily driven by turbulent premixed and partially premixed combustion of hydrocarbon fuels [2]. Current estimates suggest there is nearly one passenger car per individual living in the United States. This statistic excludes delivery, public transit, and emergency vehicles as well as air and water transport vehicles [3]. These vehicles use large-hydrocarbon liquid fuels such as gasoline, diesel, and jet fuel and will for the foreseeable future.

Fuel energy density (energy content per unit mass) is a major concern in combustor design for aircraft as excess weight and volume is detrimental to aircraft performance [4, 5]. Large-hydrocarbon fuels, which are nominally liquid at room temperature and have a carbon number of 6 or greater, are typically used in transportation because they have a high energy density relative to gaseous and electric alternatives. For example, $1\,L$ of jet fuel contains approximately $43\,MJ$ of energy; to get the same energy content, an equivalent amount of methane or lithium ion batteries would take up $1500\,L$ and $2500\,L$, respectively [2]. Despite this common use, current understanding of the turbulent combustion of these fuels in modern internal combustion and gas turbine engines is limited. As a result, it is difficult or impossible to predict combustion performance

in practical engines. This inability to predict combustion performance can result in hundreds of millions of dollars in losses in certification and development of new engines [5].

To decrease fossil fuel consumption, an improved understanding of the fundamental physics governing the turbulent combustion of transportation fuels is needed. Such an understanding can be used to provide much needed improvement to the accuracy of models used in the development of internal combustion [6] and gas turbine engines [7] and would help transform the combustion industry. This improved understanding would enable optimization of next-generation engines to maximize power output while reducing emissions and fuel consumption.

The turbulent flame speed is the rate at which a flame front propagates in an unburned turbulent fuel-air mixture [2]. This measure is important to the fidelity of combustion models used in engine design and provides a means of directly analyzing and comparing fuels. However, turbulent flame speeds for most large-hydrocarbon fuels are not known. Thus, an accurate understanding of turbulent flame speeds is required to help overcome current challenges present in engine design.

1.1 Motivations

An improved understanding of the turbulent combustion of large-hydrocarbon fuels used in transportation technologies is currently needed. This is motivated by the significance of the turbulent flame speeds in evaluating combustion models, and the ubiquity of large-hydrocarbon fuels. These motivations can be summarized as a need to:

- Develop a repository of turbulent flame speeds for liquid transportation fuels to provide much needed validation and improvement to existing models;

- Formulate a model for turbulent flame speed based on variable turbulence intensity, fuel chemistry, and inlet conditions;

- Establish a standard methodology for analysis of alternative liquid transportation fuels to help reduce fossil fuel consumption.

This research has broad implications for society and industry. Both the Federal Aviation Administration (FAA) and gas turbine engine companies have expressed significant

interest in maximizing engine performance through an improved understanding of turbulent combustion phenomena.

1.2   Research Objectives

The main objective of this effort is to measure the global consumption speed of large-hydrocarbon liquid fuels and identify the fundamental physics that govern their turbulent combustion. More specifically, this study will focus on these four objectives:

1. Identify the effects of turbulence intensity on the turbulent global consumption speed of conventional jet fuels and experimental fuel blends.

2. Identify the effects of bulk fluid velocity on the turbulent global consumption speed of large-hydrocarbon fuels.

3. Identify how different hydrocarbon classes affect the turbulent global consumption speed of large-hydrocarbon fuels.

4. Identify sensitivities of the global consumption speed to flame stretch and diffusion phenomena.

1.3   Outline of Thesis

This document presents an experimental investigation and analysis of the fundamental sensitivities of the turbulent global consumption speed of large-hydrocarbon fuels. An in-depth review of relevant literature will be presented in Chapter 2. This chapter begins with a summary of relevant laminar flame studies. Next, a discussion of turbulent flame definitions and relevant scaling techniques will be presented. Finally, a review of similar global consumption speed studies will be provided to highlight current theories in the field.

Chapter 3 will present the experimental and data processing techniques used in the analysis of the global consumption speed for the premixed turbulent Bunsen flames examined in this study. This chapter will begin with a brief discussion of the definition of the turbulent flame speed used in this study. Next, the Bunsen burner design, image processing technique, and selected fuels will be presented. A discussion of the uncertainty

prorogation in these methods will follow. The chapter will conclude with a discussion of the governing assumptions of this technique as well as a summary of its limitations.

Chapter 4 will provide a summary of the results. This chapter will begin with a discussion of the laminar flame speeds for the three fuel studied. The global consumption speed results will then be presented and discussed. With these results as a reference, the results of dimensional scaling analysis will be presented with an in-depth discussion of their significance relative to the available literature.

Chapter 5 will present the conclusions of this work, and discuss their context within the reviewed literature. Finally, Chapter 6 will discuss potential future studies motivated by these conclusions.

Chapter 2

Review of Literature

There are numerous empirical and numerical studies investigating the laminar and turbulent flame speeds of fuels relevant to transportation and power conversion. Historically, most studies have focused on the laminar combustion of gaseous or neat large-hydrocarbon fuels. Gaseous fuels, such as sin gas and natural gas, are used in power and propulsion systems and their simplified chemistry is empirically and numerically accessible. Although valuable, these studies fail to capture the complex turbulent-chemistry interactions present in practical combustors. As a result, the turbulent combustion which occurs in many practical combustion devices is poorly understood. Moreover, few studies on the turbulent combustion of real jet fuels exist. An understanding of these interactions is needed to help improve development of next-generation internal combustion and gas turbine combustors that use these fuels.

This chapter will review the available literature pertaining to the turbulent flame speed of large-hydrocarbon fuels. Section 2.1 will review fundamental laminar flamed speed theory and relevant laminar flame speed studies as a foundation for further discussion. Section 2.2 will begin with a discussion of the four definitions of the turbulent flame speed, their applications, and experimental accessibility. Following this background information, several empirical and numerical studies of the turbulent flame speed of gaseous fuels will be reviewed. This is done to highlight relevant turbulent-chemistry effects that may be present in the combustion of larger fuels. Finally, a review of empirical and numerical studies of the turbulent flame speed of liquid jet fuels will be presented, with special emphasis placed on the global consumption speed.

2.1 Laminar Flame Speed

The laminar flame speed can be defined as the rate of consumption of reactants through a reaction front under laminar flow conditions [8]. This fundamental characteristic of combustion provides the basis for much of turbulent flame speed theory. There are at least four experimental means of determining the laminar flame speed: Bunsen flame methods, flat and one-dimensional flame methods, spherical expanding flame methods, and stagnation flame methods; more detail on the application of these methods may be found in Reference [2]. Modern computing techniques based on empirical fits to laminar burning parameters have made numerical tools for determine laminar flame speeds, such as CHEMKIN and Cantera are widely accessible. Despite these advances in computational techniques, no general analytical model for determining laminar or turbulent flame speeds has been developed.

2.1.1 Laminar Flame Speed Theory

Spalding's first principles approach can be used to understand fundamental laminar flame speed theory. Spalding's approach provides this simplified equation for the flame speed in one-dimensional flow,

$$S_L = \left[-2\alpha(\nu+1)\frac{\overline{\dot{m}}_F'''}{\rho_u} \right]^{1/2}, \tag{2.1}$$

where S_L is the laminar flame speed, α is the thermal diffusivity, ν is the oxidiser-fuel mass ratio, $\overline{\dot{m}}_F'''$ is the volumetric mass consumption rate, and ρ_u is the density of the unburned mixture [9]. It should be noted that the one-dimensional approximation in this approach is highly idealized. $\overline{\dot{m}}_F'''$ is sensitive to three dimensional effects such as the spacial temperature gradient across the reaction zone; as a result, it is typically empirically determined, limiting the applicability of this approach [8].

Despite these limitations, this theoretical model provides a strong foundation for discussion as it demonstrates that the flame speed is primarily a function of the state properties of the unburned and burned gases, mass flux of the reactants, fuel-air ratio, and the fuel mass consumption rate:

$$S_L = f\left(T_u, T_b, P, \dot{m}'', \nu, \frac{dY_F}{dt}\right), \tag{2.2}$$

where T_u, T_b, and P are the unburned temperature, burned temperature, and pressure, respectively; $\dot{m}''$ is the reactant mass flux; ν is the fuel-air ratio; and $\frac{dY_F}{dt}$ is the fuel mass consumption rate. This functional understanding of the laminar flame speed will provide the basis for discussion in this section.

2.1.2 Relevant Laminar Flame Speed Literature

The laminar flame speed of transportation fuels is commonly used to determine sensitivities of combustion parameters to fuel chemistry, while avoiding the complexities associated with turbulence [10]. For example, Kumar et al. [11] investigated atmospheric laminar flame speeds and activation energies of iso-octane and n-heptane for both pure and N_2 diluted fuel-air mixtures. Data was collected using a counter-flow burner with digital particle imaging velocimitry (DPIV) at atmospheric pressure and temperatures ranging from 298–470 K. Experimental results were compared against zero and one dimensional combustion calculations using PREMIX [12] in conjunction with CHEMKIN [13] and TRANSPORT [14]. Iso-octane combustion had a consistently lower flame speed relative to n-heptane combustion for the full range of preheat temperatures investigated, while n-heptane combustion demonstrated an increased stability at the lean extinction limits. Numerical analysis revealed n-heptane had a higher mass burning flux and lower activation energy for all preheat temperatures and equivalence ratios examined. This higher relative reactivity was proposed as the source of the laminar flame speed and stability trends and was attributed to differences in the C2-C3 chemistry between the two fuels. To validate this theory, Kumar et al. [11] performed a sensitivity analysis of the reaction pathways for n-heptane and iso-octane combustion. This analysis demonstrated that n-heptane combustion produces a radical pool dominated by large concentrations of ethylene, whereas iso-octane produces a radical pool with little ethylene but large concentrations of propene, iso-butene, and methyl radicals; these results are further reinforced by related studies on n-heptane and iso-octane oxidation [11, 15–18]. These differences in C2-C3 chemistry were present throughout all test conditions, indicating a fundamental difference in the oxidation chemistry of these two fuels.

Expanding their investigation, Kumar et al. [19] found a strong sensitivity of the laminar flame speed to fuel chemistry for real multi-component fuel blends (i.e. fuels in practical use). The study investigated the laminar flame speeds and extinction limits of three conventional and alternative fuels including Jet-A, S-8 (a synthetic jet-fuel), and pure n-decane. Jet-A and S-8 demonstrated similar propagation characteristics, but significant

differences in extinction limits. S-8 provided a more stable flame that was less susceptible to stretch-induced blow off. This stability was attributed to higher alkane content. These results are reinforced when comparing the n-decane results with those of n-heptane and iso-octane in [11]. The laminar flame speed of n-decane is higher than that of n-heptane or iso-octane in all cases; this further reinforces the laminar flame speed is sensitive to fuel reactivity. Kumar et al. [19] concluded that the laminar flame speed of the Jet-A and S-B blends seem to be the result of an aggregate effect of the flame speeds of their components; in other words, the laminar flame speed is sensitive to fuel composition.

Similar analysis by Hui et al. [20] measured the laminar flame speeds and extinction stretch rates of n-propylbenzene (n-PB), 1,2,4-trimethylbenzene (1,2,4-TMB), 1,3,5-trimethylbenzene (1,3,5-TMB), and toluene, at atmospheric pressure and a temperature range of 400–470 K. This study used the same counter-flow burner, DPIV experimental apparatus, and PREMIX, CHEMKIN, and TRANSPORT calculations as previous work by Kumar et al. [19]. The n-PB was found to have the highest laminar flame speed and greatest stability over the range of test conditions followed by toluene and TMBs. This indicates that the laminar flame speed is highly sensitive to aromatic species content; the measured flame speeds of n-PB were 30 % greater at an equivalence ratio of unity than the TMBs. These results were attributed to a sensitivity of chain-branching and heat-release reactions to radical formation in combustion initiation. This result is important and indicates that similar fuels (i.e. different aromatics with similar chemical structure) can have significant differences in reactivity, flame speed, and stretch-rate based on seemingly minor chemical differences. Each of the fuels tested have the same benzene ring structure bonded with methyl groups, but different numbers and locations for these methyl groups. Finally, this result indicates the extinction stretch rate and laminar flame speed are sensitive to fuel reactivity.

Continuing this work, Hui et al. [4] measured the laminar flame speed of ten transportation relevant fuels: n-decane, n-dodecane, iso-octane, toluene, n-PB, 1,2,4-TMB, and 1,3,5-TMB, conventional Jet-A (labeled as POSF-4658), synthetic S-8 (labeled as POSF-4734), and a four-component Jet-A surrogate composed of n-dodecane, iso-octane, n-PB, and 1,3,5-TMB [4]. Tests were conducted using the same high pressure counter-flow DPIV burner as in previous studies for equivalence ratios, pre-heat temperatures, and pressures of ϕ =0.7-1.3, T_u =350–470 K, and P =1–3 atm, respectively. The objective of this study was to evaluate how well surrogate fuels are able to replicate the premixed combustion characteristics of their target fuel, in this case Jet-A. Their results indicated that the laminar flame speed of transportation fuels decreases with decreasing

reactivity and diffusivity of the fuel [4]. The measured laminar flame speed of n-decane was greater than n-dodecane; this was attributed to a decrease in the diffusivity of larger carbon chain species. In addition, the measured flame speeds for different species decreased in the following order: n-decane (n-alkane), n-dodecane (n-alkane), iso-octane (iso-alkane), toluene (aromatic). Finally, the laminar flame speed was found to decrease with increasing aromatic carbon content. This reinforces previous results by Hui et al. [20] where the laminar flame speeds of selected aromatic hydrocarbons at atmospheric pressures decreased with increasing carbon content.

The trends found by Hui et al. [4, 20], fit well with accepted fuel class reactivity trends as outlined in [2], where reaction rates increase with carbon chain length, and reactivity of species classes decrease in the following order: n-alkanes, iso-alkanes, cyclo-alkanes, alkenes, and aromatics. Comparing the laminar flame speeds of Jet-A and its surrogates with neat fuel results indicates that the laminar flame speeds of blended fuels are bounded by the flame speeds of n-alkanes on the upper limit and aromatics on the lower limit. This result is important as it suggests a sensitivity of the laminar flame speed to fuel composition; real fuels and surrogate blends with higher concentrations of n-alkanes demonstrate faster flame speeds than high aromatic content fuels. This result supports the theory that the laminar flame speed is highly sensitive to fuel composition.

In each of the studies reviewed, the laminar flame speed and flame stability were sensitive to fuel composition and reactivity; higher flame speeds and increased stability were measured for fuels with longer average hydrocarbon chain lengths and higher alkane content [4, 11, 19, 20]. These results were attributed to differences in the radical pool formed during combustion of hydrocarbon fuels primarily in the C1, C2, and C3 carbon chain size range. As summarized by Law [2], until recently the combustion community has assumed that differences in the base C1, C2, and C3 chemistry for hydrocarbon fuels were insignificant. As a result, conventional chemical kinetic mechanisms have been generated assuming similar radical formation across a wide range of fuels and validated by matching empirical burning parameters. However, the studies reviewed above suggest that radical formation during the combustion initiation and chain-branching reactions are highly sensitive to the fuel class and carbon content [4, 11, 19, 20]. This is important as it indicates that the laminar flame speeds and stretch rates for transportation fuels have a sensitivity to fuel composition. This discovery has implications on turbulent flame studies where multi-dimensional effects such as stretch cannot be neglected. Furthermore, it calls for careful application of laminar flame theory in the analysis and dimensional scaling of turbulent flame speed results.

2.2 Turbulent Flame Speed

The turbulent flame speed, similar to the laminar flame speed, is the rate of consumption of reactants through a flame front but under turbulent flow conditions. The turbulent flame speed is a metric for assessing the effects of turbulent fluctuations, molecular transport, and fuel chemistry on turbulent combustion [21]. Numerous studies have attempted to correlate the turbulent flame speed to the zero-stretch laminar flame speed and the root mean square of the turbulent velocity fluctuations as,

$$S_T = S_{L,0} \cdot f(u'_{rms}), \tag{2.3}$$

where S_T is the turbulent speed, $S_{L,0}$ is the zero-stretch laminar flame speed, and u'_{rms} is the velocity fluctuation term, f is some unknown function. However, these quantities alone do not fully capture the fundamental physics and chemistry present in turbulent reactions and no universal correlation or theory has been developed for the turbulent flame speed [22].

2.2.1 Turbulent Flame Speed Definitions

Four definitions of the turbulent flame speed have been proposed in the literature: local displacement speed ($S_{T,LD}$), global displacement speed ($S_{T,GD}$), local consumption speed ($S_{T,LC}$), and global consumption speed ($S_{T,GC}$) [22–25]. Displacement and consumption refer to the propagation of the flame front and consumption of reactants (mass burning flux), respectively. The local displacement and consumption speeds attempt to quantify flame propagation and reactant consumption locally on the flame front per unit volume. These quantities are challenging to obtain experimentally because the relevant time and length scales are typically on the order of Taylor or Kolmogorov length-scales, requiring advanced imaging equipment to capture [26]. For reference the definition for the local consumption speed is

$$S_{T,LC} = S_{L,0} I_0 \int_{-\infty}^{\infty} \Sigma d\eta, \tag{2.4}$$

where I_0 and Σ are the stretch factor and the flamelet surface area per unit volume, respectively [22]. The surface area is integrated along the path of η, over the flame brush, in the direction normal to the reaction surface [2, 27]. This approach is experimentally inaccessible and analytically intensive making it difficult to implement. As demonstrated by Cheng et al. [28] the local displacement speed is similarly intensive in its application.

The challenges associated with local flame speed measurements can be avoided through calculation of global burning velocities, assuming that all reactants flow through the flame brush [2, 22]. Like local methods, global measures of the turbulent flame speed are definition dependent; for example, the global consumption speed represents a temporally and spatially averaged measure of reactant consumption through the flame brush. It is defined as

$$S_{T,GC} = \frac{\dot{m}_R}{\rho_R \overline{A}_{\langle c \rangle}}, \tag{2.5}$$

where $\dot{m}_R$, ρ_R, and $\overline{A}_{\langle c \rangle}$ are the mass flow rate of the reactants, the density of the reactants, and the mean flame area corresponding to the contour $\langle c \rangle$, respectively [22–24]. The contour $\langle c \rangle$ corresponds to the progress variable, c, which is a measure of reactant consumption through the flame brush. Here $\langle c \rangle = 0$ and $\langle c \rangle = 1$ are the unburned and burned faces of the flame brush respectively [29]. The reduced complexity of global definitions comes at the cost of averaging over potentially large variations in local burning rates where the flame front is spatially evolving, such as in a Bunsen or spherically expanding flame where turbulence is not stationary [22]. These limitations are acceptable for practical applications as these global consumption speeds are used as initial boundary conditions for combustor simulations [6, 7]. Additional information and discussion on these measures including the local and global displacement speeds may be found in References [22–25, 30] and the sources cited therein.

2.2.2 Dimensional Analysis of Turbulent Flames

Dimensional analysis, or the Buckingham Pi theorem, is a mathematical means of reducing the number and complexity of variables that affect a physical phenomenon [31]. This is done by scaling parameters of interest (e.g. turbulent flame speed, S_T; or flame stretch, κ) with well understood values (temperature, T; pressure, P; laminar flame speed, S_L) in order to generate non-dimensional variables and systematically reduce the volume of data needed for analysis. A challenge in the analysis of turbulent flame speed data is a lack of consistency in definitions and scaling parameters used in its analysis [22]. However, for such analyses to be compared, scaling parameters must be well understood and consistent.

Typical scaling parameters attempt to simplify analysis by eliminating secondary effects. As a result, scaling parameters are often determined at limiting cases where secondary effects are minimized [31]. For example, the max-stretch laminar flame speed ($S_{L,max}$) is often used for scaling chemistry effects in turbulent flames and is determined at the

extinction stretch limits of a flame [32]. However, chemical kinetic models are validated over limited ranges of temperature, pressure, and flow conditions. As a result, the uncertainties associated with extrapolating values outside of these ranges are large, such as in the max-stretch case [2, 32, 33]. Similarly, flow time and length parameters are most commonly scaled relative to the bulk flow, integral, or Taylor scales. However, there is limited agreement on which scales are most relevant to turbulent combustion and when they should be applied [34].

Despite a wide range of studies on turbulent flame speed, structure, stability, and transport such as those reported in [22, 32, 35–47], there is little agreement on what scaling parameters are relevant to turbulent flame analysis and how those parameters should be determined.

Figure 2.1 presents a Borgi regime diagram as an example of how dimensional scaling is used. In Figure 2.1 the x-axis (l/δ_L) represents a non-dimensional length scale for local fluctuations in the flame front and the y-axis (u'/S_L) represents a non-dimensional velocity fluctuation for the flame [26].
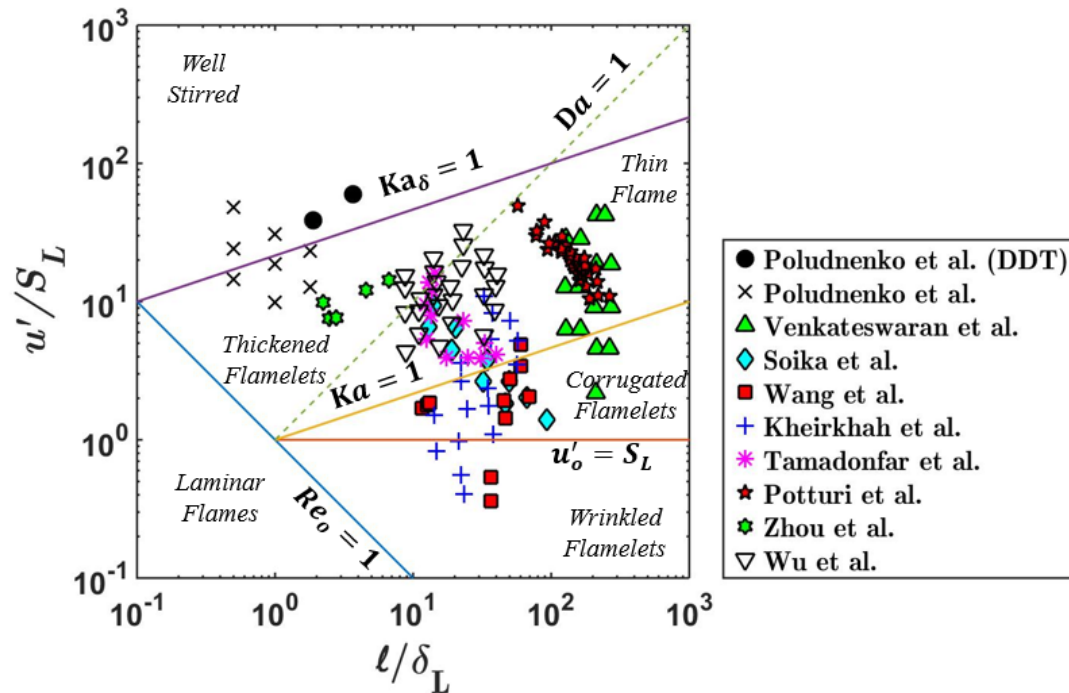
FIGURE 2.1: Borgi diagram of relevant turbulent flame studies

It is important to note that each of the studies in Figure 2.1 follows reasonable conventions and represent a meaningful contribution to the combustion field; however, of the nine research groups and fifteen studies cited in Figure 2.1, each study uses different non-dimensionalization for the x and y-axes of their own regime diagrams. In generating this diagram I attempted to consistently normalize these values in order to allow a direct comparison of the data across these studies. In doing so, I approximated the uncertainties associated with normalizing the values in Figure 2.1 by applying similar uncertainty analysis to that in Reference [32]. The results of this uncertainty analysis are total uncertainties of plus or minus an order of magnitude. The lack of consistency in the selected scaling values makes comparison between studies challenging, and highlights the need for consistent approaches in defining, generating, and applying dimensional scaling parameters to turbulent flame speed results. Thus, care must be taken in comparing relevant literature.

Further emphasising the need for robust scaling parameters to enable identification of key physics, Venkateswaran et al. [32] attempted to collapse a range of turbulent flame speed data from several studies by implementing a leading-point scaling analysis. The data scaled by the max stretch laminar flame speed ($S_{L,max}$) were found to collapse for constant-pressure conditions, but not for data where pressure was varied. This was attributed to a non-quasi-steady effect that suggested pressure effects influence the turbulent burning velocity by altering how well the flames chemistry can track the time-varying stretch rate at the leading point [32]. If this theory is true, it indicates a strong coupling effects for flame stretch and pressure.

In attempting to determine adequate chemical and flow time scales by which to elucidate the nature of these non-steady effects, Venkatswaren et al. [32] highlighted two key concerns in the application of these approaches. First, developing chemical scaling parameters from chemical kinetic models is prone to large uncertainty, which may adversely affect scaling results. Second, there is little agreement on what flow time and length scales are most relevant for turbulent flame speed analysis. The authors suggest that a wide range of fuel composition and pressure data can be correlated with the max-stretch laminar flame speed ($S_{L,max}$), but state that due to uncertainty, additional data is needed before firm conclusions may be drawn. This result highlights the limitations of current scaling approaches.

Based on the results of Venkateswaran et al. [32] and other similar studies, Verma et al. [30] pose the question, "Does sensitivity of measured scaling exponents for turbulent

burning velocity to flame configuration prove a lack of generality of the notion of turbulent burning velocity?" The authors cite several studies of turbulent flame speed which use the full range of different definitions and scaling parameters discussed previously as a basis for this question. A detailed discussion of these differences may be found in References [24, 30, 32, 42, 47–58] and the sources cited therein. In an effort to answer their own question, Verma et al. [30] investigated if the turbulent flame speed is a fundamental combustion characteristic when defined with any of the four accepted definitions discussed previously. To do this, Verma et al. [30] performed Reynolds averaged Navier-Stokes (RANS) simulations to determine values for global displacement and consumption speeds. Both wire-stabilized and rim-stabilized Bunsen flame geometries were investigated for fuel/air mixtures and flow conditions matching those in previous experimental studies as cited previously. Turbulent global consumption and displacement speed results were fit to power-law curves and compared with previous experimental results, with special care taken to understand the statistical significance of the data scatter.

Verma et al. [30] concluded by answering "no" to the titular question, indicating that the apparent scatter in the data does not prove or disprove the notion that the turbulent flame speed is a fundamental combustion characteristic, and called for further investigation. With this call for further investigation Verma et al. [30] state that their results strongly indicate that turbulent flame speed is definition and geometry specific; i.e., data can only be compared meaningfully between matching definitions and burner geometries. This result is important as it restricts the number of studies between which meaningful comparison can be made.

Venkateswaran et al. [32] tabulated several databases of turbulent flame speed values along with their corresponding burner configurations and turbulent flame speed definitions; see Table 2.1.

TABLE 2.1: Summary of Turbulent Flame Speed databases

Database	Configuration	Definition
Georgia Tech [22, 32, 37, 59]	Bunsen	Global Consumption, $S_{T,GC}$
PSI [51, 52]	Bunsen	Global Consumption, $S_{T,GC}$
Kobayashi et al. [29, 48, 60, 61]	Bunsen	Global Consumption, $S_{T,GC}$
Kido et al. [62]	Spherical bomb	Global Consumption, $S_{T,GC}$
Nakahara et al. [63]	Spherical bomb	Global Consumption, $S_{T,GC}$
Kitagawa et al. [64]	Spherical bomb	Global Consumption, $S_{T,GC}$
LSB [24, 28, 65]	Low Swirl Burner	Local Displacement, $S_{T,LD}$

Each of the studies in Table 2.1 represent a contribution to the turbulent flame speed research as well as a significant database of available results. However, based on the conclusions of Venkateswaran et al. [32], Verma et al. [30], and my own attempts to normalize data between disparate studies, only the first three databases listed in Table 2.1 will be reviewed in this document. These three databases use the same burner configuration and flame speed definition as this study; thus, their turbulent global consumption speeds can be directly compared to those measured here. The remainder of this review will focus on these References [22, 29, 32, 37, 48, 51, 52, 59–61, 66].

2.2.3 Turbulent Flame Speed of Gaseous Fuels

The turbulent consumption speed has been extensively studied for gaseous fuels as highlighted in Table 2.1 [22, 29, 32, 37, 48, 51, 52, 59–61, 66]. For example, work by Venkateswaran et al. [22] measured the global consumption speeds of premixed methane and H_2/CO (Syngas) fuel blends of 30 %, 50 %, 70 %, and 90 % H_2 by weight at atmospheric conditions on a piloted turbulent Bunsen burner [22]. These mixtures had matched zero-stretched laminar flame speeds and different Lewis numbers. The global consumption speed was found to increase with increased turbulence intensity and decrease proportionally with weight percent of H_2. Methane/air flames had the lowest observed flame speeds. This result suggests the global consumption speed is sensitive to fuel composition. This sensitivity was attributed to preferential diffusion effects as the Lewis number ($Le = \alpha/D$) of the H_2/CO was less than unity, indicating a high molecular diffusivity. This result agrees with work done by Hui et al. [4] on laminar flames, which demonstrated a decrease in laminar flame speed with decreasing diffusivity of the fuel. Moreover, this study measured a significant difference in turbulent flame speed for 90 % H_2 fuel blends relative to other fuels with similar laminar flame speeds. This indicates that classic correlations between laminar flame speed and turbulence intensity (non-dimensional velocity fluctuations, $I = u'_{rms}/U_0$) can be insufficient for correlating the turbulent flame speed.

Further work by Venkateswaran et al. [37] on the turbulent flame speeds of H_2/CO fuel blends at pressures of 1–20 atm confirmed that different fuels with equivalent unstretched laminar flame speeds had different turbulent flame speeds. Using the same piloted turbulent Bunsen burner, Venkateswaran et al. [37] measured the global consumption speed for H_2/CO fuel blends of 30 %, 50 %, 70 %, and 90 % H_2 by weight with matched un-stretched laminar flame speeds. The global consumption speed for these

H_2/CO fuel blends was found to decrease with decreasing Lewis number and pressure. The results further demonstrated that classical correlations of the turbulent flame speed as simply a function of turbulence intensity are insufficient ($S_{T,GC}/S_{L,0} = f(u'_{rms}/U_0)$). Moreover, this result is important as it illustrates that secondary Lewis number effects can be significant, and confirms observed pressure effects [19, 29, 60].

Attempting to determine a correlation for the global consumption speed, Venkateswaran et al. [37] found that their constant pressure global consumption speed data could be correlated to max-stretch laminar flame speeds ($S_{L,max}$) derived from quasi-steady leading point models. This correlation was found to collapse the data over a range of fuel compositions, but not when pressure was varied.

The quasi-steady assumption is a standard procedure in chemical kinetics that is applied when intermediate species have a production or consumption rate such that it can be assumed as constant. However, as demonstrated by Venkateswaran et al. in [66], a factor of ten increase in pressure results in a similar reduction in chemical time scale for some intermediate reactions. This reduction in chemical time scales invalidates the quasi-steady assumption at elevated pressures. Moreover, since the max-stretch laminar flame speed models used by Venkateswaran et al. [37] require that the quasi-steady assumption holds, the correlation to $S_{L,max}$ breaks down when pressure is increased. This is a limitation to the scaling technique; it is plausible that an improved non-quasi-steady model for $S_{L,max}$ would provide a consistent correlation across a wide range of pressure. Venkateswaran et al. [37] concluded by stating that this limitation of the scaling approach indicates that pressure effects can significantly alter the degree of non-quasi-steadiness in the internal structure of the flames leading point for turbulent Bunsen flames.

Venkateswaran et al. [32, 59] continued their efforts to determine a correlation for global consumption speed by accounting for non-quasi-stead effects such that

$$S_{T,GC}/S_{L,max} = f\left(\frac{\langle u'_{rms} \rangle_{LP}}{S_{L,max}}, \frac{\tau_{S_{L,Max}}}{\tau_{flow}} \right), \tag{2.6}$$

where $\tau_{S_{L,Max}}$ and τ_{flow} are the chemical time scale associated with the leading point and the characteristic velocity of the flow, respectively. The addition of a chemical and flow time scale does achieve a collapse of the data over a wider range of pressures than in previous studies. These results indicate a coupling between pressure effects and turbulence; this coupling is attributed to a sensitivity of the global consumption speed to flame stretch rate. This suggests that for highly stretch-sensitive flames, where

$S_{L,max}/S_{L,0} \gg 1$, non-quasi-steady pressure effects can alter how turbulence affects the flame front, which may significantly alter the burning velocity of the leading point. Alternatively, this indicates that non-quasi-steady effects should have less of an effect on flames with a weak stretch sensitivity, where $S_{L,max}/S_{L,0}$ 1. This result is important as it indicates that pressure and stretch effects cannot be neglected.

Kobayashi et al. [29] measured the global consumption speeds of methane/air flames with a piloted turbulent Bunsen burner at pressures up to $3.0\,\text{MPa}$. Similar to results by Venkateswarna et al. [22], the global consumption speed was found to increase with increasing turbulence intensity. Additionally, the global consumption speed and instantaneous flame area were greater and more sensitive to turbulence intensity at elevated pressures [29]. As with the work performed by Venkatswaren et al. [32], these pressure sensitivities were attributed to non-quasi-steady chemistry effects. Kobayashi et al. [29] proposed that local hydrodynamic instabilities (i.e., increased wrinkling) caused by a decrease of thermal-diffusive effects at elevated pressures may present a physical analog to these chemistry effects. In premixed flames, Darrieus-Landau hydrodynamic instabilities — caused by sudden changes in density across the flame front — can lead to flame wrinkling; however, thermal-diffusion typically serves to transfer heat across these small instabilities, equalizing the local density differential. Kobayashi et al. [29] hypothesized that thermal-diffusion effects weaken with increased pressure, resulting in relatively stronger hydrodynamic instabilities and increased flame wrinkling. If true, this theory would explain why the global consumption speed becomes more sensitive to turbulence intensity with increased pressure.

Kobayashi et al. [60] continued their work by measuring the global consumption speeds of methane, ethylene, and propane on the same piloted Bunsen burner. In comparing the global consumption speeds of these three fuels, Kobayashi et al. [60] observed that propane had a lower global consumption speed and a reduced sensitivity to non-quasi-steady effects and hydrodynamic instabilities at increased pressures relative to other fuels [60]. This result was attributed to the lower rate of molecular diffusion for propane relative to methane or ethylene, resulting in a Lewis number closer to one. This result supports similar findings by Hui et al. [4] and Venkateswaran et al. [22] that both the laminar and turbulent flame speeds decrease with decreased molecular diffusion.

Continuing their focus on high pressure effects, Kobayashi et al. [48, 61] observed finer, more convoluted flame structures as the result of increased pressure for methane/air flames. As in previous studies, these pressure effects were linked to an increase in the sensitivity of the global consumption speed to turbulence intensity at increased pressure.

This physical change in the flame structure corresponds to the theory presented by Venkatswaren et al. [32] that pressure alters how well the flame chemistry can track the time-varying stretch rate at the leading point. The non-quasi-steady chemistry effects theorized by Venkateswaran et al. [32] could plausibly alter the local thermal and molecular diffusion characteristics in the flame front. This change could cause a greater sensitivity to Darrieus-Landau hydrodynamic instabilities and result in greater flame stretch [29]. This result is important as it highlights a sensitivity of the global consumption speed to fuel composition and flame stretch.

Daniele et al. [51, 52] measured the global consumption speed of syngas on a piloted, turbulent Bunsen burner at gas turbine-relevant conditions (i.e., inlet temperatures and velocities up to $773\,\mathrm{K}$ and $150\,\mathrm{m\,s^{-1}}$) and pressures up to $2.0\,\mathrm{MPa}$. This work observed the same preferential diffusion and hydrodynamic instability effects as Venkateswaran et al. [22] and Kobayashi et al. [29]. As a result, this study is valuable as an independent validation of these observations and supports their corresponding theories.

In each of the studies reviewed herein, a sensitivity of the global consumption speed to turbulence intensity was observed [22, 29, 51]. This sensitivity has also been found to increase with an increase in pressure [32, 48, 51, 61]. This additional pressure sensitivity is attributed to non-quasi-steady chemistry effects, which alter how well the flames chemistry can track the time-varying stretch rate at the leading point [32]. As a result, these pressure effects demonstrate an increased formation of Darrieus-Landau hydrodynamic instabilities [29, 48, 51, 60, 61]. This result is important and indicates that complex interactions between turbulence and chemistry phenomena can affect the turbulent flame speed. Additional bulk chemistry sensitivities have been observed and are attributed to differences in both molecular and thermal transport. [22, 29, 32]. These chemistry and pressure effects suggest the global consumption speed is sensitive to fuel chemistry, and will be further investigated in this document.

2.2.4   Turbulent Flame Speed of Large-Hydrocarbon Fuels

Limited data has been reported for the turbulent flame speeds of large-hydrocarbon fuels (i.e., liquid at room temperature). Goh et al. [67] measured turbulent consumption speeds for JP-10/air mixtures at $473\,\mathrm{K}$ and atmospheric pressure for a range of $\phi = 0.2$ to 0.8 on a twin-flame opposed-flow burner. They reported turbulent flame velocities with respect to experimentally determined axial root mean square (rms) velocity fluctuations and Damköhler number. These results suggest turbulent flame speed is sensitive to

fluctuating turbulent time and length scales. However, the published rang of data is small and further investigation is needed to confirm the observed trends. In addition, these results were completed on a twin opposed flame burner using a global displacement speed definition for the turbulent flame speed. As a result, care must be taken comparing this work by Goh et al. [67] to previously presented studies because the geometry and turbulent flame speed definitions are different.

In another study investigating large-hydrocarbon fuels, Won et al. [21] measured the turbulent burning velocities of n-heptane/air mixtures using a Reactor Assisted Turbulent Slot (RATS) burner. The study demonstrated that the turbulent flame speed is sensitive to low-temperature chemistry by varying the preheat temperature while holding flow velocity constant. The study also observed that the turbulent flame speed is sensitive to pre-flame oxidation which altered fuel chemistry and transport properties. This result indicates that the turbulent flame speed is sensitive to fuel chemistry and can be applied to a wide range of studies since they are independent of geometry and flame speed definition, as the low temperature effects are determined upstream of the burner.

In summary, sensitivities of the global consumption speed to turbulence intensity, pressure, preferential diffusion, and fuel chemistry have been well documented in the presented literature [21, 22, 32, 51, 60]. These sensitivities are attributed to coupled turbulence and chemistry effects resulting in increased flame stretch rates [32, 48]. This literature will provide the basis for further discussion in this document.

Chapter 3

Experimental Methods

This chapter will discuss the experimental methods used for measuring the global consumption speed of large-hydrocarbon fuels in this study. Large-hydrocarbon fuels are defined as having carbon numbers greater than 6 and are nominally liquid at room temperature. The global consumption speeds are determined from non-intrusive line-of-sight chemiluminescence images of radicals in a piloted turbulent Bunsen burner flame. A time-averaged flame area is determined from OH*, CH*, and CO_2* chemiluminescence from the reaction front; this area is then used to determine the global consumption speed ($S_{T,GC}$). As stated in equation (2.5), and reiterated here, the global consumption speed is defined as

$$S_{T,GC} = \frac{\dot{m}_R}{\rho_R \overline{A}_{\langle c \rangle}},\tag{3.1}$$

where $\dot{m}_R$, ρ_R, and $\overline{A}_{\langle c \rangle}$ are the mass flow rate of the reactants, the density of the reactants, and the mean flame area corresponding to the contour $\langle c \rangle$, respectively [22–24]. There are several advantages to using a Bunsen burner configuration in this study: experimental accessibility, and a wide variety of available data on similar geometries for benchmarking and comparison, such as the extensive gaseous fuel data sets from Kobayashi et al. and Venkatswaren et al. [22, 29, 32, 37, 48, 59–61].

This chapter will present the experimental approach and facilities, turbulence characterization, image processing techniques, fuel selection, and sensitivity and uncertainty analyses employed in this study. The chapter will conclude with a discussion of the governing assumptions and limitations of this analysis method.

3.1 Experimental Approach and Facilities

Premixed, vaporized, large-hydrocarbon fuels are burned on a piloted turbulent Bunsen burner in this study. A schematic of the vaporizer and burner system used for generating the flames is presented in Figure 3.1. A detailed plumbing and instrumentation diagram, electrical schematic, and bill of materials for the experimental apparatus may be found in Appendix A. In this system pre-heated air and room temperature large-hydrocarbon fuel are injected into a highly turbulent vaporizer. Well mixed air and vaporized fuel then pass through a series of flow conditioners and a calibrated turbulence generator prior to exiting the burner nozzle. The fuel/air mixture is then ignited by a methane/air pilot flame and imaged with a UV camera. This section will discuss each of these steps in turn and conclude with a summary of the experimental conditions studied.

The piloted turbulent Bunsen burner configuration used in this study matches a similar apparatus for gaseous fuels at Georgia Institute of Technology [22]. The engineering drawings and specifications for the nozzle and plenum of this apparatus were shared with me and used in the development of the experimental apparatus discussed herein.

The burner is designed to allow Reynolds number, turbulence intensity, and temperature of the flow to be independently controlled [22]. The burner consists of a smooth contoured nozzle tapering down from 76 mm to 12 mm diameter at the exit. It is designed to reduce boundary-layer growth in the nozzle and achieve a top-hat velocity profile at the exit [22]. An annular sinter plate, with a 20 μm nominal pore size, is positioned around the burner outlet and anchors a premixed methane/air pilot flame. The methane pilot flame operates at an equivalence ratio of unity; the total mass flow does not exceed ~10 % of the main mass flow rate and results in less than a 5 % uncertainty in the turbulent flame speed for the measured conditions. A discussion of this uncertainty analysis is presented in section 3.6. The primary fuel-air mixture passes through a layer of ball bearings upon entering the burner to prevent jetting from the smaller diameter feed-lines and encourage uniform flow development [22]. The flow then passes through a 130 mm development length to ensure it is well mixed and has a uniform temperature and velocity distribution. A type-K thermocouple is used to monitor the final unburned temperature of the reactant flow (450 K) in this development length and has a total uncertainty of 2 % of the set point temperature.

The vaporizer premixes and vaporizes the large-hydrocarbon fuels. The mixing occurs ~1.3 m upstream of the burner outlet which ensures the reactants are well-mixed. The vaporizer design replicates a system developed by the Air Force Research Laboratory

[68]. Pre-heated air (i.e., 473 K) and room-temperature fuel are injected in a solid-cone spray using an air-assisted atomizing nozzle. Additional preheated air is injected into the vaporizer through an annular manifold positioned around the fuel nozzle. The manifold creates a high velocity heated air-curtain around the fuel injection site, encouraging turbulent mixing and preventing fuel from contacting the heated vaporizer walls. The main air flow is systematically heated to the desired set point temperature of 473 K using a series of tube heaters with PID temperature controllers prior to injection into the vaporizer. After mixing and vaporization the fuel/air mixture is maintained at a constant 473 K with an uncertainty of 2 % of the set point value. Care is taken to keep the air temperature below auto-ignition temperatures at all times for safety, and to minimize any fuel cracking that may occur.
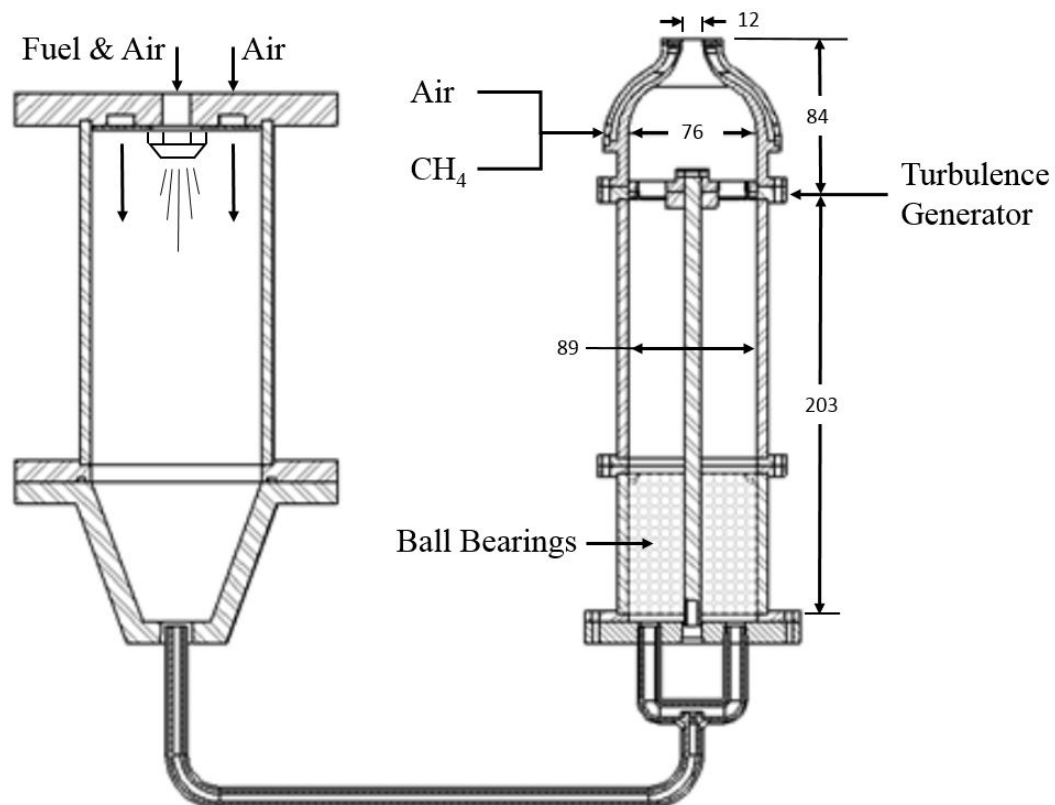
FIGURE 3.1: Schematic of the vaporizer and burner system. All dimensions in mm.

The air flow rates for both the pilot and main flames are metered upstream of the vaporizer and pre-heaters using rotameters with 3 % and 2 % full scale accuracy, respectively. Pressure transducers with 2 % full scale accuracy and type-K thermocouples with 2 % full scale accuracy are used to determine the density of the fuel/air mixture after

heating and vaporization. An additional pressure correction is applied to the primary air flow rotameter; the outlet pressure of this instrument is nominally 34.5 kPa above atmosphere and must be corrected to account for compressibility effects through the rotameter. The mass flow rate of the methane pilot fuel is metered directly using a MKS thermal mass flow controller with a full-scale accuracy of 1 %. The main fuel flowrate is metered volumetrically using duel syringe-pumps with an accuracy of 0.5 % of the set point value. As a result the uncertainty of the equivalence ratios for the pilot and main flows are below 3 % and 5 %, respectively. The total mass flow uncertainty of the pilot methane/air mixture is below 3 %. A detailed discussion of uncertainty propagation and total uncertainty is provided in section 3.6.

The turbulence intensity is controlled independently of the bulk fluid velocity using a turbulence generator developed by Venkatswaren et al. [22, 37]. As shown in Figure 3.1, the turbulence generator is located 84 mm upstream of the burner outlet and consists of a 3 mm thick bottom plate that is bolted to the plenum and a 6 mm thick top plate attached to a central shaft that extends out the bottom of the plenum. Flow straighteners are fixed to both the top and bottom plates and extend into the annular openings in the adjacent plate as shown in Figure 3.2. This geometry minimizes swirl that may develop in the flow at high blockage ratios. The turbulence intensity at the exit of the burner is proportional to the top plate's annular position (i.e. blockage ratio). A high contrast top-down photo of the plates' positions is taken to determine the blockage ratio. The image is then binarized and the blockage ratio is determined. Using this blockage-ratio the turbulence intensities are estimated based on turbulence calibration data reported by Venkateswaran et al. [22, 37] for the same burner geometry.

(a) (b)
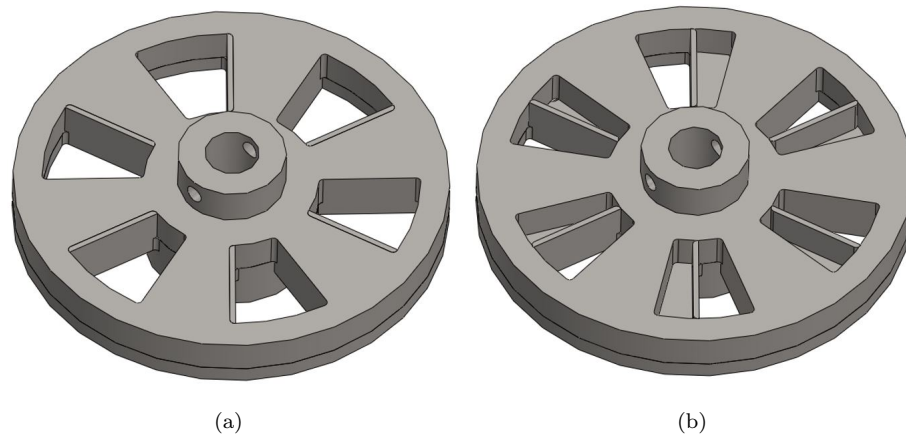
FIGURE 3.2: Schematic of turbulence generator, (a) Fully Open, (b) Partially Closed.

Venkatswaren et al. [22] thoroughly validated the turbulence generation of this geometry. Moreover, since this experimental apparatus was CNC-cut using the original designs presented by Venkateswaran et al. [22], the burner dimensions match within the tolerance of the CNC machine (<0.0001 in). This careful replication of the experimental apparatus developed by Venkatswaren et al. [22] indicates the turbulent statistics of the two experimental apparatus should match. Thus, the turbulence intensities determined from blockage ratio have an uncertainty of $\sim 10\%$ of the value as reported by Venkatswaren et al. [22]. Additional discussion on turbulence validation and uncertainty may be found in sections 3.2 and 3.6.

Turbulent consumption speeds were collected for three large-hydrocarbon fuels for a range of operating conditions. Reynolds number and turbulence intensities were independently varied from 5.000 to 10.000 and for 10% and 20% of the bulk flow velocity, respectively. All tests were repeated for a range of equivalence ratios from 0.7-1 at atmospheric conditions with an outlet temperature of ~ 450 K. These operating conditions and the detailed experimental operating procedure can be found in Appendix D.

3.2   Turbulence characterization

Venkateswaran et al. [22] and Marshall et al. [69] conducted a thorough and exhaustive characterization of the turbulent statistics of this Bunsen burner and turbulence generator configuration. Marshall et al. [69] provided a summary of this analysis and presented turbulence intensity at the centerline of the burner exit plane against relative to turbulence generator blockage ratio. Turbulence intensity increases monotonically with blockage ratio; this trend is consistent over a wide range of temperatures, pressures, and bulk flow velocities. These turbulence statistics provide the turbulence intensity values used in this study and are assumed to have an uncertainty of $\sim 10\%$. The turbulence intensities reported here correspond to the minimum and maximum blockage ratios as calibrated by Marshall et al. [69].

A brief validation of the burner bulk and fluctuating axial velocity profiles was conducted using single component hot-wire anemometery for Reynolds numbers of 10.000, 7.500, and 5.000, to confirm agreement with the flow geometry observed by Marshall et al. [22, 69]. The results of this validation are presented in Figure 3.3, and demonstrate good agreement with results presented by Marshall et al. [69] (black line). No additional turbulence characterization was completed due to constrained resources.
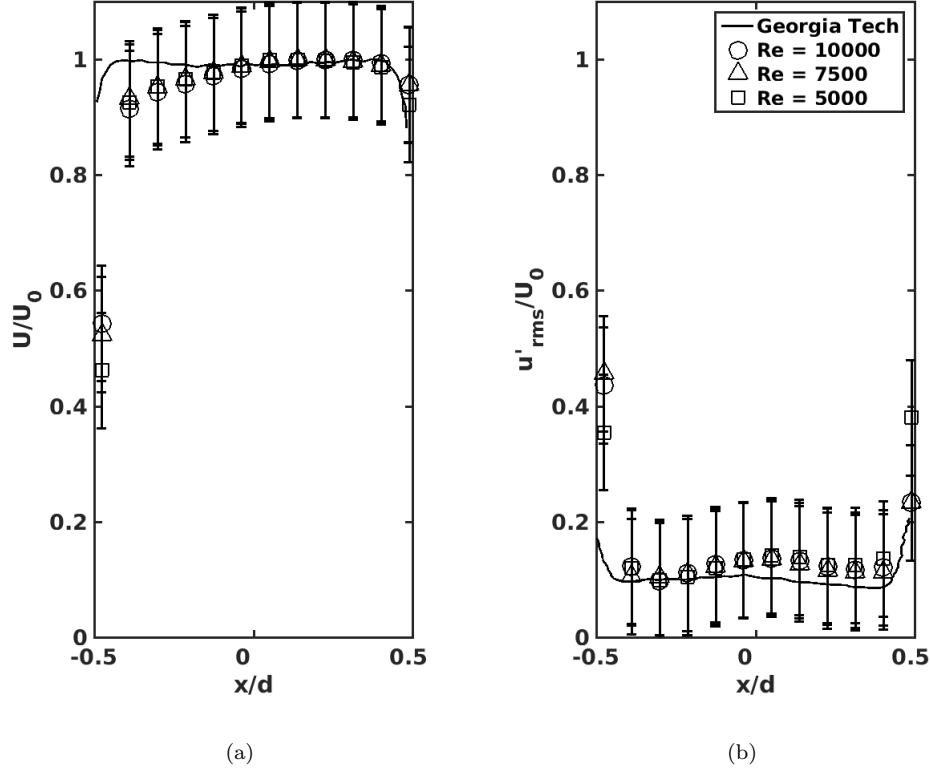
FIGURE 3.3: Normalized axial velocity profiles at 3 mm above the burner exit plane. The black line represents data reported by Venkateswaran et al. [22], and is in good agreement with the hotwire data collected in this study (circles, squares, and triangles). (a) Bulk velocity profile normalized by max axial velocity; (b) Turbulence intensity, rms of the velocity fluctuations normalized but the bulk mean velocity.

3.3 Image Processing

The average flame area $(\overline{A}_{\langle c \rangle})$ is determined though image processing of ultraviolet (UV) chemiluminescence images of the flame front. Recall, the global consumption speed $(S_{T,GC})$ is dependent on the mean flame brush area defined by contour $\langle c \rangle$, as shown in equation 2.5. The mean flame brush area is determined from chemiluminescence measurements using an Andor iStar 334-T, 16-bit, intensified charge-coupled device (ICCD) camera. The camera has a 1024×1024 pixel resolution and a 25 mm, $f/4.0$, UV camera lens. This system is sensitive in the visible and ultraviolet spectrum between 230–1.100 nm, and as such is capable of measuring OH^*, CH^*, and $CO_2{}^*$ chemilumines-cence. Line-of-sight reference images are obtained over 3 minutes at a sampling rate of

2 Hz. These reference images are used to minimize bias from the pilot flame and reduce background noise. The exposure time and gate width for these images are 0.1 s and 0.07 s, respectively.

Image processing to determine the average flame sheet from the measurements was completed using the technique developed by Venkateswaran et al. [22] and is summarized here.
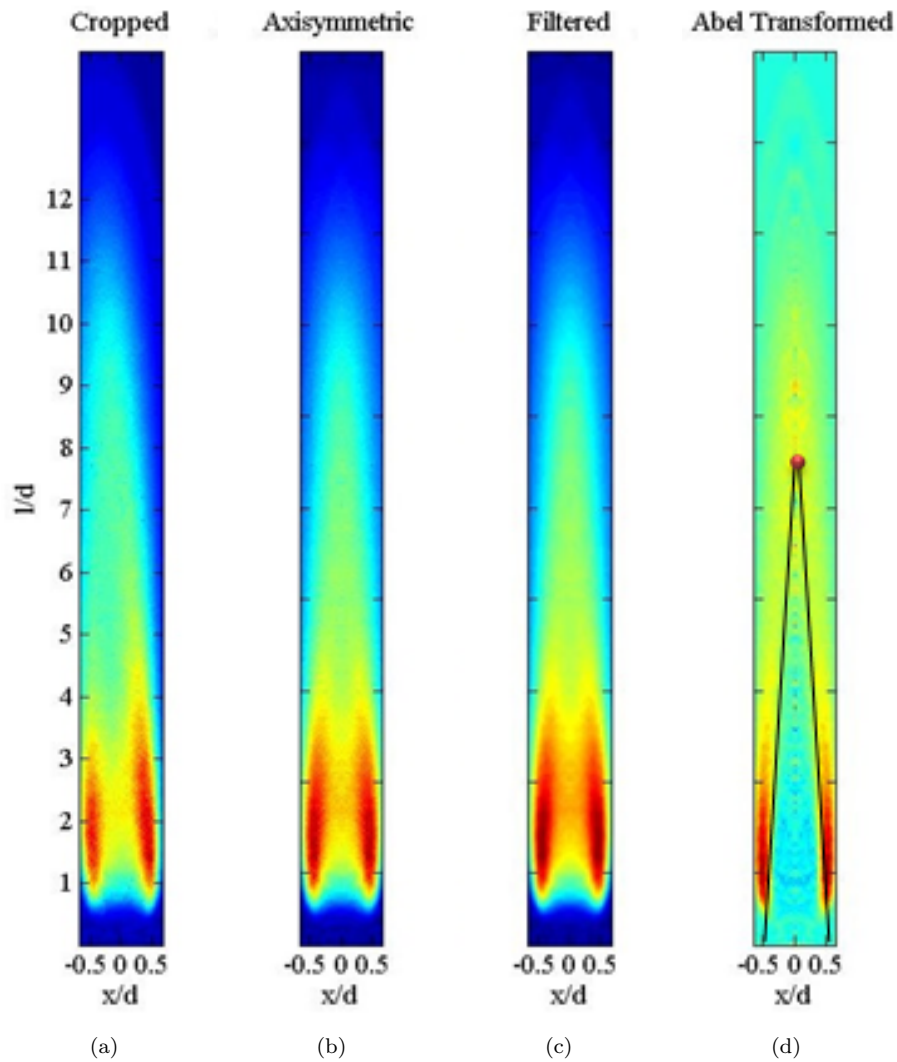
FIGURE 3.4: Step-by-step summary of image processing approach:(a) time-averaged, background subtracted and cropped image (b) Image corrected for axisymmetry (c) 2-D median filtered image (d) Abel transform result with $\langle C \rangle = 0.5$ contour drawn.

Figure 3.4 provides an illustration of the chemiluminescence image after each step in the analysis process. The line-of-sight images are time averages, the background is

subtracted, and the image is cropped (Figure 3.4(a)). The image is then corrected for axisymmetry and filtered using a 2-D median filter with a kernel less than 2% of the burner diameter (Figures 3.4(b) and 3.4(c)). A three-point Abel deconvolution is applied and the resulting axial distribution of the centerline intensity is fit to a Gaussian curve. The maximum intensity location is determined. The leading edge of the time averaged flame-brush is determined from this curve. This point is the most probable location of the flame brush, and is defined as the $\langle C \rangle = 0.5$ progress variable contour and corresponds to the location of maximum intensity [22] (Figure 3.4(d)). Once the location of mean intensity is determined, two lines are then drawn from this point to the edges of the burner, on either side of the outlet, and rotated to generate a cone. Figure 3.4(d) shows the $\langle C \rangle = 0.5$ surface drawn on the flame. The estimated uncertainty in this process is 2–3% [22]. Further discussion on the methods for uncertainty quantification can be found in section 3.6.

The outer surface area of the resulting cone is defined as the mean area of the flame brush $(\overline{A}_{\langle C \rangle})$ in the global consumption speed $(S_{T,GC})$ definition. Additional discussion on validation and development of this method can be found in [22]; the MATLAB code used in executing this method can be found in Appendix C.

3.4 Fuel Selection

Three fuels are considered in this study: a conventional Jet-A blend known as A2, and two experimental blends referred to as C1 and C5. These fuels have been selected to investigate potential sensitivities to fuel chemistry observed in the literature. A2 is the primary reference due to its common usage in commercial and military aviation. This fuel is compared to a bimodal blend of iso-dodecane and iso-hexadecane (C1), and a mix of iso-decane, n-decane, iso-undecane, and 1,2,4-trimethylbenzene (C5). These fuels have been selected to investigate sensitivities to aromatic and alkane content as well as average carbon number of the fuels. Each of the fuels have similar lower heating values and densities as indicated in Table 3.1. However, these fuels have dramatically different compositions, as indicated by the average molecular formulas and molar masses.

The differences in the chemical classes within the fuels are further highlighted in Figures 3.5. These bar graphs indicate the distribution of components within the aromatic, alkane, and cycloalkane fuel classes relative to carbon number of the fuel.

TABLE 3.1: Average fuel properties for selected fuel blends [70]

Fuel	Avg. Molecular Formula	Molar Mass [kg kmol^{-1}]	LHV MJ kg^{-1}	ρ kg m^{-3}
A2	$C_{11.4}H_{22.1}$	158.6	43.0	804
C1	$C_{12.9}H_{26.8}$	181.9	43.6	782
C5	$C_{9.7}H_{18.7}$	135.4	42.8	770

Notice that A2 has a near Gaussian distribution of aromatic, alkane, and cycloalkanes relative to carbon number. Conversely, C1 is exclusively branched alkanes, and C5 is a mix of branched/straight alkanes and aromatics. Note that these fuels isolate both species chemical class as well as species carbon number. C1 in particular is a bimodal blend of C_{12} and C_{16} iso-alkanes while C5 is comprised of species with C_{11} carbon numbers and below. As a result, these fuels highlight fuel chemistry sensitivities to alkane and aromatic content as well differences in species carbon content, while maintaining similar lower heating values. The similarity in lower heating value is important as flame speed is often sensitive to flame temperature. A similar lower heating value will provide a similar flame temperature, controlling for this sensitivity.

3.5   Laminar Scaling Parameters

Laminar flame calculations were completed in order to obtain relevant scaling parameters for analysis of the global consumption speed. These scaling parameters match those used by Venkateswaran et al. [22, 32] for zero-stretch laminar flame speed and have been demonstrated to collapse global consumption speed data for constant pressure over a wide range of conditions.

Three mechanisms, known as HyChem mechanisms, were used. These mechanisms were developed by Xu et al. [71] for the A2, C1, and C5 fuels used in this study. The mixture-averages laminar simulations were completed using PREMIX [71] includng soret and dufour effects with a domain size of ± 0.5 m and grad. and curv. settings of 0.05. It should be noted the HyChem approach is still in the validation phase and has not yet completed peer-review; however, through personal communication with Egolfopoulos et al. [72], experimental values for the zero-stretch laminar flame speed have been obtained to ensure the calculated values are accurate. The calculated values for zero-stretch laminar flame speed at the validation conditions (403 K and 1 atm) are used for this analysis. This is to ensure an accurate analysis and avoid the scaling challenges reviewed in Section
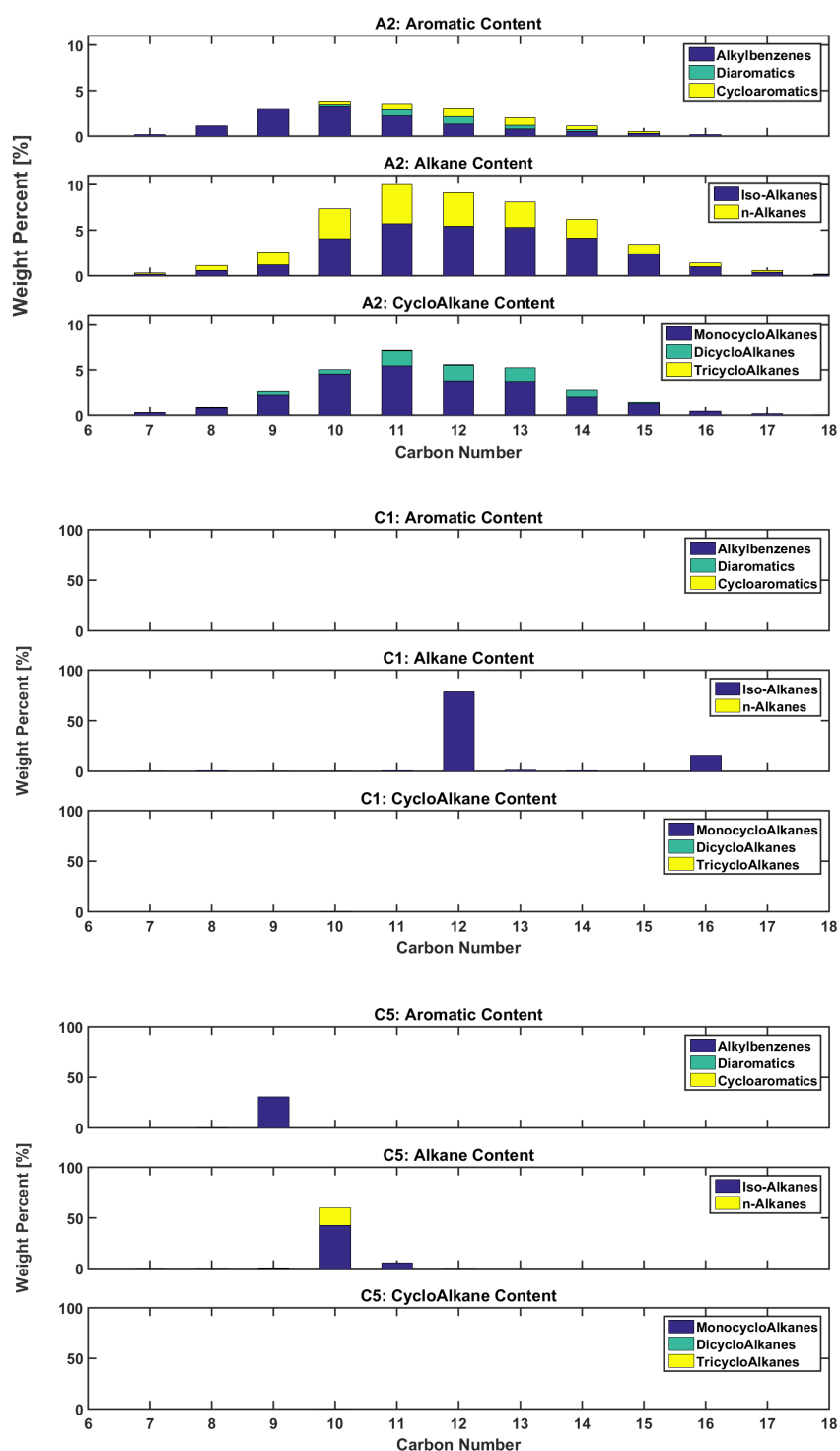
FIGURE 3.5: Fuel species composition by weight percent, presented relative to carbon number for: A2, C1, and C5. Note: The axis limits for A2 are different.

2.2.2. These calculated values are presented in Chapter 4. Note, the experimental validation values received are not presented but are within 5 % of the calculated laminar flame speeds [72].

3.6 Sensitivity and Uncertainty Analysis

Uncertainty quantification for the experimental and image processing methods was determined through a combination of Kline-McClintock, sequential perturbation, and statistical methods. First, uncertainty propagation from instrumentation bias was determined using the Kline-McClintock method. Manufacturer uncertainties were used in conjunction with the operating conditions to determine an estimate of instrumentation bias for the global consumption speed measure. Second, a sequential perturbation sensitivity analysis was used to estimate the impact and uncertainty of both the image processing method and the pilot flame. The input parameters of both the image processing method and pilot flame were systematically and sequentially perturbed with incrementally larger values until a quantifiable change in the global consumption speed was observed. The minimum possible perturbation that caused a measurable change in the global consumption speed was used in determining uncertainty. The relative magnitude of this change was used to determine an absolute value of uncertainty relative to the global consumption speed, while the maximum perturbation was used to determine an allowable operating range for each parameter. Finally, the precision error was determined by applying a student-t distribution uncertainty estimate to the collected data. Repeatability data was collected over three or more days, with three sets of three flame speed measurements collected per day. To ensure robust repeatability the burner was fully disassembled, cleaned, and reassembled regularly during data collection. The total uncertainty was determined as the root sum of the squares of the instrumentation bias, image processing bias, pilot flame bias, and precision error as shown in equation 3.2,

$$U_{S_{T,GC}} = \sqrt{U_P^2 + U_{B,Ints.}^2 + U_{B,Img}^2 + U_{B,Pilot}^2}. \tag{3.2}$$

The total uncertainty of the global consumption speed was between 4–11 % of the flame speed; bias uncertainty is on the order of 6–10 %, while precision error is 9 % on average. These values are presented as error bars on the plots in Chapter 4. A brief summary of the uncertainty and sensitivity analysis is presented herein.

3.6.1 Instrumentation Bias

The Kline-McClintock method was used to determine how instrumentation uncertainty propagated through to the global consumption speed measure from the initial temperature, pressure, and flow measurements. The primary source of uncertainty comes from measurement of the main air flow rate using rotameters. Table 3.2 provides characteristic uncertainties and an estimated range of uncertainty for the global consumption speed, mass flow rate, density, flame area, unburned temperature, and equivalence ratio.

The turbulence intensity was assumed to have an average total uncertainty of 10 % based on analysis performed by Venkateswaran et al. [22] for matching burner configuration. Additional summary of manufacturer uncertainties, test conditions, and uncertainty propagation calculations can be found in Appendices A, D, and B, respectively. Further discussion of the uncertainties associated with the turbulence intensity measure can be found in [22].

TABLE 3.2: Estimated uncertainty propagation from instrumentation for global consumption speed, equivalence ratio, and turbulence intensity.

Variable	Nominal Range	Uncertainty Source	Absolute Uncertainty	% Uncertainty
T_u	180–200 °C	Thermocouple	± 3.6–4 K	2 %
ρ_u	750–780 $\mathrm{g\,m^{-3}}$	T_u, P_{atm}	± 22–23 $\mathrm{g\,m^{-3}}$	$\sim 3\,\%$
$\dot{m}$	1.1–2.3 $\mathrm{g\,s^{-1}}$	$\rho_u, \dot{V}_{air}, \dot{m}_{fuel}$	± 0.088–0.092 $\mathrm{g\,s^{-1}}$	4–8 %
$\overline{A}_{\langle c \rangle}$	6–19 $\mathrm{cm^2}$	Img. Proc.	0.06–0.38 $\mathrm{cm^2}$	1–2 %
u'_{rms}/U_0	0.10–0.20	[22]	± 0.01–0.02	$\sim 10\,\%$
ϕ	0.70–1.00	$\dot{m}_{air}, \dot{m}_{fuel}$	± 0.05–0.03	3–5 %
$S_{T,GC}$	1.25–2.59 $\mathrm{m\,s^{-1}}$	$\rho_u, \dot{m}_{air}, \overline{A}_{\langle c \rangle}$	± 0.05–0.13 $\mathrm{m\,s^{-1}}$	4–8 %

In this uncertainty analysis, the density of the unburned gases was approximated as the density of air for all calculations. This approximation is acceptable as the vaporized fuel is at most $\sim 6\,\%$ of the mixture by mass and has a vaporized density similar to air in all

cases. An additional 1.0 % bias uncertainty was added to the relative uncertainty of the density to account for this approximation. This additional uncertainty is conservative as the total change in the density accounting for the density of the vaporized fuel will be less than 1 %

3.6.2   Image Processing Bias

As mentioned previously, the uncertainty in the image processing technique was determined through a sequential perturbation method. Each of the relevant image processing steps were systematically and sequentially perturbed to determine both the magnitude of the associated uncertainty and the minimum perturbation needed to cause a measurable change in the global consumption speed. The results of this analysis are summarized in Table 3.3. Values left blank in Table 3.3 correspond to image correction steps that do not have an operable range, i.e., they are either included or not. For example, background subtraction can either be performed or not, but there are not relative degrees of subtraction.

TABLE 3.3: Estimated uncertainty of image processing methods.

Adjustment	Allowable Range	Uncertainty	Set Point
Spacial Calibration	$\pm 5 \ Pixel$	$1 \ \% - 2 \ \%$	User Defined
Background Subtraction		$> 1 \ \%$	
Cropping	$\pm 10 \ Pixel$	$1 \ \%$	From Spacial Calibration
Antisymmetry Correction		$2 \ \%$	
2D Median Filter	$< (10x10) \ Pixel$	$1 \ \%$	$5x5 \ Pixel$
$\overline{\mathbf{A}}_{\langle \mathbf{c} \rangle}$		$\mathbf{1 \ \% - 2 \ \%}$	**Net Uncertainty**

3.6.3   Pilot Flame Sensitivity

The pilot flame sensitivity was determined with the sequential perturbation method. A methane/air pilot flame with an equivalence ratio of one was used. The heat release of the pilot flame was controlled and limited to a set percentage of the heat release from the Bunsen burner flame. Heat release values for the Bunsen burner flame were based

on lower heating values (LHV) determined using the Federal Aviation Administration NJFCP fuel report [70] for these fuels.

Uncertainties are based on the change in global consumption speed relative to a minimum pilot flame heat release of 5% for a main flame equivalence ratio of one. For lean equivalence ratios the relative effect is difficult to determine as the flame may be unstable for low pilot flame heat release rates and a reference global consumption speed at a pilot flame heat release of 5% may not exist. This minimum heat release was required to maintain a stable pilot flame due to the high velocity of the main fuel/air jet. A summary of this analysis is provided in Table 3.4.

TABLE 3.4: Sensitivity of the global consumption speed to pilot flame heat release.

Heat Release % Main Flame	Stability Range	Uncertainty
~ 5 %	$\phi = 0.85 - 1.0$	
~ 7.5 %	$\phi = 0.8 - 1.0$	~ 3 %
~ 10 %	$\phi = 0.7 - 1.0$	~ 5 %
~ 12.5 %	$\phi = 0.7 - 1.0$	~ 10 %

Based on this analysis, the pilot flame was set to ~ 10 % of the heat release of the main flame based on the LHV resulting in an approximate uncertainty of 5 % in the global consumption speed. These sensitivities were consistent over the three fuels investigated.

3.7 Governing Assumptions

There are four primary assumptions which must be considered in the discussion of this line-of-sight imaging technique:

1. The instantaneous reaction front is thin.

2. The time-averaged reaction front is axisymmetric.

3. Fuel is fully consumed through the reaction front.

4. OH^*, CH^*, and CO_2^* radicals exist only in the reaction front.

The first assumption is well accepted for closed, turbulent premixed-flames and is discussed by [2, 26]. Moreover, instantaneous focused Schlieren images by Kobayashi et al. [48, 61] validate this assumption for a similar piloted Bunsen configuration.

The second assumption stems from the first and is illustrated in Figure 3.6.

(a)   (b)
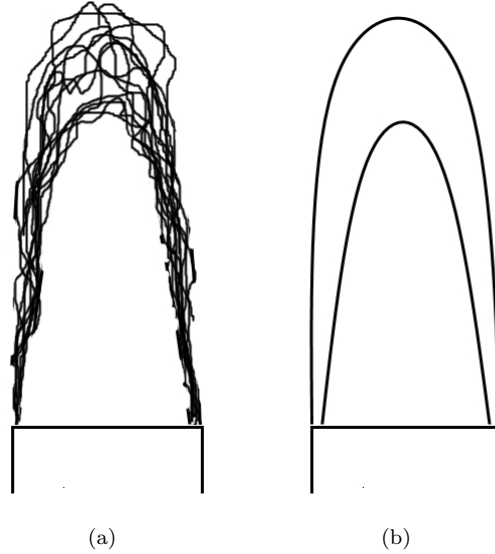
FIGURE 3.6: Cartoon representation of instantaneous and time averaged reaction front; (a) Superposition of several instantaneous reaction fronts forming flame brush, (b) Time averaged reaction front.

In Figure 3.6(a), each individual line represents the flame front at an instant in time. The time averaged flame brush is thus the aggregate of these instantaneous lines [2]. If the instantaneous reaction front is thin and wrinkled, and the fuel-air jet is axisymmetric then the time averaged flame brush can be assumed to be axisymmetric; Figure 3.6(b).

The third assumption that fuel is fully consumed through the reaction front has been thoroughly validated for similar geometries by Kobayashi et al. [29] and Venkatswaren et al. [22] and is required by the thin reaction front assumption [2]. However, to further ensure this assumption is valid, the equivalence ratio is restricted to a range of 0.7-1.0. This restriction avoids the potential for un-combusted fuel to pass through the reaction front as may occur in rich ($\phi > 1$) combustion where there is insufficient air to fully oxidize the fuel.

Finally, assumption four has been thoroughly validated by Kobayashi et al. [29, 48, 60, 61] for a similar Bunsen burner configuration using OH-PLIF . As demonstrated by

Guyot et al. [73] there are two peaks in radiation intensity at $\sim$308 nm and $\sim$431 nm emitted during hydrocarbon oxidation; these wavelengths correspond to OH^* and CH^* emissions. In addition the same study found $CO_2{}^*$ emitted over a spectrum ranging from $\sim$300 nm to $\sim$450 nm [73]. These radicals are typically short lived and the result of fast elementary reactions which occur as intermediate steps during the oxidation process [2]. Kobayashi et al. [48, 61] presented line-of-sight images validating that these emissions occur primarily in the thin reaction region using OH-PLIF, sensitive to these wavelengths, and focused Schlieren to provide a spacial reference.

Additional information on the underlying assumptions used in determining the global consumption speed is presented by Gouldin et al. [23] and Lieuwen et al. [74] and the sources cited therein.

3.8 Limitations

There are three primary limitations of this experimental approach which must be understood. First, the flame area used in the definition of the global consumption speed is not a true flame area. The average flame area is a derived quantity based on a physically relevant progress variable. The area is based on OH^*, CH^*, and $CO_2{}^*$ chemiluminescence, which does physically represent the flame front [23, 29, 60, 73]. However, as shown in Figure 3.6, the flame front is not a perfect cone and as such there is an inherent uncertainty in this approximation. Focused Schlieren performed by Kobayashi et al. does demonstrate that the conical approximation is reasonable and uncertainty is small as a result [48, 61]. Thus, although it would be experimentally prohibitive to quantify the uncertainty in this approximation, based on the results of Kobayashi et al. it is reasonable to neglect these effects [48, 61].

Second, the vaporized fuel/air mixture is assumed to have the thermochemical properties of a pure air mixture at an equivalent temperature and pressure. As stated previously, this assumption is common and valid as the fuel is at most 6 % by mass of the mixture. It must be understood that this assumption may still impact the results of this study, if only on a small scale. As a result, this study is strictly an investigation of global parameters; local phenomena will depend on transport properties specific to each fuel not represented when approximating a fuel/air mixture as pure air.

Finally, the lean stability limits are determined through visual inspection of the flame front and, as a result, may be prone to uncertainty. For Bunsen flames, when the

(a) Closed flame (b) Broken flame
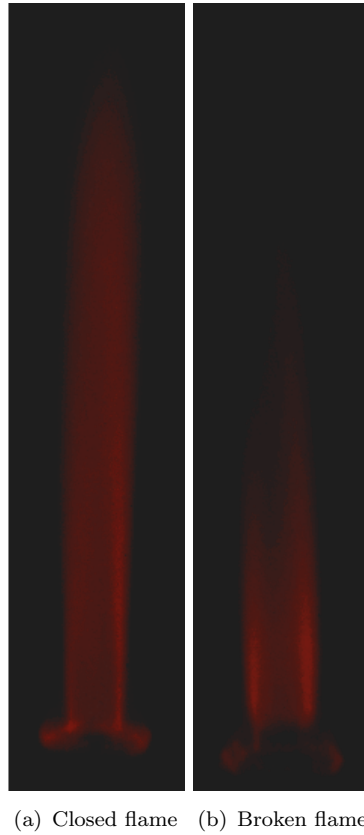
FIGURE 3.7: Raw UV-images of C1 Bunsen burner flames showing closed and broken flame regimes.

local velocity exceeds the local burning rate, the flame tip breaks open and the global consumption speed definition becomes invalid because fuel may pass through without reacting [2]. This phenomenon is well documented and can be identified with a strong understanding of the local burning parameters and activation energy of the fuel [2]. However, local measures and determinations of activation energies are outside the scope of this study and would be prohibitively expensive to determine. Practically, this effect is apparent in the data as an artificial increase in the global consumption speed. The broken flame tip skews the intensity of OH^*, CH^*, and CO_2^* chemiluminescence emission towards the burner. This results in a decreased in flame area and an increase in the global consumption speed. Figure 3.7 presents raw UV-images of the C1 Bunsen flames highlighting the closed flame and broken flame regimes. Through visual inspection of the chemiluminescence images at these conditions it is clear that in the broken flame regime, the observed increase in flame speed does not represent true physics. As a result, the lean stability limits must be determined through visual inspection of the flame front,

and are indicated by an increase in the global consumption speed at lean conditions.

These limitations are highlighted as they are difficult or impossible to quantify with the available experimental apparatus. Each of these limitations are primarily relevant in local analysis of the flame front and do not significantly impact the global consumption speed. However, these limitations must be considered when comparing the result of this study to other turbulent flame speed studies.

Chapter 4

Results and Discussion

This chapter presents the experimental results, provides discussion of the observed trends, and presents plausible explanations for governing physics. First, laminar flame speeds and adiabatic flame temperatures are presented. Next, the global consumption speeds for the three fuels at a Reynolds number (Re_D) of 5.000, 7.500, and 10.000 and estimated turbulence intensities of 10 % and 20 % will be presented for all fuels, with equivalence ratios ranging from 0.70–1.0 . Finally, dimensional analysis results examining sensitivities of the global consumption speed to bulk and fluctuating velocities, flame height, and stretch rate will be presented and discussed.

4.1   Laminar Burning Parameters

The zero-stretched laminar flame speeds calculated with the HyChem mechanisms [71] are presented in Figure 4.1. Laminar flame parameters are calculated at $403\,\mathrm{K}$ and $1\,\mathrm{atm}$. These laminar conditions are different then the turbulent operating conditions used in this study but match experimental validation data received through personal communication with Egolfopoulos [72]. Although the zero-stretch laminar flame speed is likely to increase between $403\,\mathrm{K}$ and $450\,\mathrm{K}$, the trends of the laminar flame speed relative to fuel type and equivalence ratio will not. These values provide a valid reference for dimensional scaling analysis. A2, C1, and C5 are circles, triangles, and squares respectively. This convention will be maintained throughout this chapter. Experimental validation data is not presented by request of Egolfopoulos.

Note that the laminar flame speeds of these fuels are similar. The laminar flame speed of A2 is 5 % or less slower than C5 at all equivalence ratios. Similarly, C1 is 10 % or less slower than A2 and 14 % or less slower than C5.
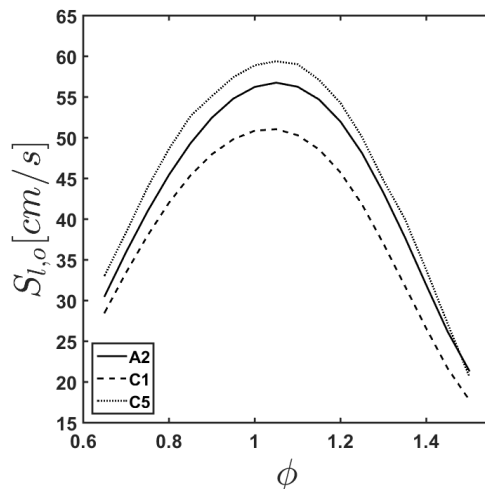
FIGURE 4.1: Zero-stretch laminar flame speeds of selected fuels at 403 K and 1 atm.

The observed similarities in laminar flame speeds are expected. A2, C1, and C5 have similar average molecular structures and lower heating values are within 2 %, as shown in Table 3.1. These calculated values provide a foundation for comparison of the global consumption speed data.

4.2 Turbulent Flame Speeds

The global consumption speeds of A2, C1, and C5 at all operating conditions are presented in this section. Table 4.1 provides a summary of the marker convention used in presenting the different flame conditions. All tests were conducted at atmospheric pressure with the vaporizer temperature at 470 K and the outlet temperature of the burner at 450 K.

4.2.1 Global Consumption Speeds

The global consumption speeds for the three fuels at Re_D of 5,000, 7,500, and 10,000 and estimated turbulence intensity of 10 % are presented relative to adiabatic flame temperature in Figure 4.2; the laminar flame trends are presented for ease of comparison and are calculated with the NJFCP thermophysical property tables [70]. Error bars

TABLE 4.1: Legend

Re_D	A2		C1		C5	
	$I = 10\ \%$	$I = 20\ \%$	$I = 10\ \%$	$I = 20\ \%$	$I = 10\ \%$	$I = 20\ \%$
$5{,}000$	●	○	▲	△	■	□
$7{,}500$	●	○	▲	△	■	□
$10{,}000$	●	○	▲	△	■	□

represent the total bias and precision uncertainty within 95 % confidence and are on the order of 10 % or less for both axes; horizontal uncertainty bars are constant (10 %) and left off for clarity.

(a) Laminar Flame

(b) Low Intensity Turbulent Flame
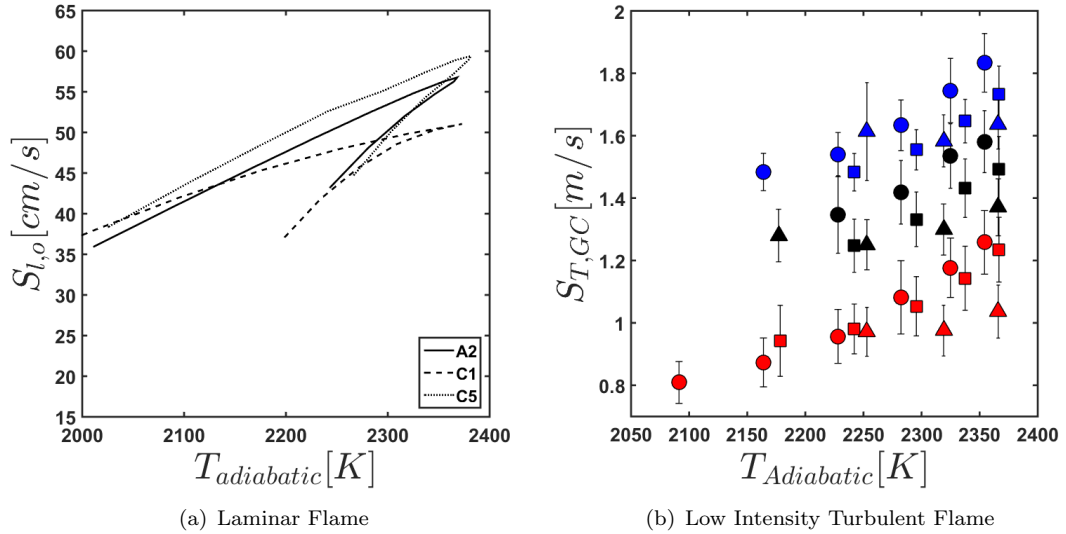
FIGURE 4.2: Global consumption speed vs adiabatic flame temperature for all fuels at low turbulence intensity of $I = 10\ \%$; laminar flame results provided for ease of reference.

Both the laminar and turbulent flame speeds increase with increasing adiabatic flame temperature up to an equivalence ratio of unity. The adiabatic flame temperatures of all three fuels are within 5 % for all equivalence ratios. No difference in trends is readily discernible. This suggests there is no difference in the sensitivity of the global

consumption speed to adiabatic flame temperature relative to the laminar flame speed. Similar results are observed for high turbulence intensity conditions.

The global consumption speeds for the three fuels at Re_D of $5,000$, $7,500$, and $10,000$ and estimated turbulence intensities near $10\ \%$ and $20\ \%$ are presented relative to equivalence ratio in Figure 4.3. The equivalence ratio is based on stoichiometry found using the average molecular formula presented in the NJFCP thermophysical properties tables [70]. Error bars represent the total bias and precision uncertainty within $95\ \%$ confidence and are on the order of $10\ \%$ or less of the value. The uncertainty in the equivalence ratio is between $3\ \%$ and $5\ \%$ with higher uncertainties noted for lower equivalence ratios; horizontal error bars have been left off for clarity.

(a) Low Turbulence Intensity (b) High Turbulence Intensity
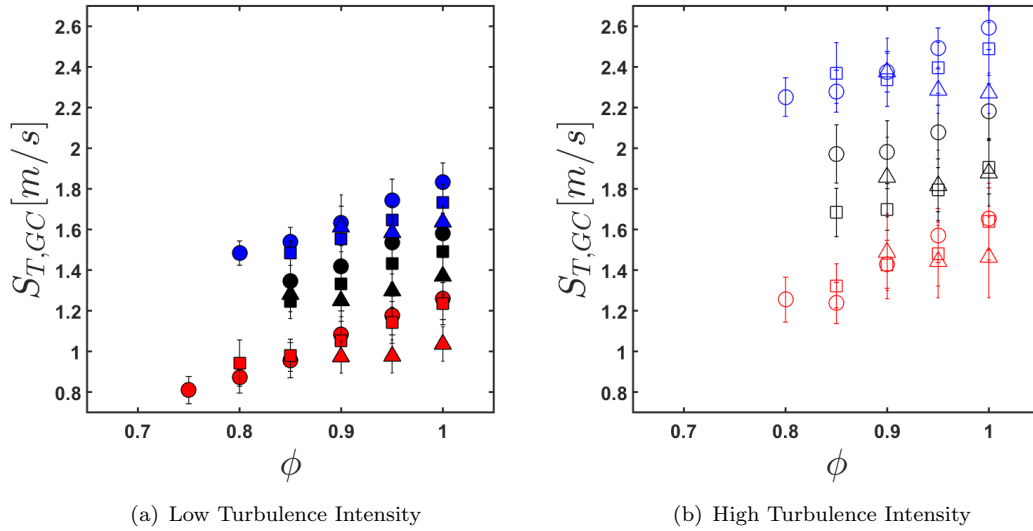
FIGURE 4.3: Global consumption speed for all fuels and flow conditions presented relative to equivalence ratio; (a) Low turbulence intensity $I = 10\ \%$ (b) High turbulence intensity $I = 20\ \%$

The global consumption speed for all three fuels increases with both bulk Reynolds number and turbulence intensity. The global consumption speed of A2 and C5 are observed to increase with equivalence ratio up to $\phi = 1$. This is expected because of the sensitivity of the flame speed to the flame temperature, which increases as the equivalence ratio is increased. A similar sensitivity to equivalence ratio is observed for C1 at low turbulence conditions cases but is not observed for C1 at high turbulence intensity conditions.

The global consumption speed of A2 is within 5 % of C5 for all flow conditions, which is similar to observed laminar flame speed trends. Both the A2 and C5 fuels demonstrate an increased sensitivity of the global consumption speed to turbulence intensity with increasing bulk Reynolds number and decreasing equivalence ratio. To illustrate this trend, Table 4.2 presents global consumption speed values for A2, C1, and C5 at an equivalence ratio of one and the lean stability limits of each fuel. The global consumption speeds of A2 and C5 both increase by 24 % and 30 % from low to high turbulence intensity at $\phi = 1.0$ for $Re_D = 5,000$ and $Re_D = 10,000$, respectively. However, at the lower stability limit of $\phi = 0.85$, A2 increases by 22 % and 3 % while C5 increases by 26 % and 37 % for $Re_D = 5,000$ and $Re_D = 10,000$, respectively, between the low and high turbulence intensity cases. This observation indicates a higher sensitivity of C5 to the turbulence intensity than A2 for lean flames. Moreover, the global consumption speed of A2 is higher than C5 for all flow conditions. This trend is different than the laminar flame speed results where C5 was higher than A2 at all equivalence ratios. This shift between which fuel has a high flame speed reinforces the observed difference in sensitivity of the turbulent flame speed to fuel chemistry.

TABLE 4.2: Representative global consumption speeds at an equivalence ratio of one and the lean stability limits for A2, C1, and C5.

		A2				
		$\phi = 1.00$			$\phi = 0.85$	
	$S_{T,GC}$ [m/s]			$S_{T,GC}$ [m/s]		
Re_D	$I = 10$ %	$I = 20$ %	**Increase**	$I = 10$ %	$I = 20$ %	**Increase**
$5,000$	1.26	1.65	**24** %	0.96	1.24	**22** %
$7,500$	1.58	2.18	**28** %	1.35	1.97	**31** %
$10,000$	1.83	2.59	**30** %	1.54	2.28	**32** %
		C1				
		$\phi = 1.00$			$\phi = 0.90$	
$5,000$	1.04	1.46	**29** %	0.97	1.49	**34** %
$7,500$	1.37	1.88	**27** %	1.25	1.86	**33** %
$10,000$	1.64	2.27	**27** %	1.61	2.37	**32** %
		C5				
		$\phi = 1.00$			$\phi = 0.85$	
$5,000$	1.23	1.64	**24** %	0.98	1.32	**26** %
$7,500$	1.49	1.91	**22** %	1.25	1.68	**26** %
$10,000$	1.73	2.49	**30** %	1.48	2.37	**37** %

C1 demonstrates a little to no sensitivity of the global consumption speed to turbulence intensity with increasing bulk Reynolds number, but an increased sensitivity with decreasing equivalence ratio. For example, C1 increases by 29 % and 27 % from low to high turbulence intensity at $\phi = 1.0$ for $Re_D = 5,000$ and $Re_D = 10,000$. Similarly, at

the lower stability limit of $\phi = 0.90$, the global consumption speed of C1 increases by 34 % and 32 % for $Re_D = 5,000$ and $Re_D = 10,000$, respectively. The percent increase in the global consumption speed between the low and high turbulence intensity cases is approximately the same for all Reynolds numbers at a given equivalence ratio. This is different than A2 and C5, where the global consumption speed was found to be more sensitive to turbulence intensity with increased bulk Reynolds number. Moreover, these observations hold when uncertainty is considered.

Finally, a sensitivity of the lean stability limits to fuel chemistry, turbulence intensity, and bulk Reynolds number is observed. This is evident by the lowest equivalence ratio at which data is reported; these limits are presented in Table 4.3. A2 has the lowest lean stability limit of $\phi = 0.80$ for most flow conditions; alternatively, C5 is stable to $\phi = 0.85$ and C1 is stable to $\phi = 0.90$. The lean stability limit of A2 and C5 extends to $\phi = 0.75$ and $\phi = 0.8$, respectively, for $Re_D = 5,000$ and low turbulence intensity. These results indicate an increased stability for lower Reynolds numbers and turbulence intensities for all three fuels. Moreover, the observed difference in the sensitivity of the stability limits for A2, C1, and C5 to these flow conditions suggests a sensitivity to fuel chemistry.

TABLE 4.3: Lean stability limit equivalence ratios for A2, C1, and C5 presented relative to Reynolds number and turbulence intensity.

Re_D	**A2**		**C1**		**C5**	
	$I = 10$ %	$I = 20$ %	$I = 10$ %	$I = 20$ %	$I = 10$ %	$I = 20$ %
$5,000$	0.75	0.80	0.90	0.90	0.80	0.85
$7,500$	0.85	0.85	0.85	0.90	0.85	0.85
$10,000$	0.80	0.80	0.90	0.90	0.85	0.85

Comparing the global consumption speeds to results from the reviewed literature, these trends are counter to those observed by Hui et al. [4, 20] and Kumar et al. [11, 19] for the stretched laminar flame speeds of large-hydrocarbon fuels. These studies indicated that laminar flame speed and flame stability both increase with decreasing aromatic content [4, 11, 19, 20]. This trend is reversed in the measured global consumption speeds for A2, C1, and C5. However, Hui et al. [4, 20] and Kumar et al. [11, 19] also reported that the increase in laminar flame speed results in an increased sensitivity of alkane fuels to flame stretch. C1 is 100% iso-alkanes and has no aromatic content but is the least stable of the three fuels; conversely, A2 and C5 are 18% and 30% aromatic content by mass, respectively. Furthermore, a decrease in lean stability limits with increased flame stretch is observed in these studies for a wide range of fuels. It is plausible that the high alkane content of C1 makes it more sensitive to turbulence induced stretch effects

decreasing its stability range. Thus, although the flame speed trends are reversed the stretch sensitivities trends seem to be the same.

4.2.2 Flame Stretch Sensitivities

Flame stretch is a measure of the time-varying fluctuations in the flame front. It is defined as the rate of change of area normalized by the total flame area,

$$\kappa = \frac{1}{A}\frac{dA}{dt}, \tag{4.1}$$

and has units of inverse time (s^{-1}) [2]. Expanding this relationship, the flame stretch rate can be defined as,

$$\kappa = \nabla_{tangential} \cdot v_{s,tangential} + \left(V_f \cdot n\right)\left(\nabla \cdot n\right), \tag{4.2}$$

where $v_{s,tangential}$ is the local fluid velocity tangential to the flame front, V_f is the local displacement speed, and n is the unit normal vector of the flame front [2]. In equation 4.2, the first term is the result of non-uniformity in the flow field and can be related to local velocity fluctuations in the flow; this is typically referred to as hydrodynamic stretch and is dominated by local momentum transfer. Darrieus–Landau instabilities, such as those observed by Kobayashi et al. [29] in turbulent Bunsen flames, are an example of these effects. Alternatively, the second term is the result of unsteadiness in the flame front and caused by local and global curvature effects typically associated with thermal and mass diffusion. The global stretch rate is a measure of the average stretch rate relative to the average flame area and is an example of this type of stretch effects. Global stretch rates have been reported by Hui et al. [4, 20] and Kumar et al. [11, 19] for large-hydrocarbon fuels using counter-flow stagnation flames.

Applying Equation 4.1 to laminar Bunsen flames, it can be seen that these flames are negatively stretched and the stretch rate can be simplified to the form,

$$\kappa = \frac{w\sin\left(2\alpha\right)}{2R_f}, \tag{4.3}$$

where w is the unburned velocity, α is one-half of the angle of the flame sheet at the flame tip, and R_f is the radius of the flame at the base [2]. From this equation, it can be see that the stretch rate for laminar Bunsen flames is primarily the result of changes in

the global flame curvature. The relative structure of the flame remains constant, while the global half angle at the flame tip, α, changes with changes in unburned velocity.

Turbulent Bunsen flames exhibit both hydrodynamic and curvature based stretch effects. These effects are heavily coupled and do not lend themselves well to analytical solutions as is possible with laminar Bunsen flames. However, these principles of hydrodynamic and curvature effects can be applied to the turbulent Bunsen flames in this study through careful implementation of dimensional scaling parameters.

4.2.2.1 Normalized Velocity Scaling

To better understand the impact of flame stretch on the global consumption speed, the flame speed is presented against both the estimated root mean square (rms) of the velocity fluctuations and the bulk fluid velocity. These values are all normalized by the zero-stretch laminar flame speed in Figure 4.4. This normalization is performed to isolate the effects of local and bulk flow velocities on the global consumption speed. Similar analyses have been performed previously [22, 32, 48, 51, 52, 61]. Note that equivalence ratio increases from left to right for each data set in Figure 4.4. In addition, uncertainty bars have been omitted for clarity; typical uncertainty is on the order of 10% or less of the plotted value on both axes.

(a) Sensitivity to u'_{rms}

(b) Sensitivity to U_0
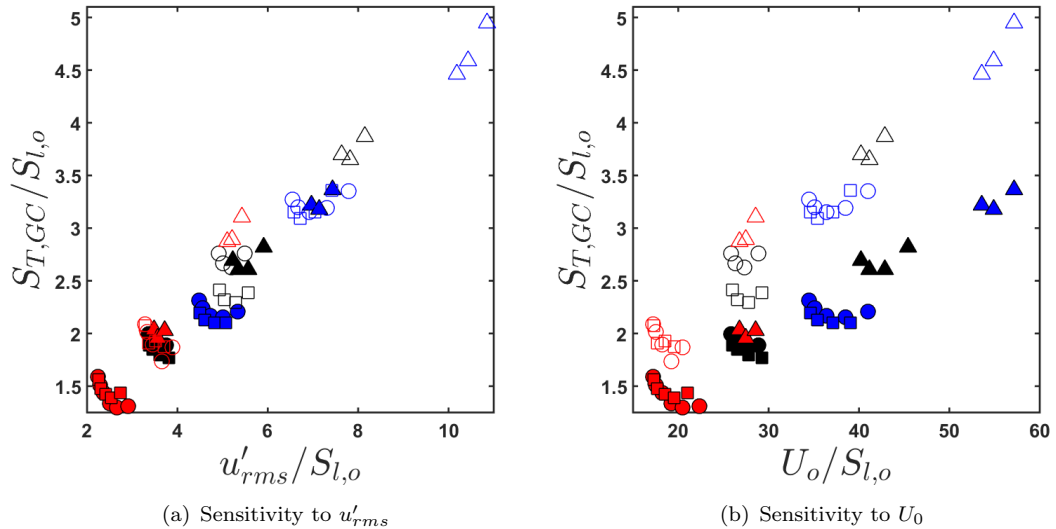
FIGURE 4.4: Global consumption speed relative to the rms of the velocity fluctuations and the bulk flow velocity normalized by zero-stretch laminar flame speed. The equivalence ratio increases from left to right for each data set.

Two key trends are observed in Figure 4.4. First, the global consumption speed increases proportionally for increasing normalized u'_{rms}. This suggests the global consumption speed is sensitive to hydrodynamic stretch; the normalized global consumption speed increases with increases in the relative magnitude of turbulent velocity fluctuations. Second, a similar proportional relationship is observed between the global consumption speed and U_0. In contrast to u'_{rms}, high (open-face markers) and low (closed-face markers) turbulence intensities demonstrate different proportional relationships to the global consumption speed, with high turbulence intensity conditions demonstrating a steeper (more sensitive) relationship. This suggests both a sensitivity of the global consumption speed to global flame curvature, and a strong coupling of hydrodynamic and curvature based stretch effects.

Examining fuel sensitivities for both the u'_{rms} and U_0 plots, A2 and C5 demonstrate similar trends. The normalized global consumption speeds of A2 and C5 are within 5% or less for most flow conditions. An ~ 12 % difference in the normalized global consumption speed is observed between A2 and C5 for a bulk Reynolds number of $7,500$ and high turbulence intensity. However, referring to Figure 4.3, these points are within the reported uncertainty for these conditions. Conversely, C1 consistently demonstrated a higher normalized global consumption speed than A2 and C5 at all conditions. Specifically, the normalized global consumption speed of C1 is between 20% and 40% higher than that of A2 and C5. Similarly, the normalised rms velocity (u'_{rms}) is on average 55% higher compared to A2 and C5 for all flow conditions. This difference is such that the normalized global consumption speed of C1 at $Re_D = 5,000$ is similar to that of A2 and C5 at $Re_D = 7,500$; moreover, the normalized global consumption speed of C1 at $Re_D = 7,500$ is higher than that of A2 and C5 at $Re_D = 10,000$. This observed difference in normalized global consumption speed between fuel blends reinforces that a strong sensitivity exists for the global consumption to fuel chemistry.

Examining the fuel composition information presented in Figure 3.5, it is plausible that the observed sensitivity of the global consumption speed to fuel chemistry is the result of aromatic content. A2 and C5 are approximately 18% and 30% by mass aromatics, respectively, while C1 is strictly a bi-modal blend of iso-alkanes. Similar results by Venkateswaran et al. [32] indicate that flames where $S_{L,max}/S_{L,0} \gg 1$ are highly sensitive to stretch effects while $S_{L,max}/S_{L,0} \sim 1$ are not. Furthermore, Hui et al. [4, 20] and Kumar et al. [11, 19] reached similar conclusions and demonstrated that $S_{L,max}/S_{L,0} \sim 1$ for aromatic fuels but $\gg 1$ for alkane fuels. Comparing these conclusions with the results of this study, it is plausible that the global consumption speeds of A2 and C5 are less

sensitive to flame stretch than C1 because of this increased aromatic content. This result is important as it indicates that the combustion characteristics of multi-component fuels are more complex than previously thought. This suggests that single component fuels are insufficient substitutes for real transportation fuels in combustion studies.

It is important to note that Hui et al. [4, 20] and Kumar et al. [11, 19] report trends counter to those observed herein. In their studies, the laminar flame speed and flame stability ranges decrease with increased aromatic content. In this study, the turbulent global consumption speed and stability ranges increase with increased aromatic content. However, both these results and those reported by Hui et al. [4, 20] and Kumar et al. [11, 19] are attributed to increased flame stretch. This suggests a potential coupling of hydrodynamic and curvature based stretch effects in turbulent Bunsen flames. From an energy perspective, stretch constitutes a loss and serves to lower the overall flame temperature, weakening the reaction front. Thus, it is plausible that low aromatic content fuels that are highly sensitive to stretch, such as C1, stretch more readily under turbulent flow conditions, and as a result become unstable at higher equivalence ratios. This theory is supported by the high sensitivity of the global consumption speed of C1 to both u'_{rms} and U_0 in Figure 4.4; recall u'_{rms} and U_0 affect hydrodynamic and curvature based stretch effects, respectively.

To further investigate the potential sensitivity of the global consumption speed to fuel chemistry, Figure 4.5 plots the normalized global consumption speed relative to equivalence ratio for all fuels and conditions. Typical uncertainties are on the order of 10% or less for the normalized global consumption speed and 5% or less for the equivalence ratio; uncertainty bars have been omitted for clarity.

The normalized global consumption speeds of A2 and C5 are observed to have little or no sensitivity to equivalence ratio. Conversely, an inverse sensitivity of the normalized global consumption speed to equivalence ratio is observed for C1. This observation agrees with the data presented in Figure 4.4, where the sensitivity of the global consumption speed to both the normalized rms and bulk velocities increases with decreasing equivalence ratio. This suggests that C1 is more sensitive to flame stretch at low equivalence ratios. As mentioned in Section 3.8, when Bunsen flames are stretched, they can break open at the tip [2]; this phenomena is observed in unprocessed UV images of the flame at the lean stability limits as shown in Figure 3.7. This opening of the tips results in an artificial increase to the global consumption speed due to limitations in the image processing technique. It is plausible that C1 becomes unstable at higher equivalence ratios than A2 and C5 under high stretch conditions; this result supports
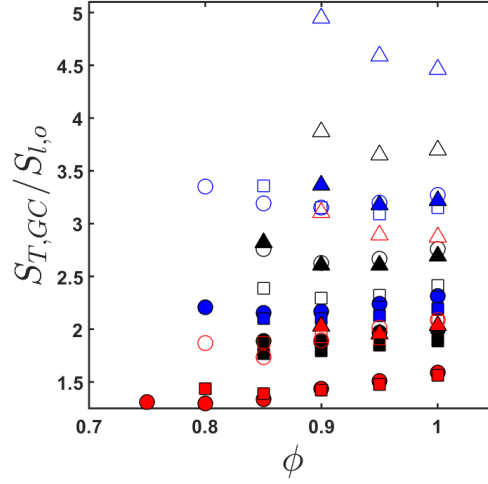
FIGURE 4.5: Normalized global consumption speed vs equivalence ratio for all fuels and conditions.

existing theories on flame stretch as an energy loss. As the equivalence ratio of C1 flame decreases, the flame temperature is reduced. This reduced temperature couples with the increased stretch effects further lowering the flame temperature and destabilizing the flame. Thus, the decreased stability range and increased global consumption speeds of C1 at low equivalence ratios observed in Figures 4.3 and 4.4 are attributed to flame stretch effects causing the flame front to break open.

4.2.2.2   Flame Structure Scaling

To further understand the sensitivities of the global consumption speed to hydrodynamic and curvature induced stretch effects, the global structure of the time-average flame front is investigated. A non-dimensional leading point location and global stretch rate are defined to aid in the analysis. The non-dimensional leading point is a measure of the average flame height and is defined as h/D, where h is the location of mean intensity of chemiluminescence emissions and D is the nominal burner diameter. The global stretch rate is adapted from Equation 4.3 and is defined as,

$$\overline{\kappa}_{\langle c \rangle} = \frac{U_0 \sin\left(2\alpha_{\langle c \rangle}\right)}{2R_f}.$$ (4.4)

Equations 4.3 and 4.4 are the same except for the definition of the flame angle and the use of the bulk fluid velocity. In Equation 4.4 $\alpha_{\langle c \rangle}$ is the time-averaged half flame

angle of the mean flame area determined from the $\langle c \rangle = 0.5$ progress variable contour; Equation 4.3 uses the instantaneous flame angle. Figure 4.6 presents the normalized global consumption speed plotted relative to the non-dimensional leading point location and global stretch rate. When compared to the normalized data in Figure 4.4, these parameters are intended to provide insight on how global flame curvature and local hydrodynamic instabilities affect the average flame area. Uncertainties for h/D and $\overline{\kappa}_{\langle c \rangle}$ are on the order of 2% and 8%, respectively. Uncertainty in the normalized global consumption speed is 10% or less; uncertainty bars are omitted for clarity.

(a) Sensitivity to flame height

(b) Sensitivity global flame stretch
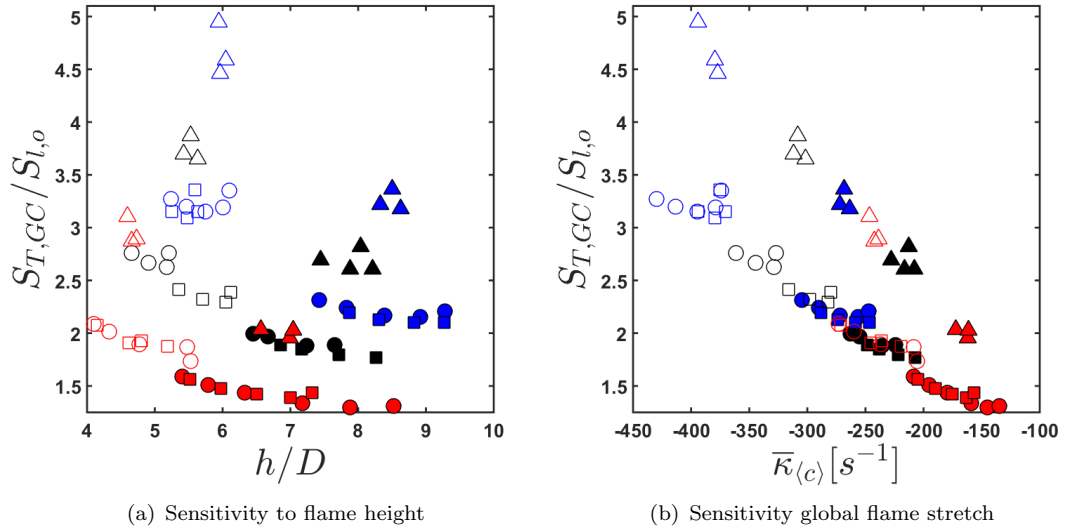
FIGURE 4.6: Global consumption speed against the non-dimensional leading point location and global stretch rate.

Four trends are observed. First, the non-dimensional leading point location increases with Reynolds number but decrease with turbulence intensity. Second, the global stretch rate is inversely proportional to the normalized global consumption speed and decreases (becomes more negative) with both Reynolds number and turbulence intensity. Third, A2 and C5 demonstrate a similar proportional relationship of the global consumption speed to h/D and $\overline{\kappa}_{\langle c \rangle}$, while C1 exhibits a greater sensitivity and steeper proportional relationship to both h/D and $\overline{\kappa}_{\langle c \rangle}$. Fourth, the non-dimensional leading point location of C1 becomes insensitive to equivalence ratio for high turbulence intensity flames. This trend for C1 flames is reversed from what is expected for other fuels and conditions, where, the non-dimensional leading point location is inversely proportional to global consumption speed. Moreover, the global consumption speed decreases with decreasing equivalence ratio for A2 and C5, as well as C1 at low turbulence intensities. In these

trends the equivalence ratio decreases from left to right for most fuels and conditions; however, for high turbulence intensity C1 flames equivalence ratio increases from bottom to top and right to left.

The reduction in non-dimensional leading point location with increased turbulence intensity is attributed to an increase in hydrodynamic stretch effects. This trend agrees with similar sensitivities to u'_{rms} observed in Figure 4.4. As the turbulence intensity is increased, the absolute magnitude of turbulent fluctuations increases. This increase results in increased wrinkling of the flame front, which subsequently increases the total flame area. As a result the flame becomes more compact, i.e., the wrinkling allows for a greater total flame area to fit within a shorter flame height. Alternatively, the increase in non-dimensional leading point location with increased Reynolds number is attributed to an increase in global flame curvature. This is analogous to inflating a balloon, as the mass flux into the flame front increases, the mean flame area and curvature must increase to compensate for the increased mass flow.

Both increased flame wrinkling and curvature increase the global consumption speed and absolute magnitude of the global stretch rate ($\overline{\kappa}_{\langle c \rangle}$) of the flame. This explains why the global consumption speed is inversely proportional to global flame stretch. As flame wrinkling increases with turbulence intensity, the mean flame area decreases, which increases the global consumption speed. Similarly, as the global curvature increases with increased bulk flow velocity and Reynolds number, molecular diffusion through the flame also increases. This increased diffusion is the result of flame thinning from high (more negative) stretch. This thinning increases the spatial gradients driving species diffusion, thus increasing mass flux through the flame [2]. This increased diffusion results in a decrease of the global consumption speed. These effects are similar to those observed by Kobayashi et al. [29] for small hydrocarbon turbulent premixed Bunsen flames, and by Hui et al. [4, 20] and Kumar et al. [11, 19] for large-hydrocarbon laminar flames. Both groups measured an increased mass diffusion and burning flux with increased flame curvature and stretch rate.

The third trend of Figure 4.6 highlights dramatic differences in the sensitivity of the global consumption speed of C1 relative to A2 and C5 and is attributed to aromatic content of the fuels. This result suggests a strong sensitivity of the global consumption speed and global stretch rate to aromatic content and reinforces observed trends in Figures 4.3, 4.4, and 4.5.

For the fourth trend, the insensitivity of high turbulence intensity C1 flames to non-dimensional leading point location in Figure 4.6 is attributed to a strong coupling of the fuel chemistry and stretch effects near the lean extinction limits. As the C1 flames became highly stretched the hydrodynamic instabilities appear to reach a maximum and the mean flame area becomes constant across a range of equivalence ratio. It is plausible that when this happens global curvature effects dominate thinning of the reaction front. This thinned reaction front results in higher species gradients, which increase diffusive transport through the flame. This theory is supported by the more negative stretch rates and constant non-dimensional leading point location of C1 at high turbulence intensity conditions. Similar effects of flame curvature increasing species diffusion are observed for a range for fuels and burner configurations [2, 4, 11, 19, 20, 29, 32]. It is plausible that the aromatic content of A2 and C5 reduces these stretch sensitivities; as a result aromatic content appears to increase flame stability for highly turbulent flames. If correct, this theory explains the trends observed in Figure 4.4.

The theories explaining the flame stretch trends observed in Figure 4.6 are strengthened by the increase in the global consumption speed of C1 near the lean stability limits. Bunsen flames break open at the tip as a result of high stretch [2]; this phenomenon can be identified through visual inspection of the flame front as shown in Figure 3.7. C1 flames should break open at higher equivalence ratios than A2 or C5, as a result of their high stretch sensitivity. Due to the limitations of this technique, this broken flame front presents as an artificially high global consumption speed. Thus, the reduced stability range and increased global consumption speeds of C1 at lean equivalence ratios are expected, and support the theory that C1 is more sensitive to flame stretch than A2 or C5. Moreover, these trends support the notion that flame stretch alters the flames area and structure changing the global consumption speed. An improved measure of the flame breaking open at the stability limits would validate these theories.

4.2.2.3   Average Karlovitz Number Scaling

To further investigate the observed stretch sensitivity, a globally averaged Karlovitz number is defined based on laminar flame theory in [2]:

$$\overline{Ka}_{\langle c \rangle} = \frac{l_T}{S_{l,0}} \overline{\kappa}_{\langle c \rangle}, \tag{4.5}$$

where l_T is the characteristic length scale of the turbulent velocity fluctuations obtained from the turbulent analysis in [22]. The Karlovitz number represents a non-dimensional

stretch rate and is a measure of how quickly the flame curvature changes relative to how quickly the flame wrinkles. Figure 4.7 presents the normalized global consumption speed relative to the average Karlovitz number ($\overline{Ka}_{\langle c \rangle}$). The relative uncertainty of the globally averaged Karlovitznumber is on the order of 12 % or less; uncertainty bars are omitted for clarity. Equivalence ratio decreases from left to right for for all fuels and conditions except C1 at high turbulence intensity which increases from right to left. These trends are similar to those discussed in Figure 4.6(b).
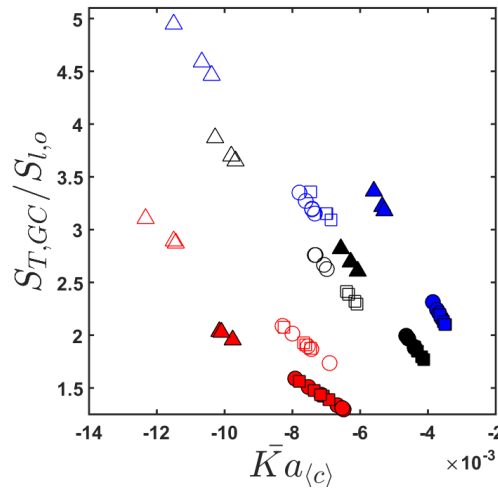
FIGURE 4.7: Normalized global consumption speed relative to globally averaged Karlovitz number for all fuels and conditions.

The average Karlovitz number is found to have an inverse linear relation to the normalized flame speed. Lines of constant Reynolds number and turbulence intensity are observed, and are consistent across all three fuels. This linear trend is expected. The Karlovitz number is a ratio of the characteristic flame and aerodynamic flow time scales (i.e., $\overline{Ka}_{\langle c \rangle} \sim \tau_{flame}/\tau_{flow}$). For a constant Reynolds number and turbulence intensity, the characteristic aerodynamic flow time scale is constant as well. If the aerodynamic flow time scale is constant, then the functional relation between the Karlovitz number and the non-dimensional global consumption speed becomes a simple linear relation of the form

$$\frac{S_{T,GC}}{S_{L,0}} = f\left(\overline{Ka}_{\langle c \rangle}\right) \sim f\left(\frac{\tau_{flame}}{\tau_{flow}}\right) = \frac{1}{\tau_{flow}} f\left(\tau_{flame}\right), \tag{4.6}$$

where the slope corresponds to the inverse of characteristic aerodynamic time scale. As a result, $\overline{Ka}_{\langle c \rangle}$ should demonstrate a linear relationship to normalized flame speed for constant flow conditions.

The average Karlovitz number is observed to increase (become less negative) with increased Reynolds number. This indicates an increase of the aerodynamic time-scale for high Reynolds number and low $\overline{Ka}_{\langle c \rangle}$ number flames. This is attributed to an increase in the absolute magnitude of the velocity fluctuations consistent with high Reynolds number flows. As the Reynolds number increases the magnitude and frequency of the velocity fluctuations increases as well, this results in greater flame wrinkling, increasing the characteristic aerodynamic time scale, and shifts $\overline{Ka}_{\langle c \rangle}$ closer to unity.

The slope of the lines for constant flow conditions becomes more similar as turbulence intensity and Reynolds number are increased. Specifically, the high turbulence intensity $Re_D = 10,000$ line is in the middle of the trends — not at an extreme — and has a similar slope to the high turbulence intensity $Re_D = 7,500$ line. The slopes of these lines becoming more similar suggests a limit to the effects of hydrodynamic and curvature base stretch. It is plausible that as stretch rate increases the slope of the line relating $\overline{Ka}_{\langle c \rangle}$ and $S_{T,GC}/S_{L,o}$ tends towards a constant. If true, this implies a limit to the effects of turbulence intensity and Reynolds number on the global consumption speed.

It is plausible that this limit of $\overline{Ka}_{\langle c \rangle}$ to Reynolds number and turbulence intensity at high stretch conditions is the mechanism responsible decreased flame stability at these conditions. This supports previous results from Kobayashi et al. [29, 48, 60, 61], which showed flame stability decreased with increased flame curvature for highly stretch-sensitive flames. Moreover, the increased sensitivity of C1 to $\overline{Ka}_{\langle c \rangle}$ fits well with the trends observed in Figures 4.6 and 4.3. If a limit is reached for stretch effects, it is expected that the flame structure and global consumption speed would become constant for high stretch flames. The insensitivity of high stretch C1 flames to flame height in Figure 4.6 and equivalence ratio in 4.3 seem to support this notion. Further study is needed to verify this theory.

Chapter 5

Summary and Conclusions

This chapter will provide a brief summary of the global consumption speed results reported in this study. This summary will focus on overall trends and differences in the global consumption speeds and stability limits between fuels. The chapter will finish with a discussion of the conclusions reached and their significance.

5.1   Summary of Results

Turbulent global consumption speeds for large-hydrocarbon fuels are reported in this work. Moreover, a methodology for the analysis of large-hydrocarbon fuels is presented. In summary, A2 has the highest turbulent flame speeds and largest stability range while C1 has the slowest turbulent flame speeds and smallest stability range. C5 has a lean stability limit between that of the other two fuels, but similar global consumption speeds to A2. The measurements show the global consumption speeds of large-hydrocarbon fuels are sensitive to fuel chemistry, despite similar heat release rates and laminar flame speeds. Moreover, this fuel sensitivity is evident from differences in the lean stability limits of the three fuels. Slower flame speeds and decreased stability ranges correspond to decreased aromatic content. This decreased stability and reduced global consumption speed is attributed to an increased sensitivity to flame stretch of low aromatic content fuels.

5.2 Conclusions

Five primary conclusions are reached:

1. The global consumption speed increases with increasing turbulence intensity for large-hydrocarbon fuels. This is attributed to a sensitivity of the global consumption speed to hydrodynamic stretch effects, resulting in greater flame wrinkling, as evidenced by the trends observed in Figure 4.4(a). This wrinkling results in a more compact flame and a decreased average flame area; thus, increasing the global consumption speed. This conclusion is supported by the observed decrease in non-dimensional leading point location with increased turbulence intensity in Figure 4.6(a).

2. The global consumption speed increases with increased bulk fluid velocity for large-hydrocarbon fuels. This is attributed to a sensitivity of the global consumption speed to curvature induced stretch effects. This increased curvature increases mass diffusion through the flame front and is in agreement with similar observations by Kobayashi et al. [29]. As the bulk velocity increases the flame area is increased, as shown in 4.6(a). This increased area results in a more negative global stretch rate as shown in Figure 4.6(b). As the magnitude of the stretch rate increases, the flame front thins; this thinning can result in an increase in species gradients across the flame front. The larger gradients increase mass diffusion through the flame front and subsequently increase the global consumption speed.

3. The global consumption speed of multi-component large-hydrocarbon fuels is sensitive to the chemical class of its components, even for fuels with similar laminar flame speeds and heat releases. This is attributed to the sensitivity of the global consumption speed to global stretch rate observed in Figure 4.6(b). The normalized global consumption speed of C1 is more sensitive to stretch rate than A2 and C5. Aromatic fuels have a weak sensitivity to flame stretch while alkane fuels have a strong sensitivity to flame stretch; this is highlighted in [4, 11, 19, 20, 32]. Both A2 and C5 are approximately 18% and 30% by mass aromatic fuels, respectively, while C1 has no aromatic content. Thus, it is plausible that aromatic content decreases a flame's sensitivity to stretch.

4. The stability of premixed large-hydrocarbon fuel/air flames is sensitive to chemical composition, even for fuels with similar flame speeds. This is attributed to an increased sensitivity to flame stretch. Flame stretch constitutes an energy loss

and lowers the flame temperature [2]. This reduced temperature weakens the flame structure at the tip and can cause it to break open in high stretch conditions.

5. The average Karlovitz number increases with Reynolds number, turbulence intensity, and aromatic content. The average Karlovitz number is found to be inversely proportional to the normalized global consumption speed. This is attributed to hydrodynamic– and curvature–based stretch effects. In light of the other conclusions, these trends indicate a strong coupling of flame stretch to turbulence and chemistry effects. This conclusion is important as it indicates that these effects are not isolated phenomena and should be considered together.

Chapter 6

Future Work

This document presents a study of the global consumption speed for large-hydrocarbon fuels. A sensitivity of the global consumption speed to fuel chemistry and flame stretch rate is discovered. However, further investigation is needed to understand the fundamental physics governing these observed sensitivities. These efforts should focus on four main areas:

1. Fully resolved three-dimensional turbulence statistics are needed to extend the scaling analysis of this work and determine how different turbulent time and length scales affect flame stretch effects. The current analysis from [22, 69] only examines the Taylor length scale; however, it is likely that smaller time and length scales are relevant and should be included in further analysis of the global consumption speed. This could be achieved through implementation of three-component hot-wire anemometry using a normal and yaw probe [75].

2. An improved laminar flame analysis is needed to develop additional scaling parameters such as the max-stretch laminar flame speed, laminar flame thickness, and laminar combustion time scales. These scaling parameters could further highlight chemistry effects in the global consumption speed. Implementation of this analysis is pending the completion and peer-review of the reaction mechanisms being developed by Xu et al. in [71].

3. Direct measurement of hydrodynamic instabilities in the flame front are needed to confirm the theorised physical basis for the observed sensitivities of the global

consumption speed to turbulence intensity. This could be achieved through time-resolved optical measurement of the flame front using the focused Schlieren techniques developed by Kobayashi et al. [29]. Such images would enable a study of which time and length scales are relevant to these stretch effects.

4. Time-resolved assessment of radical formation and species diffusion in the reaction front is needed to confirm the physical basis for the observed sensitivities of the global consumption speed to bulk flow velocity. It is plausible that increased bulk fluid velocities increase the overall flame curvature which increases stretch and thins the flame front. Time-resolved OH-PLIF, similar to the techniques developed by Kobayashi et al. [29] could be implemented to quantify if and how much the flame thins with increased flame curvature. These images would validate the theory that the corresponding increase of the global consumption speed with increased bulk fluid velocity is the result of increased mass diffusion caused by increased flame curvature.

Appendix A

Experimental Schematics and Materials

A.1   Plumbing & Instrumentation Diagram

A.2   Electrical Schematic

Repeat 5 Time

Repeat 3 Time

Temperature
Controller
+   −

SSR

Heater

Temperature
Controller
+   −

SSR

Heater

E-STOP

120 VAC
20 A

240 VAC
30 A

Stator
Relay
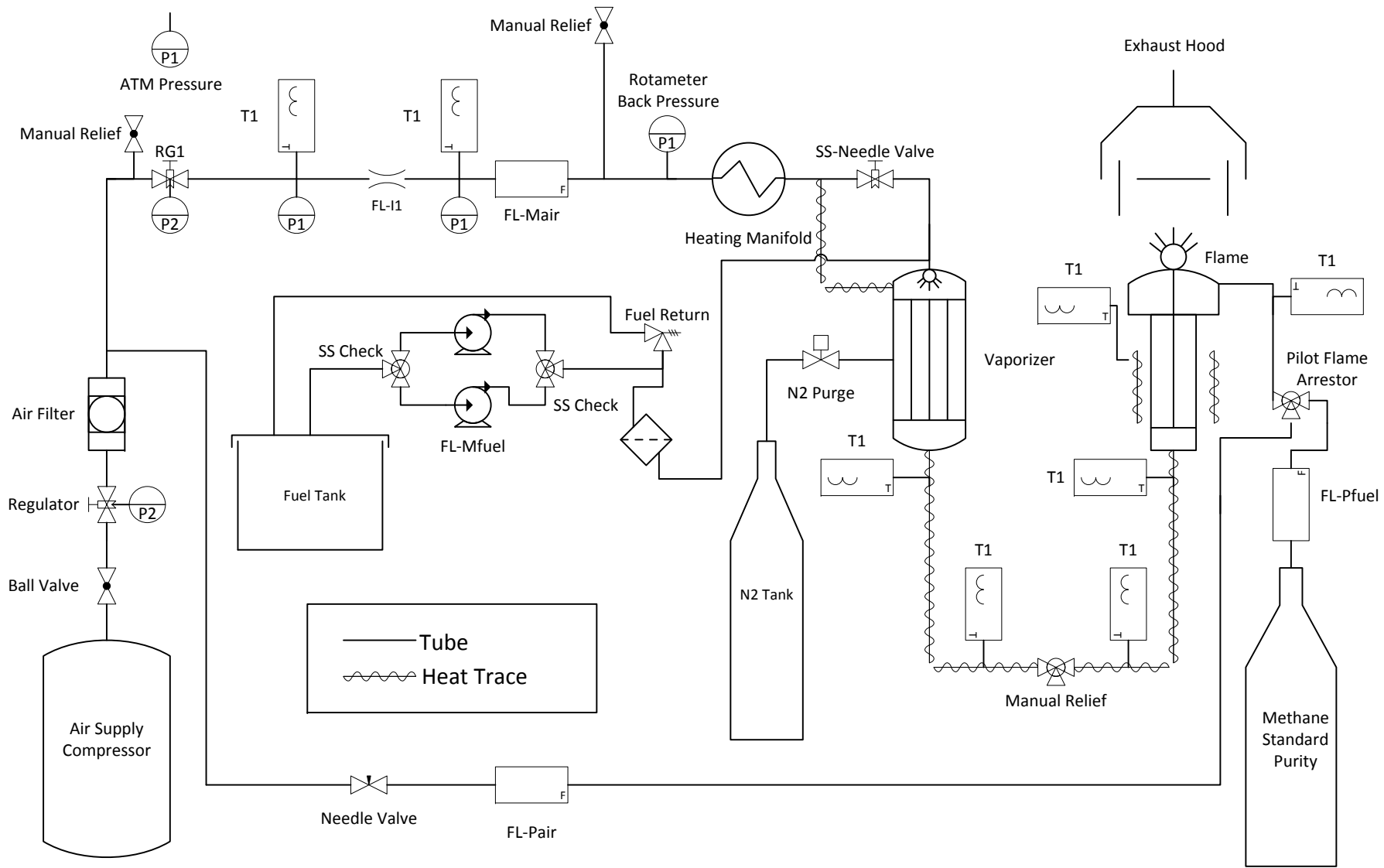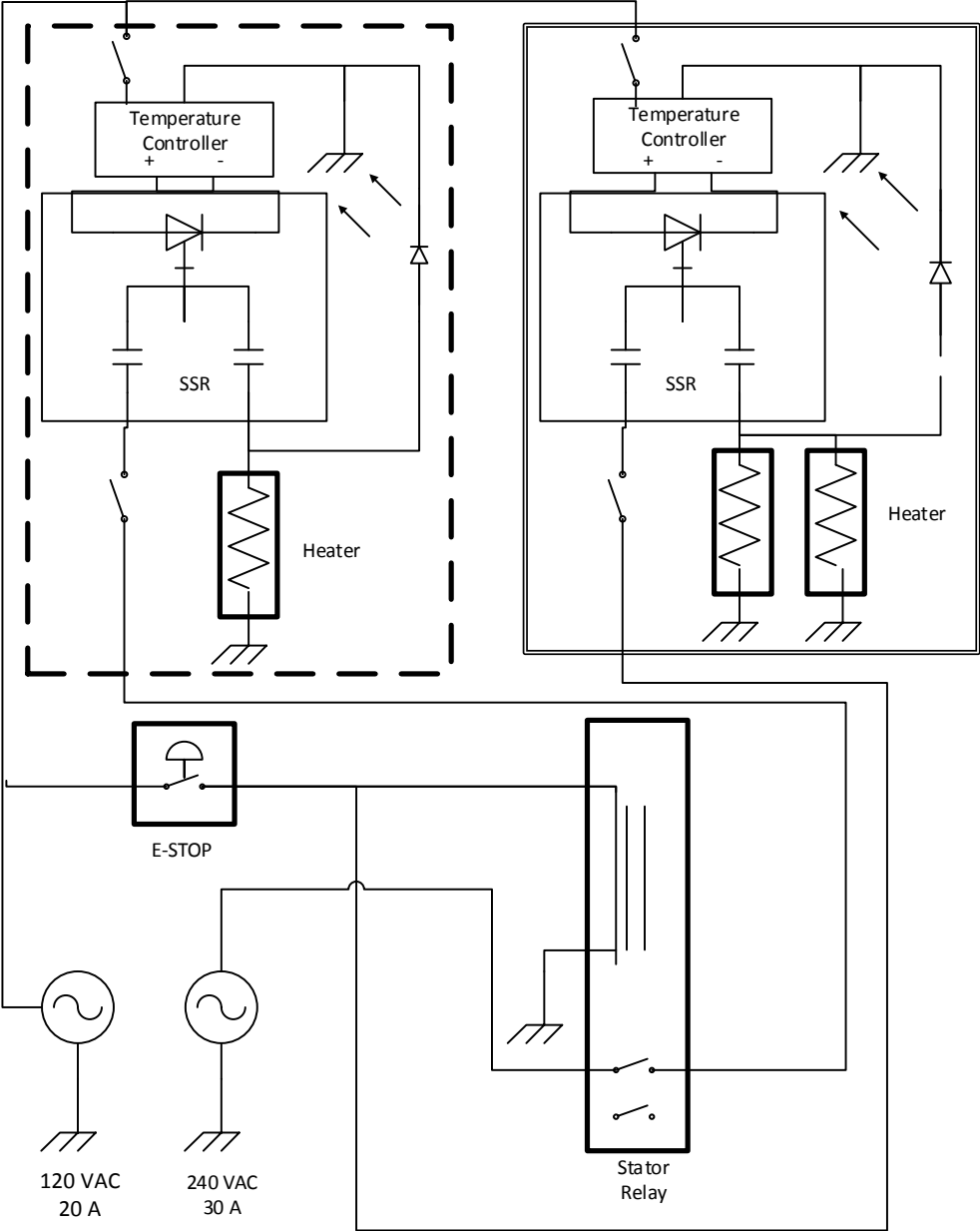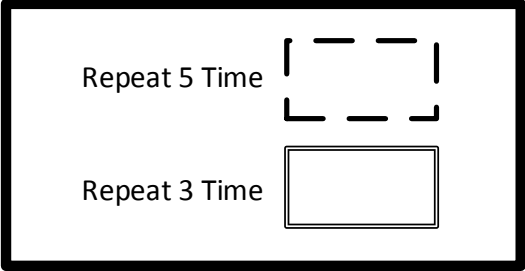
A.3   Bill of Materials with Uncertainty

Assembly	P&ID	Part	Part Description	Uncertainty	Manufacturing	Material	Dimensions	Vendor	Quantity
Vaporizer		End Cap	Ø7.5" x .75" LG		Maual Mill - Quote	SS 304	PL .75" X 8" X 8"	MIME Shop	1
		Baffle Plate	Ø3.95" x .125" LG		Maual Mill - Quote	Al 2024	PL .125" x 5" x 5"		1
		End Flange	Ø7.5" x .5" LG		Maual Mill - Quote	SS 304	PL .5" X 8" X 8"		1
		Cone End Cap	Ø7.5" x 3.75" LG		CNC - Quote	SS 304	Ø7.5" X 3.75" LG		1
			Ø5" x 3.25" LG		CNC - Quote	SS 304	Ø5" x 3.25" LG		1
			Ø7.5" x .5" LG		CNC - Quote	SS 304	PL .5" X 8" X 8"		1
		Nozzle Pipe	Ø.75" x 6" LG		Standard Part	SS 304			1
		Canister	4" SCHED 40 Pipe x 8" LG (4.5" OD x 4" ID)		Standard Part	SS 304	4" SCH 40 x 8"	Discount Steel	1
Nozzel		Sinter Plate retainer	Retaining ring for porous pilot plate		CNC - Quote	SS 316		MIME Shop	1
		Inner Niozzel	Inner burner nozzel		CNC - Quote	SS 316			1
		Outer Nozzel	Outer burner nozzel		CNC - Quote	SS 316			1
		Sinter Plate	McMaster-Carr PN 9446T35 Select the 5 µm size					McMaster-Carr	2
Plenum		Bottom Disk	Ø5" x .25" LG		CNC or Waterjet	SS 304	PL .25" X 5.5" X 5.5"	Discount Steel	1
		Middle Disk	Ø4.375" x .25" LG		CNC or Waterjet	SS 304	PL .25" X 5" X 5"	Discount Steel	2
		Top Disk	Ø4.375" x .375" LG		CNC or Waterjet	SS 304	PL .375" X 5" X 5"	Discount Steel	1
		Turbulence generator	Turbulence generator		WIRE EDM, Mill, Weld	SS 304		Discount Steel	1
		Bottom Tube	3" SCHED 40 Pipe x 3.225" LG (3.5" OD x 3.07" ID)		Manual Lathe	SS 304	3" SCH 40 X 3.5"	Discount Steel	1
		Top Tube	3" SCHED 40 Pipe x 5.975" LG (3.5" OD x 3.07" ID)		Manual Lathe	SS 304	3" SCH 40 X 6"	Discount Steel	1
Flow	FL-Pair	FL-3696ST	Rotameter 12,058 cc/min of air - Piliot	+/-2% FS				Omega	1
	FL-N2	FL2092	Regulator 4 to 50 SCFM of Air, with plastic integral gate valve	+/- 2% FS				Omega	1
	FL-Mair	FL4611-V	Rotameter 8.5 SCFM Max Flow of Air, 1/2 FNPT	+/- 2% FS +/-.5% repeatability				Omega	2
	FL-Pfuel	M100B-2000	MKS Thermal Mass flow meter 2000 sccm	+/- 1% FS				MKS	2
	FL-Mfuel	100DX Syringe Pump	Isco High-Precision, High-Pressure Syringe Pumps	+/- 0.5% set point				Teledyne Isco	1
Therocouple	T1	KQXL-116G-12	Gounded 1/16in Dia. 12in L	+/- 2% FS		SS 316		Omega	12
Pressure	P1	PX309-100GV	100 psi gage pressure range, cable connection output	+/-.25%		SS 316		Omega	4
	P2	PGS-25B-160	2½ inch general service gauge with back fitting and 0-160 psig range					Omega	2
Heaters		HBT-4411	Band heater, 1100 W, 4.5" Dia X 2" width					Omega	3
Flow Indicator	FL-I1	P/N: 2822T17 0.063"	303 Stainless Flow-Control Orifice 1/2" NPT pipe fitting- High flow rates			SS 316		McMaster-Carr	2
	FL-I2	P/N: 2822T17 0.038"	303 Stainless Flow-Control Orifice 1/2" NPT pipe fitting- Low flow rates			SS 316		McMaster-Carr	2
Tube		Main Air	10 ft ASTM A269-10 304 Stainless Steel Welded Round Tube 1/2" x 18ga			SS 316	1/2" x 18ga	Discount Steel	1
		Pilot Fuel and fule inlet	5 ft ASTM A269-10 304 Stainless Steel Welded Round Tube 1/4" x 18ga			SS 316	1/4" x 18ga	Discount Steel	1
		Air line	10 ft High-Pressure PVC Tubing, Food, 1/2" ID, 3/4" OD, 1/8" Wall Thickness			SS 316	1/2" ID, 3/4" OD	McMaster-Carr	1
Fittings			Misc.					McMaster-Carr	
Regulators	RG-1	PRG200-120	2 to 120 psi (0.14 to 8.27 bar) output pressure range, manual	+/0.1%				Omega	2
Motor		23HS20-2004S	Nema 23 Bipolar Stepper Motor 2.0A 0.9Nm(127.5oz.in)					Stepperonline	1
Encoder		MA3-P12-250-N	A2 Absolute magnetic Encoder					US Digital	1
Motor Controller		ST-712	Bipolar Stepper Motor Driver Max 3A Current 128 High Subdivision					Stepperonline	1
Power Supply			12 Volt DC power supply						1
Fuel Cell		SUM-293205	Fuel Cell, Aluminum, Natural, 5 Gallons					Summit Racing Eq.	1
Fuel line Adaptor		EAR-916107ERL	Fitting, Straight, -8 AN Female to 1/4 in. NPT Male, Aluminum, Blue Anodized, Each					Summit Racing Eq.	4
Electrical Misc.			Cosmos ® 20 PCS mini Aluminum Chips VGA RAM Cooling Heatsinks heat sink cooler + Cosmos Cable Tie					Amazon	1
		Adriono Uno 3	Arduino Micro Controler					Arduino	1
		Dev-12646	Teensy 3.1 Dev-12646 ROHS					Spark Fun	1
		8075T3	Two-Stage Particle- & Oil-Removal Air Filter, 1/2 Pipe Size, 36 Maximum scfm @ 100 PSI					McMaster-Carr	1
		4833K21	Gasoline and Diesel Fuel Filter 3/4 Pipe Size					McMaster-Carr	1

Part #	Part Description	Material	Vendor	Quantity
SS-200-1-1	1/8 MNPT to 1/16 swage	SS	Swagelok	5
SS-810-1-8	1/2 MNPT to Swage	SS	Swagelok	3
SS-810-3	1/2 swage T with 1/4 branch	SS	Swagelok	1
SS-810-9	1/2 swage elbow	SS	Swagelok	1
SS-400-1-4	1/4 MNPT to swage	SS	Swagelok	6
SS-810-1-6	3/8 MNPT to 1/2 swage	SS	Swagelok	1
SS-400-3	1/4 Swage t	SS	Swagelok	4
SS-400-6	1/4 swage union	SS	Swagelok	2
SS-400-9	1/4 swage elbow	SS	Swagelok	2
SS-403-1	1/4" swage ferrol	SS	Swagelok	10
SS-103-1	1/16" swage ferrol	SS	Swagelok	10
SS-810-6-4	1/2" swage to 1/4" swage reducing union	SS	Swagelok	3
SS-810-1-8	1/2" swage to 1/2" MNPT union	SS	Swagelok	11
SS-810-1-6	1/2" swage to 3/8" MNPT union	SS	Swagelok	1
SS-810-1-4	1/2" swage to 1/4" MNPT union	SS	Swagelok	9
SS-810-7-8	1/2" swage to 1/2" FNPT union	SS	Swagelok	4
SS-810-7-6	1/2"swage to 3/8" FNPT union	SS	Swagelok	6
SS-400-1-8	1/4" swage to 1/2" MNPT	SS	Swagelok	1
SS-400-1-4	1/4" swage to 1/4" MNPT union	SS	Swagelok	4
SS-400-7-6	1/4" swage to 3/8" FNPT	SS	Swagelok	1
SS-400-7-2	1/4" swage to 1/8" FNPT	SS	Swagelok	2
SS-400-1-OR	1/4" swage to 7/16-20 UNF (O-Seal)	SS	Swagelok	4
SS-200-1-2	1/8" swage to 1/8" MNPT union	SS	Swagelok	2
SS-810-3	1/2" swage T	SS	Swagelok	8
SS-810-3-8-4	1/2" swage T with 1/4" swage Branch	SS	Swagelok	4
SS-810-3-8-1	1/2" swage T with 1/16" swage Branch	SS	Swagelok	10
SS-810-3-4TTF	1/2" swage T with 1/4" FNPT branch	SS	Swagelok	4
SS-400-3	1/4" swage T	SS	Swagelok	2
SS-200-3	1/8" swage T	SS	Swagelok	1
SS-810-4	1/2" swage cross union	SS	Swagelok	2
SS-810-9	1/2" swage elbow	SS	Swagelok	8
SS-AFSS8	1/2" swage Ball Valve	SS	Swagelok	2
SS-812-1	1/2" swage nut	SS	Swagelok	4
SS-402-1	1/4" swage nut	SS	Swagelok	5
SS-102-1	1/16" swage nut	SS	Swagelok	5
SS-813-1	1/2" swage ferrol	SS	Swagelok	4

Appendix B

Uncertainty Propagation Example Calculations

Global Consumption Speed
Uncertainty Propagation

$$S_{T,GC} = \frac{\dot{m}_u}{\rho_u \bar{A}_{\langle c \rangle}}$$

$$\dot{m}_u = \left(\dot{V}_a \rho_a + \dot{V}_F \rho_F \right)$$
$$\frac{\partial S_{T,GC}}{\partial \dot{m}_u} = \frac{1}{\rho_u \bar{A}_{\langle c \rangle}}$$

$$\rho_u = \rho_F Y_F + \rho_a Y_a$$
$$\frac{\partial S_{T,GC}}{\partial \rho_u} = \frac{-\dot{m}_u}{\rho_u^2 \bar{A}_{\langle c \rangle}}$$

$$\bar{A}_{\langle c \rangle} = \pi r \sqrt{h^2 + r^2}$$
$$\frac{\partial S_{T,GC}}{\partial \bar{A}_{\langle c \rangle}} = \frac{-\dot{m}_u}{\rho_u \bar{A}_{\langle c \rangle}^2}$$

$\dot{V}_a$
$$\frac{\partial \dot{m}_u}{\partial \dot{V}_a} = \rho_a$$

ρ_a
$$\frac{\partial \dot{m}_u}{\partial \rho_a} = \dot{V}_a$$

$\dot{V}_F$
$$\frac{\partial \dot{m}_u}{\partial \dot{V}_F} = \rho_F$$

ρ_F
$$\frac{\partial \dot{m}_u}{\partial \rho_F} = \dot{V}_F$$

r
$$\frac{\partial \bar{A}_{\langle c \rangle}}{\backslash partial r} = \frac{\pi (h^2 + 2r^2)}{\sqrt{h^2 + r^2}}$$

h
$$\frac{\partial \bar{A}_{\langle c \rangle}}{\partial h} = \frac{\pi h r}{\sqrt{h^2 + r^2}}$$

U_{rota} | T_∞ P_∞ | U_{rota} | T_∞ | U_r | U_h

U_T U_P | U_T

Y_a
$$\frac{\partial \rho_u}{\partial Y_a} = \rho_a$$

ρ_a
$$\frac{\partial \rho_u}{\partial \rho_a} = Y_a$$

Y_F
$$\frac{\partial \rho_u}{\partial Y_F} = \rho_F$$

ρ_F
$$\frac{\partial \rho_u}{\partial \rho_F} = Y_F$$

U_{stoic} | T_∞ P_∞ | U_{stoic} | T_∞

U_T U_P | U_T
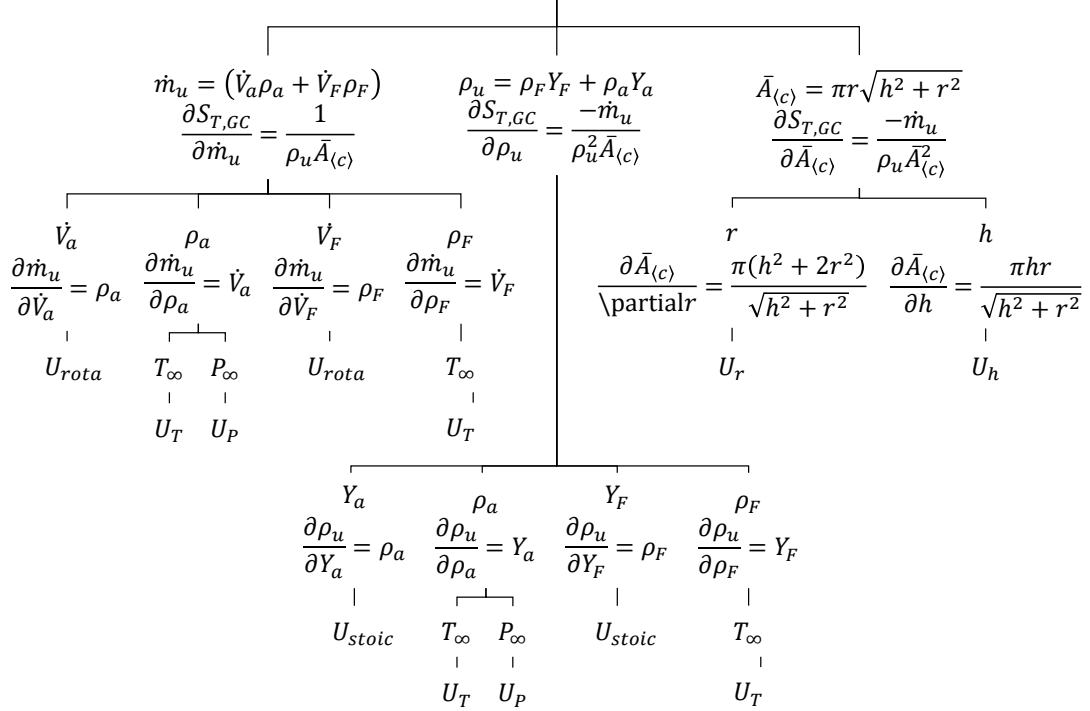
Global Stretch Rate
Uncertainty Propagation

$$\bar{\kappa}_{\langle c \rangle} = \frac{-U_0 \sin(2\alpha_{\langle c \rangle})}{2r}$$

$$U_o = \frac{\dot{m}_u}{\rho_u A_D}$$
$$\frac{\partial \bar{\kappa}_{\langle c \rangle}}{\partial U_o} = -\frac{\sin(2\alpha)}{2r}$$

r
$$\frac{\partial \bar{\kappa}_{\langle c \rangle}}{\partial r} = -\frac{U_o \sin(2\alpha)}{2r^2}$$

$$\alpha_{\langle c \rangle} = \tan^{-1} \frac{r}{h}$$
$$\frac{\partial \bar{\kappa}_{\langle c \rangle}}{\partial \alpha} = -\frac{U_o \sin(2\alpha)}{2r^2}$$

$\dot{m}_u$
$$\frac{\partial U_o}{\partial \dot{m}_u} = \frac{1}{\rho_u A_D}$$

ρ_u
$$\frac{\partial U_o}{\partial \rho_u} = \frac{\dot{m}_u}{\rho_u^2 A_D}$$

$$A_D = \frac{\pi D^2}{4}$$
$$\frac{\partial U_o}{\partial A_D} = \frac{\dot{m}_u}{\rho_u A_D^2}$$

U_r

r
$$\frac{\partial \alpha_{\langle c \rangle}}{\partial r} = -\frac{r}{h^2 + r^2}$$

h
$$\frac{\partial \alpha_{\langle c \rangle}}{\partial h} = \frac{h}{h^2 + r^2}$$

$U_{\dot{m}_u}$ | U_{ρ_u} | U_r | U_h

D
$$\frac{\partial A_D}{\partial D} = \frac{\pi D}{2}$$

U_D
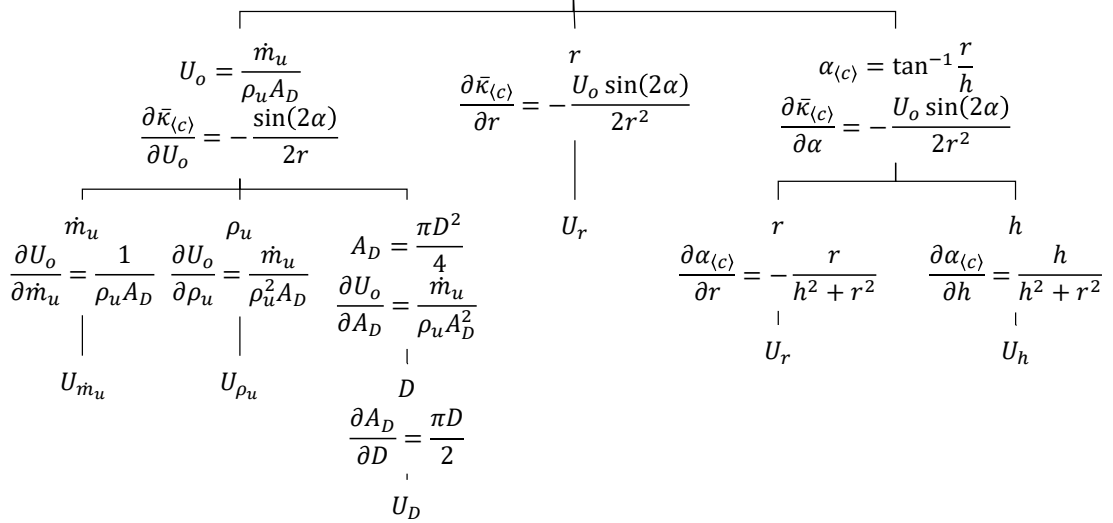
Global Karlovitz Number
Uncertainty Propagation

$$\overline{Ka}_{\langle c \rangle} = \frac{l_T}{S_{L,0}} \bar{\kappa}_{\langle c \rangle}$$

$S_{L,0}$

$$\frac{\partial \overline{Ka}_{\langle c \rangle}}{\partial S_{L,0}} = \frac{-l_T}{S_{L,0}^2} \bar{\kappa}_{\langle c \rangle}$$

$U_{S_{L,0}}$

l_T

$$\frac{\partial \overline{Ka}_{\langle c \rangle}}{\partial l_T} = \frac{\bar{\kappa}_{\langle c \rangle}}{S_{L,0}}$$

U_{l_T}

$\bar{\kappa}_{\langle c \rangle}$

$$\frac{\partial \overline{Ka}_{\langle c \rangle}}{\partial \bar{\kappa}_{\langle c \rangle}} = \frac{l_T}{S_{L,0}}$$

$U_{\bar{\kappa}_{\langle c \rangle}}$

Appendix C

Image Processing MATLAB Code

C.1 Spatial Calibration Code

```matlab
1   clear
2   clc
3   close all
4
5   %% Add path to functions for calculating laminare and turbulent flame
        speeds.
6   % Not currently used this is left over from GTI-code and will be worked in
7   %
8   Codepath = 'C:\Users\AJ\Google Drive\A Research Folder\GT Burner\
        AbelTransformCodes';
9   Datapath = 'C:\Users\AJ\Documents\A Research Folder\Masters_Thesis\Flame
        Data\C1';
10  addpath 'C:\Users\AJ\Google Drive\A Research Folder\GT Burner\
        AbelTransformCodes';
11  addpath 'C:\Users\AJ\Documents\A Research Folder\Masters_Thesis\Flame Data\
        C1';
12  % addpath 'Z:\Chemkin\UnStrainedAnalysis\FlameSpeedandThickness'
13  %
14  bg_path = 'C:\Users\AJ\Documents\A Research Folder\Masters_Thesis\Flame
        Data\C1\Background.tiff';
15  Cal_path = 'C:\Users\AJ\Documents\A Research Folder\Masters_Thesis\Flame
        Data\C1\Calibration_2.tiff';
16  numsamples = 1;
17  numframes = 360*numsamples;                    %Set number of frames from
        camera settings
18  home = pwd;
19
20  fg_path = 'C:\Users\AJ\Documents\A Research Folder\Masters_Thesis\Flame
        Data\C1\RE10000_PHI085_C1_POSF11489_1.tiff';
21  % fg_path = 'D:\Users\Public\Documents\GTI burner\DATA\Turbulent Flame Data
        DO NOT DELETE\5-11-15\RE10000_PHI1_A2_POSF10325_1.tiff';
22  % fg_path_1 = 'D:\Users\Public\Documents\GTI burner\DATA\Turbulent Flame
        Data DO NOT DELETE\5-11-15\RE10000_PHI1_A2_POSF10325_1.tiff';
23  % fg_path_2 = 'C:\Users\AJ\Documents\GT Burner\Data\Turbulent Flame Data DO
        NOT DELETE\5-15-2015\RE10000_PHI09_A2_POSF10325_2.tiff';
24  % fg_path_3 = 'C:\Users\AJ\Documents\GT Burner\Data\Turbulent Flame Data DO
        NOT DELETE\5-15-2015\RE10000_PHI09_A2_POSF10325_3.tiff';
25  % fg_path_4 = 'D:\Users\Public\Documents\GTI burner\DATA\5-06-15\
        RE10000_PHI1_10.tiff';
26
27  %% Input Parameters
28  m_dot_total = 0.0024;
29  rho_u = 0.7817;
30  D       = 12;                          %Burner Diameter
31  % P       = 20;                          %Some stirng variable input for
        naming convention GTI
32  % T       = 300;                         %Some stirng variable input for
        naming convention GTI
33  % U       = 07;                          %Mean velocity input for naming
        convention GTI
34  phi     = 0.9;                         %Equivalence ratio used in file naming
        convention GTI
35  fuel    = 'Jet-A';                     %String Speciying Fuel used in file
        nameing convention GTI
```

```matlab
36  % angle    = [ 0 , 6 , 12 , 18 , 24];   %Angle of turbulence generator will
        call callibration data
37  % expdate = '20130329';                  %Used in naming convention GTI date?
38  % expt    = 'ERSweeps';                   %Used in naming convention GTI type?
39  % runs = [1 2 3 4 5 8];                   %Runs of interest not currently used
40  run_BG = 8;                               %Background Run − Change to string
41
42  %% Laminar Flame data
43  % Need to determine if SL_ref or SL is appropriate talk to Blunck/Niemeyer
        about
44  % how to develope database
45
46  % SL =                                    %Something will go here
47
48  %% Image Parameters − Selected From Image
49  flame_img = imread(Cal_path);
50
51  % flame_img = imadjust(flame_img,[.05  0.2],[]);
52  figure
53  % flame_img = imadjust(flame_img,[0.3  0.7],[]);
54  imshow(flame_img)
55  colormap('Bone')
56  axis image
57  title('Select Left edge, Right Edge, Bottom')
58  [x_flame,y_flame] = ginput(3);
59  Lf                        = x_flame(1);
                                               % left edge of the flame
60  Rf                        = x_flame(2);
                                               % right edge of the flame
61  Bcrop                     = y_flame(3);
                                                % location for cropping of the
        top of the image
62  % Tcrop                   = y_flame(4);
                                               % pixel location of the burner
        lip: y−location
63
64  imshow(flame_img)
65  colormap('bone')
66  axis image
67  title('Select Left edge, Right Edge of calibration device')
68  [x_cal,y_cal] = ginput(2);
69  Left                      = x_cal(1);
                                                    % location of left line on
        calibration device
70  Right                     = x_cal(2);
                                                % location of right line on
        calibration device
71
72  %% Image Parameters − User Selected
73  %Comment out Lf Rf Bcrop Tcrop Length Right and Left for spacial
74  %calibration determination
75
76  % Lf                      = 413.4548;
                                                % left edge of the flame
77  % Rf                      = 608.3502;
                                               % right edge of the flame
```

```
78  % Bcrop                    = 958.2036;
                                                    % location  for  cropping  of
          the  top  of  the   image
79  Tcrop                      = 1;                                                    %
          pixel  location  of  the  burner  lip :  y−location
80  C                          = ( Lf + Rf )/2;
                                                    % center  of  burner
81  % length                   = 0.787 ∗ 0.0254;
                                                    % length  from  calibration  device  (
          cm)
82  diameter = 0.0254;
                                                                          % use
          if  no  calibration  image
83  % Left                     = 475;
                                                    % location  of  left  line
          on  calibration  device
84  % Right                    = 546.0476;
                                                    % location  of  right
          line  on  calibration  device
85  pixels                     = Right − Left ;
86  Calibration                = diameter / pixels ;
                                                    % meters / pixel
87  R                          = 0.008;
                                                    % radial  distance  (cm)
          from  center  to  crop  on  left  and  right  side
88
89  %% Preparation  and  Calibration
90  % Calibration  for  turbulence  generator
91
92  % numRuns                  = length ( angle );
                                                    % enter  the  number  of  runs
93  % BR                       = 0.9852.∗ angle + 68.967;
                                                    % blockage  ratio  at  each  angle
94  %
95  % if  D == 12
96  % %    ODm = 13.335e−3;
                                                                          % OD of  inner
          part  of  burner  lip  (m)
97  % %     ODm = 35.56e−3;
                                                                          % OD of  burner
          lip  (m)
98  %     urms                 = ( 0.0029405 .∗ BR − 0.084321 ) .∗ U;
                              % urms  at  each  angle
99  % elseif  D == 20
100 % %    ODm = 41.7e−3;
                                                                          % OD of  burner
          lip  (m)
101 %     urms                 = ( 0.0036 .∗ BR − 0.1128 ) .∗ U;
                              % urms  at  each  angle
102 % else
103 %     error ('This  is  not  a  recognized  burner  diameter ');
104 % end
105
106 %% Calculate  radius  and  volume  flow  rate
107 % Change  to  valumetric  flow  rate  from  data
108 % USE MASS FLOW AND UNBURNED DENSITY
109
```

```matlab
110  r                          =  (D/2)*10^-3;
                                          % burner  radius  (m)
111  v_dot                      =   m_dot_total/rho_u;%pi*r^2*U;
                                          % volume  flowrate  (m^3/s)
112
113  %% Image Read In , Average ,  and  Background  Subtract
114  % add  for  loop  to  repeat  for  number  of  runs  as  needed .
115  info  =  imfinfo ( fg_path );
116  num_images  =  numel ( info );
117  for  i  =  1:360
118       fg_image ( : , : , i )  =  imread ( fg_path , i , 'Info ' , info );
119  %       fg_image ( : , : , i+360)  =  imread ( fg_path_2 , i , 'Info ' , info );
120  %       fg_image ( : , : , i+720)  =  imread ( fg_path_3 , i , 'Info ' , info );
121  %       fg_image ( : , : , i+1080)  =  imread ( fg_path_4 , i );
122       bg_image ( : , : , i )  =  imread ( bg_path , i , 'Info ' , info );
123  end
124  MeanImg  =  sum ( fg_image ,3 )/numframes ;
125  Mean_bg  =  sum ( bg_image ,3 )/360;
126  BG_sub  =  MeanImg−Mean_bg ;
127  figure
128  image (BG_sub )
129  %% Image crop  dimensions
130  [ ydim ,  xdim ,  cases ]  =  size (MeanImg );
131
132  Lcrop                      =  floor (C  −  (1/ Calibration )*R );                      %
         location  for  cropping  on  left  side  of  image  (0.5  cm from  OD  of  burner
         lip )
133
134  if  Lcrop  <  1
135       error ( 'Cropping  domain  is  larger  than  actual  image ');
136  end
137
138  Rcrop                      =  floor (C  +  (1/ Calibration )*R );                      %
         location  for  cropping  on  right  side  of  image  (0.5  cm from  OD  of  burner
         lip )
139  if  Rcrop  >  xdim
140       error ( 'Cropping  domain  is  larger  than  actual  image ');
141  end
142
143  ImCrop  =  BG_sub ( ceil (Tcrop ): ceil (Bcrop ),   ceil (Lcrop ): ceil (Rcrop ));
         % crop  the  image
144  Intensity   =  ImCrop ;
145  figure
146  image ( ImCrop )
147  axis  image
148  %% Axisymmetrize  the  image  by  averaging  both  sides
149
150  Axisym  =  0.5*( Intensity ( : ,  1:end)  +  Intensity ( : ,  end + 1  −  (1:end))));
151  [ f ,  g ]  =  size (Axisym ( : ,  : ));                                                  %
         get  dimensions  of  the  axisymmetrized  image
152
153  %% Perform  median  filter  on  images
154
155  ImageFilt  =  Axisym ;
156  % for  i  =  1:numRuns
157       ImageFilt ( : ,  : )  =  medfilt2 (Axisym ( : ,  : ),  [5  5]);
158  % end
159  %% Extract  the  centerline  intensity  of  the  filtered  axisym  image
```

```matlab
160
161  CL_axisym = zeros(f,1);
162  % for i = 1:numRuns
163      CL_axisym(:,1) = ImageFilt(:, round(g/2));
164  % end
165
166  CL_axisym = flipud(CL_axisym);
167
168  %% Perform the Abel Transform to each image
169
170  ImageAbel = ImageFilt;
171  % for i = 1:numRuns
172      ImageAbel(:, :) = abeltransform(ImageFilt(:, :));
173  % end
174  IA = ImageAbel;
175  %% Create array of centerlines for each Abel transformed image
176
177  CL = zeros(f,1);
178  % for i = 1:numRuns
179      CL(:) = ImageAbel(:, round(g/2));
180      CL = bwfilter(CL, 1 : length(CL), 0.01);
181  % end
182
183  CL = flipud(CL);
184
185  %% Fit Gaussian to each centerline and find maximum location
186
187  GF        = zeros(f,1);
188  H         = zeros(1);
189  ft        = fittype('gauss1');
190  options = fitoptions('gauss1');
191  pxl       = (1:f)';
                                                              % create
          pixel location vector
192  met       = pxl*Calibration;                            % convert pixel
          location vector into meters
193
194  % for i = 1:numRuns
195      curvefit          = fit(pxl, CL(:), ft, options);               %
              create fit model
196      GF(:)           = curvefit(pxl);                                %
              evaluate fit model for pixel vector
197      [GFmax, I]        = max(GF(:));                                 %
              find the magnitude and location of the maximum value of the
              Gaussian
198  %      GFnorm(:, i)     = GF(:, i)/GFmax;
                                                              % normalize the gaussian by the
          maximum value
199      H               = I*Calibration;                              %
              convert the location of the maximum into meters instead of pixels
200  % end
201
202  %% Calculate flame speeds from H
203
204  s               = (H.^2 + r^2).^(0.5);
205  ConeArea       = pi*r*s;
206  ST              = v_dot./ConeArea;
```

```
207  % ST_SL       = ST/SL;
208  % urms_SL     = urms ./ SL;
209
210
211  %% Plot
212
213  % newdir = [currdir,'\PlotsAndAnalysis'];
214  % cd(newdir)
215
216  lwidth  = 1.5;
217  fsize   = 14;
218
219  % for i = 1:numRuns
220      figure;
221      set(gcf, 'color', 'w');
222      subplot(1,4,1); imagesc(Intensity(:, :)); axis image; set(gca, '
          FontSize', fsize, 'FontName', 'Times'); title('Cropped');
223          y = ylim;
224          label = fliplr([y(2)-.012/Calibration y(2)-(.012*2)/Calibration y
              (2)-(.012*3)/Calibration y(2)-(.012*4)/Calibration y(2)
              -(.012*5)/Calibration...
225              y(2)-(.012*6)/Calibration y(2)-(.012*7)/Calibration y(2)
                  -(.012*8)/Calibration y(2)-(.012*9)/Calibration y(2)
                  -(.012*10)/Calibration y(2)-(.012*11)/Calibration...
226              y(2)-(.012*12)/Calibration]);
227          set(gca,'ytick',label)
228          set(gca,'yticklabel',[12 11 10 9 8 7 6 5 4 3 2 1])
229          ylabel('l/d')
230          [Row Col] = size(Intensity);
231          set(gca,'xtick',[Col/2-.006/Calibration Col/2 Col/2+.006/
              Calibration])
232          set(gca,'xticklabel',[-0.5 0 0.5]);
233          xlabel('x/d')
234      subplot(1,4,2); imagesc(Axisym(:, :)); axis image; set(gca, 'FontSize',
           fsize, 'FontName', 'Times'); title('Axisymmetric');
235          set(gca,'yticklabel',[])
236          set(gca,'xtick',[Col/2-.006/Calibration Col/2 Col/2+.006/
              Calibration])
237          set(gca,'xticklabel',[-0.5 0 0.5]);
238          xlabel('x/d')
239      subplot(1,4,3); imagesc(ImageFilt(:, :)); axis image; set(gca, '
          FontSize', fsize, 'FontName', 'Times'); title('Filtered');
240          set(gca,'xtick',[Col/2-.006/Calibration Col/2 Col/2+.006/
              Calibration])
241          set(gca,'xticklabel',[-0.5 0 0.5]);
242          xlabel('x/d');
243          set(gca,'yticklabel',[])
244      subplot(1,4,4); imagesc(ImageAbel(:, :)); axis image; set(gca, '
          FontSize', fsize, 'FontName', 'Times'); title('Abel Transformed');
245          set(gca,'xtick',[Col/2-.006/Calibration Col/2 Col/2+.006/
              Calibration])
246          set(gca,'xticklabel',[-0.5 0 0.5]);
247          xlabel('x/d')
248          set(gca,'yticklabel',[])
249  %     fn = ['Images_', num2str(U), '_', num2str(angle(i)), '_', num2str(D),
          'mm'];
250  %      saveas(gcf, [fn '.fig']);
251  %      saveas(gcf, [fn '.png']);
```

```matlab
252         figure;
253         set(gcf, 'color', 'w');
254         plot(100*met, CL, 'r', 100*met, GF, 'b', 'LineWidth', lwidth);
255         set(gca, 'FontSize', fsize, 'FontName', 'Times');
256         xlabel('axial location (cm)');
257         ylabel('Intensity');
258 %       fn = ['Intensity_', num2str(U), '_', num2str(angle(i)), '_', num2str(
        D), 'mm'];
259 %       saveas(gcf, [fn '.fig']);
260 %       saveas(gcf, [fn '.png']);
261 % end
262
263  figure;
264  set(gcf, 'color', 'w');
265
266 % for  i = 1:numRuns
267      subplot(111); imagesc(ImageFilt(:, :)); axis image; set(gca, 'FontSize'
            , fsize, 'FontName', 'Times'); title('Axisym');
268 %      subplot(1,numRuns,i); imagesc(ImageFilt(:, :, i)); axis image; set(
        gca, 'FontSize', fsize, 'FontName', 'Times'); title('Axisym');
269 % end
270
271 % fn = ['AxisymImages_', num2str(U), '_BRSweep_', num2str(D), 'mm'];
272 % saveas(gcf, [fn '.fig']);
273 % saveas(gcf, [fn '.png']);
274
275  figure;
276  set(gcf, 'color', 'w');
277
278 % for  i = 1:numRuns
279      subplot(111); imagesc(ImageAbel(:, :)); axis image; set(gca, 'FontSize'
            , fsize, 'FontName', 'Times'); title('Abel Transformed');
280
281 %      subplot(1,numRuns,i); imagesc(ImageAbel(:, :, i)); axis image; set(
        gca, 'FontSize', fsize, 'FontName', 'Times'); title('Abel Transformed')
        ;
282 % end
283
284 % fn = ['AbelImages_', num2str(U), '_BRSweep_', num2str(D), 'mm'];
285 % saveas(gcf, [fn '.fig']);
286 % saveas(gcf, [fn '.png']);
287
288 % for  i = 1:numRuns
289      figure;
290      set(gcf, 'color', 'w');
291      plot(100*met, CL ./ max(CL), 'r', 'LineWidth', lwidth); hold on
292      plot(100*met, CL_axisym ./ max(CL_axisym), 'b', 'LineWidth', lwidth);
            hold off
293      set(gca, 'FontSize', fsize, 'FontName', 'Times');
294      xlabel('axial location (cm)');
295      ylabel('Intensity');
296      legend('Abel Transformed Centerline', 'Axisym Image Centerline', '
            FontSize', fsize, 'FontName', 'Times')
297 %      fn = ['IntensityComparison_', num2str(U), '_', num2str(angle(i)), '_
        ', num2str(D), 'mm'];
298 %      saveas(gcf, [fn '.fig']);
299 %      saveas(gcf, [fn '.png']);
300 % end
```

```matlab
301
302  % figure;
303  % set(gcf, 'color', 'w');
304  % plot(urms_SL , ST_SL, 'go', 'LineWidth', lwidth);
305  % set(gca, 'FontSize', fsize , 'FontName', 'Times');
306  % xlabel('u'' _r_m_s / S_L_, _0');
307  % ylabel('S_T_, _G_C/S_L', 'fontAngle', 'italic');
308  % fn = ['ST_SL_', num2str(U), '_', num2str(D), 'mm'];
309  % saveas(gcf, [fn '.fig']);
310  % saveas(gcf, [fn '.png']);
311  % disp('Save workspace');
312
313  % filename = [int2str(D), 'mm_burner_', int2str(P), 'atm_', int2str(T), 'K_
         ', int2str(U), 'mps_', fuel , '_ER0' , num2str( phi * 100 ) ];
314  % save(filename)
315
316  % close all
317
318  % cd('Z:\Flame Speed Data\AbelTransformCodes');
319
320  fprintf('S_T = %5.4f\n',ST)
321
322  save('Calibration.mat','Lf','Rf','Bcrop','Right','Left')
```

C.2   Image Processing Code

```matlab
1   clear
2   clc
3   close all
4
5   %% Add path to functions for calculating laminare and turbulent flame
       speeds.
6   % Not currently used this is left over from GTI−code and will be worked in
7   %
8   Codepath = 'C:\Users\AJ\Google Drive\A Research Folder\GT Burner\
       AbelTransformCodes';
9   Datapath = 'F:\11−24−15';
10  addpath 'C:\Users\AJ\Google Drive\A Research Folder\GT Burner\
       AbelTransformCodes';
11  addpath 'F:\11−24−15';
12  % addpath 'Z:\Chemkin\UnStrainedAnalysis\FlameSpeedandThickness'
13  %
14  bg_path = 'F:\11−24−15\Background.tiff';
15  Cal_path = 'F:\11−24−15\Calibration.tiff';
16  numsamples = 1;
17  numframes = 360*numsamples;                         %Set number of frames from
       camera settings
18  home = pwd;
19
20  fg_tiff_list = dir(strcat(Datapath,'\*f*','.tiff'));        %Generates
       alphabetic list of data files
21
22  for i=1:length(fg_tiff_list)
23      file_name_test{i,1} = fg_tiff_list(i).name;
24  end
25
26  m_dot_total = 0.0024;
27  Density = [.7817 .7817 .7817 .7797 .7797 .7797 .7778 .7778 .7778]; %.7856
       .7856 .7856 .7837 .7837 .7837
28
29  load Calibration
30  % Right = Right;
31  % Left = Left−10;
32  % Bcrop = Bcrop+15;
33
34  for k=1:length(fg_tiff_list)
35  fg_path = strcat(Datapath,'\',fg_tiff_list(k).name);
36      file_name{k} = fg_tiff_list(k).name;
37  % fg_path = 'D:\Users\Public\Documents\GTI burner\DATA\Turbulent Flame Data
       DO NOT DELETE\5−11−15\RE10000_PHI1_A2_POSF10325_1.tiff';
38  % fg_path_1 = 'D:\Users\Public\Documents\GTI burner\DATA\Turbulent Flame
       Data DO NOT DELETE\5−11−15\RE10000_PHI1_A2_POSF10325_1.tiff';
39  % % fg_path_2 = 'D:\Users\Public\Documents\GTI burner\DATA\5−06−15\
       RE10000_PHI1_8.tiff';
40  % % fg_path_3 = 'D:\Users\Public\Documents\GTI burner\DATA\5−06−15\
       RE10000_PHI1_9.tiff';
41  % % fg_path_4 = 'D:\Users\Public\Documents\GTI burner\DATA\5−06−15\
       RE10000_PHI1_10.tiff';
42
43  %% Input Parameters
44  rho_u = Density(k);
```

```matlab
45  D        = 12;                          %Burner Diameter
46  % P       = 20;                         %Some stirng variable input for
        naming convention GTI
47  % T       = 300;                        %Some stirng variable input for
        naming convention GTI
48  % U       = 07;                         %Mean velocity input for naming
        convention GTI
49  phi      = 0.9;                         %Equivalence ratio used in file naming
        convention GTI
50  fuel     = 'Jet-A';                     %String Speciying Fuel used in file
        nameing convention GTI
51  % angle   = [ 0 , 6 , 12 , 18 , 24];    %Angle of turbulence generator will
        call callibration data
52  % expdate = '20130329';                 %Used in naming convention GTI date?
53  % expt    = 'ERSweeps';                 %Used in naming convention GTI type?
54  % runs = [1 2 3 4 5 8];                 %Runs of interest not currently used
55  run_BG = 8;                             %Background Run - Change to string
56
57  %% Laminar Flame data
58  % Need to determine if SL_ref or SL is appropriate talk to Blunck/Niemyer
        about
59  % how to develope database
60
61  % SL =                                  %Something will go here
62
63  %% Image Parameters - Selected From Image
64  % flame_img = imread(Cal_path);
65  % image(flame_img)
66  % colormap('Bone')
67  % zoom on
68  % LZoom = x_zoom(1);
69  % RZoom = x_zoom(2);
70  % BZoom = y_zoom(4);
71  % TZoom = y_zoom(3);
72  %
73  % image(flame_img(BZoom:TZoom,LZoom:RZoom))
74  % colormap('bone')
75  % axis image
76  % [x_flame,y_flame] = ginput(4);
77  % Lf                = x_flame(1);
                                            % left edge of the flame
78  % Rf                = x_flame(2);
                                            % right edge of the flame
79  % Tcrop             = y_flame(4);
                                            % pixel location of the burner
        lip: y-location
80  % Bcrop             = y_flame(3);
                                            % location for cropping of the
        top of the image
81  %
82  % cal_img = imread(Cal_path);
83  % image(cal_img(:,:,1))
84  % colormap('spring')
85  % [x_cal,y_cal] = ginput(2);
86  % Left              = x_cal(1);
                                            % location of left line on
        calibration device
```

```matlab
87  % Right                        = x_cal(2);
                                                % location of right line on
        calibration device
88
89  %% Image Parameters - User Selected
90  %Comment out Lf Rf Bcrop Tcrop Length Right and Left for spacial
91  %calibration determination
92
93  % Lf                           = 392.6872;
                                                        % left edge of the
        flame
94  % Rf                           = 585.9852;
                                                        % right edge of the
        flame
95  % Bcrop                        = 986.9587;
                                                        % location for cropping
           of the top of the   image
96  Tcrop                    = 1;
                                                            % pixel location
           of the burner lip: y-location
97  C                        = (Lf + Rf)/2;                  % center of burner
98  % length                       = 0.787 * 0.0254;
                                                    % length from calibration
        device (cm)
99  diameter                 = 0.0254;
                                                            % use if no
        calibration image
100 % Left                         = 453.3924;
                                                        % location of left line
           on calibration device
101 % Right                        = 520.4875;
                                                        % location of right
        line on calibration device
102 pixels                   = Right - Left;
103 Calibration              = diameter/pixels;
                                                % meters/pixel
104 R                        = 0.008;
                                                        % radial distance (cm)
        from center to crop on left and right side
105
106 %% Preparation and Calibration
107 % Calibration for turbulence generator
108
109 % numRuns                      = length(angle);
                                                    % enter the number of runs
110 % BR                           = 0.9852.*angle + 68.967;
                                        % blockage ratio at each angle
111 %
112 % if D == 12
113 % %     ODm = 13.335e-3;
                                                                % OD of inner
        part of burner lip (m)
114 % %     ODm = 35.56e-3;
                                                            % OD of burner
        lip (m)
115 %     urms                     = ( 0.0029405 .* BR - 0.084321 ) .* U;
                        % urms at each angle
```

```matlab
116  % elseif D == 20
117  % %    ODm = 41.7e-3;
                                                                     % OD of burner
         lip (m)
118  %      urms                 = ( 0.0036 .* BR - 0.1128 ) .* U;
                                  % urms at each angle
119  % else
120  %      error('This is not a recognized burner diameter');
121  % end
122
123  %% Calculate radius and volume flow rate
124  % Change to valumetric flow rate from data
125  % USE MASS FLOW AND UNBURNED DENSITY
126
127  r                           = (D/2)*10^-3;
                                             % burner radius (m)
128  v_dot                       =  m_dot_total/rho_u;%pi*r^2*U;
                                             % volume flowrate (m^3/s)
129
130  %% Image Read In, Average, and Background Subtract
131  % add for loop to repeat for number of runs as needed.
132  info = imfinfo(fg_path);
133  num_images = numel(info);
134  for i = 1:360
135      fg_image(:,:,i) = imread(fg_path,i,'Info',info);
136  %      fg_image(:,:,i+360) = imread(fg_path_2,i,'Info',info);
137  %      fg_image(:,:,i+720) = imread(fg_path_3,i,'Info',info);
138  %      fg_image(:,:,i+1080) = imread(fg_path_4,i);
139      bg_image(:,:,i) = imread(bg_path,i,'Info',info);
140  end
141  MeanImg = sum(fg_image,3)/360;
142  Mean_bg = sum(bg_image,3)/360;
143  BG_sub = MeanImg-Mean_bg;
144  % figure
145  % image(BG_sub)
146  %% Image crop dimensions
147  [ydim, xdim, cases] = size(MeanImg);
148
149  Lcrop                       = floor(C - (1/Calibration)*R);                    %
         location for cropping on left side of image (0.5 cm from OD of burner
         lip)
150
151  if Lcrop < 1
152      error('Cropping domain is larger than actual image');
153  end
154
155  Rcrop                       = floor(C + (1/Calibration)*R);                    %
         location for cropping on right side of image (0.5 cm from OD of burner
         lip)
156  if Rcrop > xdim
157      error('Cropping domain is larger than actual image');
158  end
159
160  ImCrop = BG_sub(ceil(Tcrop):ceil(Bcrop), ceil(Lcrop):ceil(Rcrop));
         % crop the image
161  Intensity = ImCrop;
162  % figure
163  % image(ImCrop)
```

```matlab
164  % axis image
165  %% Axisymmetrize the image by averaging both sides
166
167  Axisym = 0.5*(Intensity(:, 1:end) + Intensity(:, end + 1 - (1:end)));
168  [f, g] = size(Axisym(:, :));                                          %
         get dimensions of the axisymmetrized image
169
170  %% Perform median filter on images
171
172  ImageFilt = Axisym;
173  % for i = 1:numRuns
174      ImageFilt(:, :) = medfilt2(Axisym(:, :), [5 5]);
175  % end
176  %% Extract the centerline intensity of the filtered axisym image
177
178  CL_axisym = zeros(f,1);
179  % for i = 1:numRuns
180      CL_axisym(:,1) = ImageFilt(:, round(g/2));
181  % end
182
183  CL_axisym = flipud(CL_axisym);
184
185  %% Perform the Abel Transform to each image
186
187  ImageAbel = ImageFilt;
188  % for i = 1:numRuns
189      ImageAbel(:, :) = abeltransform(ImageFilt(:, :));
190  % end
191  IA = ImageAbel;
192  %% Create array of centerlines for each Abel transformed image
193
194  CL = zeros(f,1);
195  % for i = 1:numRuns
196      CL(:) = ImageAbel(:, round(g/2));
197      CL = bwfilter(CL, 1 : length(CL), 0.01);
198  % end
199
200  CL = flipud(CL);
201
202  %% Fit Gaussian to each centerline and find maximum location
203
204  GF      = zeros(f,1);
205  H       = zeros(1);
206  ft      = fittype('gauss1');
207  options = fitoptions('gauss1');
208  pxl     = (1:f)';
                                                                % create
         pixel location vector
209  met     = pxl*Calibration;
                                                        % convert pixel
         location vector into meters
210
211  % for i = 1:numRuns
212      curvefit        = fit(pxl, CL(:), ft, options);               %
             create fit model
213      GF(:)           = curvefit(pxl);                              %
             evaluate fit model for pixel vector
```

```matlab
214     [GFmax, I]          = max(GF(:));                                    %
            find the magnitude and location of the maximum value of the
            Gaussian
215 %       GFnorm(:, i)     = GF(:, i)/GFmax;
                                                    % normalize the gaussian by the
        maximum value
216
217     H                = I*Calibration;                                   %
            convert the location of the maximum into meters instead of pixels
218 % end
219
220 %% Calculate flame speeds from H
221
222 s                = (H.^2 + r^2).^(0.5);
223 ConeArea       = pi*r*s;
224 ST(k)              = v_dot./ConeArea;
225 % ST_SL        = ST/SL;
226 % urms_SL      = urms ./ SL;
227 end
228
229 %% Plot
230
231 % newdir = [currdir,'\PlotsAndAnalysis'];
232 % cd(newdir)
233
234 lwidth  = 1.5;
235 fsize   = 14;
236
237 % for i = 1:numRuns
238     figure;
239     set(gcf, 'color', 'w');
240     subplot(1,4,1); imagesc(Intensity(:, :)); axis image; set(gca, '
            FontSize', fsize, 'FontName', 'Times'); title('Cropped');
241     subplot(1,4,2); imagesc(Axisym(:, :)); axis image; set(gca, 'FontSize',
             fsize, 'FontName', 'Times'); title('Axisymmetric');
242     subplot(1,4,3); imagesc(ImageFilt(:, :)); axis image; set(gca, '
            FontSize', fsize, 'FontName', 'Times'); title('Filtered');
243     subplot(1,4,4); imagesc(ImageAbel(:, :)); axis image; set(gca, '
            FontSize', fsize, 'FontName', 'Times'); title('Abel Transformed');
244
245 %     fn = ['Images_', num2str(U), '_', num2str(angle(i)), '_', num2str(D),
        'mm'];
246 %     saveas(gcf, [fn '.fig']);
247 %     saveas(gcf, [fn '.png']);
248     figure;
249     set(gcf, 'color', 'w');
250     plot(100*met, CL, 'r', 100*met, GF, 'b', 'LineWidth', lwidth);
251     set(gca, 'FontSize', fsize, 'FontName', 'Times');
252     xlabel('axial location (cm)');
253     ylabel('Intensity');
254 %     fn = ['Intensity_', num2str(U), '_', num2str(angle(i)), '_', num2str(
        D), 'mm'];
255 %     saveas(gcf, [fn '.fig']);
256 %     saveas(gcf, [fn '.png']);
257 % end
258
259 figure;
260 set(gcf, 'color', 'w');
```

```matlab
261
262  % for  i = 1:numRuns
263        subplot (111); imagesc (ImageFilt (:, :)); axis image; set (gca, 'FontSize'
                , fsize , 'FontName', 'Times'); title ('Axisym');
264  %      subplot (1,numRuns, i); imagesc (ImageFilt (:, :, i)); axis image; set (
          gca , 'FontSize', fsize , 'FontName', 'Times'); title ('Axisym');
265  % end
266
267  % fn = ['AxisymImages_', num2str (U), '_BRSweep_', num2str (D), 'mm'];
268  % saveas (gcf , [fn '.fig ']);
269  % saveas (gcf , [fn '.png ']);
270
271  figure ;
272  set (gcf , 'color ', 'w');
273
274  % for  i = 1:numRuns
275        subplot (111); imagesc (ImageAbel (:, :)); axis image; set (gca, 'FontSize'
                , fsize , 'FontName', 'Times'); title ('Abel Transformed ');
276
277  %      subplot (1,numRuns, i); imagesc (ImageAbel (:, :, i)); axis image; set (
          gca , 'FontSize', fsize , 'FontName', 'Times'); title ('Abel Transformed ')
          ;
278  % end
279
280  % fn = ['AbelImages_', num2str (U), '_BRSweep_', num2str (D), 'mm'];
281  % saveas (gcf , [fn '.fig ']);
282  % saveas (gcf , [fn '.png ']);
283
284  % for  i = 1:numRuns
285        figure ;
286        set (gcf , 'color ', 'w');
287        plot (100*met, CL ./ max( CL), 'r', 'LineWidth', lwidth ); hold on
288        plot (100*met, CL_axisym ./ max(CL_axisym), 'b', 'LineWidth', lwidth );
                hold off
289        set (gca , 'FontSize', fsize , 'FontName', 'Times');
290        xlabel ('axial location (cm)');
291        ylabel ('Intensity ');
292        legend ('Abel Transformed Centerline ', 'Axisym Image Centerline ', '
                FontSize', fsize , 'FontName', 'Times')
293  %      fn = ['IntensityComparison_', num2str (U), '_', num2str (angle (i)), '_
          ', num2str (D), 'mm'];
294  %       saveas (gcf , [fn '.fig ']);
295  %       saveas (gcf , [fn '.png ']);
296  % end
297
298  % figure ;
299  % set (gcf , 'color ', 'w');
300  % plot (urms_SL , ST_SL, 'go', 'LineWidth', lwidth );
301  % set (gca , 'FontSize', fsize , 'FontName', 'Times');
302  % xlabel ('u''_r_m_s / S_L_, _0');
303  % ylabel ('S_T_, _G_C/S_L', 'fontAngle', 'italic ');
304  % fn = ['ST_SL_', num2str (U), '_', num2str (D), 'mm'];
305  % saveas (gcf , [fn '.fig ']);
306  % saveas (gcf , [fn '.png ']);
307  % disp ('Save workspace ');
308
309  % filename = [int2str (D), 'mm_burner_', int2str (P), 'atm_', int2str (T), 'K_
          ', int2str (U), 'mps_', fuel , '_ER0', num2str ( * 100 ) ];
```

```
310  % save ( filename )
311
312  % close  all
313
314  % cd ( 'Z:\Flame  Speed  Data\AbelTransformCodes ') ;
315  for  i = 1: length (ST)
316  fprintf ( 'S_T = %5.4f %s\n' ,ST( i ) , file_name { i })
317  end
318  ST = ST ';
319  file_name = file_name ';
```

Appendix D

Operating Procedures & Conditions

Turbulent Flame Burner

Operational Procedures

Written - Aaron Fillo 4/1/2015
Updated - Jonathan Bonebrake 9/1/2015

1 INTRODUCTION

This document lists the operational procedure for use of the CIRE Lab Turbulent Flame Burner. To ensure safe and correct operation of the turbulent flame burner this procedure should be read in its entirety prior to use. Section 2 details personal protection equipment (PPE) that should be worn during use of the device. Section 3 lists area set up requirements as well as the burner start up procedure. Section 4 provides a detailed discussion of regular system use and data collection. Finally, sections 5 and 6 present the regular and emergency shut down procedures respectively.

2 PERSONAL PROTECTION EQUIPMENT

This section discusses personal protection equipment required during the operation of the turbulent flame burner.

1. Eye Protection in the form of safety glasses or other impact and chemical resisted equivalent with side shields must be worn by all personnel involved in the operation of the device. Personal prescription glasses are acceptable provided they have side shields. Personal sitting at lab desks may choose not to wear eye protection provided they remain outside the operation boundary.
2. Long pants must be worn by those participating in testing.
3. Closed toed shoes must be worn by those participating in testing.
4. Respirators are recommended for highly sooting flames, ie. $\Phi \gg 1$.
5. Hearing protection is recommended but not required.

NOTE: All PPE can be located by the Lab entrance.

3 START-UP PROCEDURE

This section highlights the step by step procedure that must be followed to safely operate the turbulent flame burner.

3.1 AREA SET UP

Area and lab set up is critical to safe operation of the device. This check list must be performed prior to burner start up.

1. [ ] Clean up area immediately around burner and remove any potentially flammable items.
2. [ ] Inform all personnel in lab of pending test and verify they have sufficient PPE.
3. [ ] Turn on all fume hoods.
4. [ ] Verify that main air ventilation is open to supply fresh air to lab.
5. [ ] Open outer door.
6. [ ] Switch "Do Not Enter" sign on.
7. [ ] Close inner door.

3.2 SYSTEM START-UP

This procedure must be followed explicitly for safe operation of the turbulent flame burner. Do not skip or substitute any steps. Changes must be submitted to Dr. Blunck and approved prior to implementation.

1. [ ] Complete area set up procedure
2. [ ] Verify all heaters and thermocouples are wired correctly.
3. [ ] Verify Blast shield is in place.
4. [ ] Start "Turbulent Flame" Lab VIEW VI and verify temperature and pressure readings using secondary thermocouple reader and lab barometric pressure gauge. If necessary re-calibrate DAQ.
5. [ ] Disconnect Ch 2. Thermocouple from base of burner. Note: Flow interlock should be tripped if flow rate is zero.
6. [ ] Verify that Nitrogen purge is engaged.
7. [ ] Reconnect Ch.2 Thermocouple and restart Lab VIEW VI.
8. [ ] Plug in 120 VAC (Black power cord) for heater control board.
9. [ ] Plug in 240 VAC (Yellow power cord) for heater control board.
10. [ ] Turn ¼ turn air supply valve under corner fume hood to start air supply.
11. [ ] Fully open globe valve located above optical table to start air flow to turbulent flame burner.
12. [ ] Adjust primary pressure regulator to 60 PSI.
13. [ ] Verify Flow interlock disengages in VI.
14. [ ] Adjust pilot fuel air rotameter to desired air flow.
15. [ ] Using "Snoop" or "Soap Spray" perform leak check on fittings that have been disconnected since last use. If system has not been used in several days perform full leak check.
16. [ ] Perform leak check on vaporizer and burner gaskets. Tighten as needed.
17. [ ] If leak is found close pressure regulators and main globe valve and repair. If no leaks found proceed.
18. [ ] Using key switch on main power to heater control unit.
19. [ ] Switch silver toggle switches on for all heater control units that will be used during test.
20. [ ] Verify thermocouple reading against thermocouple reader with ambient air probe.
21. [ ] Unplug each thermocouple in turn and verify single led turns off indicating temperature interlock is correctly triggered.

22. [ ] Reconnect all thermocouples.
23. [ ] Beginning with heater 1 power on all heaters in order by flipping red safety toggles.
24. [ ] Allow system to steady state.
25. [ ] Once system has reached stead state conditions fully open valve on top of nitrogen supply and adjust regulator to 60 PSIG.
26. [ ] Retrieve general fuel catch container from flammable liquid storage and connect to fuel return line on lab bench.
27. [ ] Insert fuel draw line into desired fuel tank and place on lab bench.
28. [ ] Power on Isco pump controller and pumps.
29. [ ] Fully open valve on top of Methane supply and adjust regulator to desired pressure.
30. [ ] Adjust pilot air regulator to match methane supply pressure.
31. [ ] Power on MKS controller and initiate Methane flow at desired flow rate.
32. [ ] Open Pilot fuel globe valve to full.
33. [ ] Ignite pilot flame using lighter.
34. [ ] Allow system to regain steady state operation.
35. System is now ready for regular operation.

4   REGULAR OPERATION

During normal operation turbulent premixed flames of liquid fuels requires that both fuel and air be mixed and heated prior to combustion, as a result extreme care must be taken in monitoring flow conditions between the mixing point and combustion zone. If any temperature alarms are tripped during operation proceed immediately to the Emergency procedure in section 6. The following section is split into three parts highlighting data collection and flow rate adjustment for air and fuel respectively. All steps must be followed for safe operation.

4.1   AIR ADJUSTMENT
1. Engage Nitrogen purge.
2. Fully close Fuel Rotameter stopping all fuel flow.
3. Adjust Air flow to desired amount.
4. If Critical Orifices need to be changed the system must be shut down entirely and the orifices changed with all safeties and the system fully purged.
5. Allow system to regain steady state.

4.2   FLAME IGNITION
1. Once system has reached steady state open fuel rotameter valve and adjust flow rate to desired flow rate. If equivalence ratio is greater than 0.5 adjust to 0.5 five for primary ignition.
2. Disengage Nitrogen purge and verify main fuel line ignites with pilot fuel. If ignition does not occur reengage Nitrogen purge and adjust flow conditions (Section 4.2 and 4.3).
3. Raise fuel flow to desired equivalence ratio.

4.3 DATA COLLECTION

4. Record the barometric temperature and pressure from the pressure gauge located on the lab wall above the "Do Not Enter" light switch.
5. Verify the ambient temperature using type K thermocouple probe and thermocouple reader.
6. With Camera directed at flame front trigger camera and Lab VIEW VI simultaneously. Continue recording for desired time.
7. Stop Lab VIEW write data function once camera has stopped recording.
8. Reengage Nitrogen purge.
9. Verify data has saved correctly.
10. Repeat Steps 2-6 a minimum of three times.
11. Adjust turbulence generator as needed.
12. If Fuel or Air adjustments are required for the next data point proceed to sections 4.2 and 4.3.
13. If testing is completed procedure to section 5.

NOTE: DO NOT Alter fuel and air flow simultaneously.

5 SYSTEM SHUT-DOWN

Safe system shutdown is critical to prevent potential damage to the system and avoiding any potential accidents. Follow the listed procedure exactly.

1. [ ] Engage Nitrogen Purge.
2. [ ] Fully close pressure regulator and tank valve on Methane tank.
3. [ ] Fully needle valve at base of fuel rotameter.
4. [ ] Increase Air flow rate to maximum.
5. [ ] Shut down all heaters one by one to avoid potential arch flash.
6. [ ] Once all heaters have been shut off switch off the 240 VAC master switch on the control board.
7. [ ] Depress E-Stop button.
8. [ ] Fully close pressure regulator and tank valve on Nitrogen tank.
9. [ ] Allow system to flow with all heaters disengaged until burner thermocouple registers at 40 °C or below.
10. [ ] Once system has cooled fully close air flow pressure regulators.
11. [ ] Fully close pilot air rotameter valve.
12. [ ] Fully close main air globe valve.
13. [ ] Close ¼ turn main air supply valve.
14. [ ] Unplug 240 VAC line.
15. [ ] Unplug 120 VAC line to heater control system.
16. [ ] Stop Lab VIEW VI and close program.
17. [ ] Purge fuel tank pressure by pulling the "Pop-it" valve located on the lid.
18. [ ] Empty Fuel redirect tank into secondary fuel storage container.
19. [ ] System is now safely shut down.

6 EMERGENCY SHUT-DOWN PROCEDURE

1. If system registers a temperature alarm.
   1. Depress E-Stop
   2. Exit the area.
   3. Once area have been vacated reevaluate and determine if it is safe to reenter.
   4. If reentry is advisable carefully proceed with system shutdown before attempting to determine cause of failure.
2. If System registers a flow alarm.
   1. Depress E-Stop
   2. If caused by operator error in adjusting air supply, increase air supply and continue with normal operation
   3. If cause unknown exit the area.
   4. Once area have been vacated reevaluate and determine if it is safe to reenter.
   5. If reentry is advisable carefully proceed with system shutdown before attempting to determine cause of failure.
3. In the Event of flash back
   1. Depress E-Stop
   2. Exit the area.
   3. Once area have been vacated reevaluate and determine if it is safe to reenter.
   4. If reentry is advisable carefully proceed with system shutdown before attempting to determine cause of failure.
4. In the event of lift off.
   1. Depress E-Stop
   2. Lower fuel and air flow rates
   3. Continue with normal operation
5. Power Failure
   1. Depress E-Stop
   2. Fully close Fuel rotameter needle valve.
   3. Safely proceed with system shutdown.

Turbulent Flame Burner Start-up and Shut-down Procedures

Enter the date and then initial the box for each step after it has been completed.

Date:					

Start up Procedure - Area Set-up

Area and lab set up is critical to safe operation of the device. This check list must be performed prior to burner start up.

1	Clean up area immediately around burner and remove any potentially flammable items					
2	Inform all personnel in lab of pending test and verify they have sufficient PPE					
3	Turn on all fume hoods					
4	Verify that main air ventilation is closed					
5	Open outer door					
6	Switch "Do Not Enter" sign on					
7	Close inner door					

Start-up Pressure System Start-up

This procedure must be followed explicitly for safe operation of the turbulent flame burner. Do not skip or substitute any steps. Changes must be submitted to Dr. Blunck and approved prior to implementation.

1	Verify all heaters and thermocouples are wired correctly					
2	Turn on pressure transducer power supply					
3	Plug in 120 VAC (Black power cord) for heater control board					
4	Verify that heater safety key 2 is in off position, plug in 240 VAC (Yellow power cord) for heater control board					
5	Turn heater controller safety key 1 to on position					
6	Turn heater controller safety key 2 to on position					
7	Pull out E-Stop button					
8	Start "Turbulent Flame" Lab VIEW VI and verify temperature and pressure readings using secondary thermocouple reader and lab barometric pressure gauge. If necessary re-calibrate DAQ by unplugging re-plugging USB cable					

#	Description					
9	Disconnect Ch 2. Thermocouple from base of burner. Note: Flow interlock should be tripped if flow rate is zero					
10	Verify that Nitrogen purge is engaged					
11	Reconnect Ch.2 Thermocouple and restart Lab VIEW VI					
12	Turn ¼ turn air supply valve under corner fume hood to start air supply					
13	Using gloves if system is warm, fully open vaporizer inlet needle valve					
14	Fully open globe valve located above optical table to start air flow to turbulent flame burner					
15	Adjust Premix Air MKS pressure regulator to 50 psig					
16	Adjust Pilot Air MKS pressure regulator to 30 psig					
17	Verify Flow interlock disengages in VI					
18	Adjust pilot fuel air MKS to desired air flow					
19	Turn heater controller safety key 2 to off position					
20	Using soap spray perform leak check on all air fittings					
21	Perform leak check on vaporizer and burner gaskets, and vaporizer inlet needle valve. Tighten as needed					
22	If leak is found close pressure regulators and main globe valve and repair. If no leaks found proceed					
23	Turn heater controller safety key 2 to on position					
24	Switch silver toggle switches on for all heater control units that will be used during test					
25	Verify thermocouple reading against thermocouple reader with ambient air probe					
26	Beginning with heater 1 power on all heaters in order by flipping red safety toggles					
27	Allow system to steady state					
28	Once system has reached steady state conditions fully open valve on top of nitrogen supply and adjust regulator to 60 PSIG					
29	Retrieve general fuel catch container from flammable liquid storage and connect to fuel return line on lab bench					
30	Insert fuel draw line into desired fuel container					

31	Power on Isco pump controller and pumps					
32	Fully open valve on top of Methane supply and adjust regulator to desired pressure					
33	Adjust pilot air regulator to match methane supply pressure					
34	Power on MKS controller and initiate Methane flow at desired flow rate					
35	Open Pilot fuel globe valve to full					
37	Allow system to regain steady state operation					

Shut-down Procedure - System Shut-down

Safe system shutdown is critical to prevent potential damage to the system and avoiding any potential accidents. Follow the listed procedure exactly.

1	Engage Nitrogen Purge					
2	Fully close pressure regulator and tank valve on Methane tank					
3	Fully needle valve at base of fuel rotameter					
4	Increase Air flow rate to maximum					
5	Shut down all heaters one by one					
6	Once all heaters have been shut off, turn heater controller safety key switch 2 to off position					
7	Depress E-Stop button					
8	Fully close pressure regulator and tank valve on Nitrogen tank					
	Turn off methane flow on MKS controller screen					
9	Allow system to flow with all heaters disengaged until burner thermocouple registers at 40 °C or below					
10	Once system has cooled fully close air flow pressure regulators					
11	Fully close pilot air rotameter valve					
12	Fully close main air globe valve					
13	Close ¼ turn main air supply valve					
	Move all heater controller unit switches to off position					
	Turn heater controller safety key switch 1 to off position					
14	Unplug 240 VAC line					
15	Unplug 120 VAC line to heater control system					

16	Stop Lab VIEW VI and close program					
17	Remove fuel draw line from fuel container, and put container in flammables storage					
18	Empty Fuel redirect tank into secondary fuel storage container if more than 1 gallon of fuel is present					

A2	13POSF10325	Jet A
Air Properties @ °C	25	473 K
Density [kg/m^3]	1.184	0.7461
Viscosity [kg/m-s]	0.00001849	0.00002577
Average mol carbon	11.4	
Average mol hydrogen	22.1	
Average Liquid Density @ 15 °C	804	4.086246921
Average MW (g/mol)	158.6	
Average MW Air (kg/kmol)	28.97	
Average Mol Air stoic	16.925	
F/A stoic	0.067954631	
Mixture Viscosity	See Air	0.00002577

Re = 5000

			Fuel	Air		Velocity	Methane Pilot MKS		Air Pilot Rotameter
RE	Phi	F/A	ml/min	SCFM	ρ_u [kg/m^3]	U_o	L/min	ml/min2	Air MM
5000	1	0.0680	5.7666	2.0351	0.7871	13.6427	0.6078	5786.2450	25.1364
5000	0.95	0.0646	5.4957	2.0416	0.7850	13.6779	0.5793	5514.4772	23.6063
5000	0.9	0.0612	5.2231	2.0481	0.7830	13.7133	0.5505	5240.9691	22.0813
5000	0.85	0.0578	4.9488	2.0547	0.7810	13.7489	0.5216	4965.7039	20.5617
5000	0.8	0.0544	4.6727	2.0613	0.7789	13.7847	0.4925	4688.6645	19.0475
5000	0.75	0.0510	4.3948	2.0680	0.7769	13.8208	0.4632	4409.8339	17.5391
5000	0.7	0.0476	4.1151	2.0747	0.7749	13.8571	0.4337	4129.1945	16.0366

Re = 7500

			Fuel	Air		Velocity	Pilot MKS		Pilot Rotameter
RE	Phi	F/A	ml/min	SCFM	ρ_u [kg/m^3]	U_o	L/min	ml/min2	Air MM
7500	1	0.0680	8.6498	3.0526	0.7871	20.4640	1.0485	9981.2726	50.6285
7500	0.95	0.0646	8.2436	3.0624	0.7850	20.5168	0.9992	9512.4732	47.6050
7500	0.9	0.0612	7.8347	3.0722	0.7830	20.5699	0.9497	9040.6717	44.6066
7500	0.85	0.0578	7.4232	3.0820	0.7810	20.6233	0.8998	8565.8392	41.6338
7500	0.8	0.0544	7.0091	3.0920	0.7789	20.6771	0.8496	8087.9463	38.6874
7500	0.75	0.0510	6.5923	3.1020	0.7769	20.7312	0.7991	7606.9635	35.7681
7500	0.7	0.0476	6.1727	3.1120	0.7749	20.7857	0.7482	7122.8605	32.8766

Re = 10000

| RE | Phi | F/A | Fuel | Air | ρ_u [kg/m³] | Velocity | Pilot MKS | | Pilot Rotameter |
			ml/min	SCFM		U_o	L/min	ml/min2	Air MM
10000	1	0.0680	11.5331	4.0702	0.7871	27.2854	1.3980	13308.3635	73.3491
10000	0.95	0.0646	10.9914	4.0832	0.7850	27.3557	1.3323	12683.2977	68.9116
10000	0.9	0.0612	10.4463	4.0962	0.7830	27.4265	1.2662	12054.2290	64.5247
10000	0.85	0.0578	9.8976	4.1094	0.7810	27.4977	1.1997	11421.1190	60.1894
10000	0.8	0.0544	9.3454	4.1226	0.7789	27.5694	1.1328	10783.9285	55.9072
10000	0.75	0.0510	8.7897	4.1360	0.7769	27.6416	1.0654	10142.6179	51.6793
10000	0.7	0.0476	8.2303	4.1494	0.7749	27.7143	0.9976	9497.1473	47.5069

C1	13POSF11498	Gevo ATJ
Air Properties @ °C	25	473
Density [kg/m^3]	1.184	0.7461
Viscosity [kg/m-s]	0.00001849	0.00002577
Average mol carbon	12.6	
Average mol hydrogen	27.2	
Average Liquid Density @ 15 °C	761	4.59896012
Average MW (g/mol)	178.5	
Average MW Air (kg/kmol)	28.97	
Average Mol Air stoic	19.4	18332.38
F/A stoic	0.066723842	27.27414
Mixture Viscosity	See Air	0.00002577

Re = 5000

			Fuel	Air		Velocity	Methane Pilot MKS		Air Pilot Rotameter
RE	Phi	F/A	ml/min	SCFM	ρ_u [kg/m^3]	U_o	L/min	ml/min2	Air MM
5000	1	0.0667	5.9890	2.0374	0.7874	13.6371	0.5975	5688.0002	24.5815
5000	0.95	0.0634	5.7074	2.0438	0.7853	13.6725	0.5694	5420.5531	23.0809
5000	0.9	0.0601	5.4240	2.0503	0.7833	13.7082	0.5411	5151.4225	21.5853
5000	0.85	0.0567	5.1388	2.0567	0.7812	13.7442	0.5127	4880.5925	20.0949
5000	0.8	0.0534	4.8519	2.0632	0.7792	13.7803	0.4840	4608.0471	18.6098
5000	0.75	0.0500	4.5631	2.0698	0.7771	13.8167	0.4552	4333.7698	17.1303
5000	0.7	0.0467	4.2724	2.0764	0.7751	13.8533	0.4262	4057.7440	15.6566

Re = 7500

			Fuel	Air		Velocity	Pilot MKS		Pilot Rotameter
RE	Phi	F/A	ml/min	SCFM	ρ_u [kg/m^3]	U_o	L/min	ml/min2	Air MM
7500	1	0.0667	8.9834	3.0561	0.7874	20.4556	1.0307	9811.8004	49.5304
7500	0.95	0.0634	8.5610	3.0657	0.7853	20.5088	0.9822	9350.4540	46.5703
7500	0.9	0.0601	8.1360	3.0754	0.7833	20.5624	0.9334	8886.2038	43.6346
7500	0.85	0.0567	7.7082	3.0851	0.7812	20.6162	0.8844	8419.0221	40.7238
7500	0.8	0.0534	7.2778	3.0949	0.7792	20.6705	0.8350	7948.8812	37.8386
7500	0.75	0.0500	6.8446	3.1047	0.7771	20.7250	0.7853	7475.7529	34.9798
7500	0.7	0.0467	6.4087	3.1146	0.7751	20.7799	0.7353	6999.6085	32.1479

Re = 10000

			Fuel	Air		Velocity	Pilot MKS		Pilot Rotameter
RE	Phi	F/A	ml/min	SCFM	ρ_u [kg/m^3]	U_o	L/min	ml/min2	Air MM
10000	1	0.0667	11.9779	4.0749	0.7874	27.2741	1.3742	13082.4005	71.7359
10000	0.95	0.0634	11.4147	4.0876	0.7853	27.3451	1.3096	12467.2721	67.3962
10000	0.9	0.0601	10.8480	4.1005	0.7833	27.4165	1.2446	11848.2717	63.1056
10000	0.85	0.0567	10.2777	4.1135	0.7812	27.4883	1.1792	11225.3628	58.8652
10000	0.8	0.0534	9.7037	4.1265	0.7792	27.5606	1.1133	10598.5083	54.6763
10000	0.75	0.0500	9.1261	4.1396	0.7771	27.6334	1.0470	9967.6705	50.5402
10000	0.7	0.0467	8.5449	4.1528	0.7751	27.7066	0.9804	9332.8113	46.4580

C5	15POSF12345	Flat boiling
Air Properties @ °C	25	473
Density [kg/m^3]	1.184	0.7461
Viscosity [kg/m-s]	0.00001849	0.00002577
Average mol carbon	9.7	
Average mol hydrogen	18.7	
Average Liquid Density @ 15 °C	770	3.48851093
Average MW (g/mol)	135.4	
Average MW Air (kg/kmol)	28.97	
Average Mol Air stoic	14.375	
F/A stoic	0.068305451	
Mixture Viscosity	See Air	0.00002577

Re = 5000

			Fuel	Air		Velocity	Methane Pilot MKS		Air Pilot Rotameter
RE	Phi	F/A	ml/min	SCFM	ρ_u [kg/m^3]	U_o	L/min	ml/min2	Air MM
5000	1	0.0683	6.0503	2.0344	0.7856	13.6679	0.6107	5814.2069	25.2946
5000	0.95	0.0649	5.7662	2.0409	0.7837	13.7018	0.5821	5541.2113	23.7562
5000	0.9	0.0615	5.4803	2.0475	0.7817	13.7360	0.5532	5266.4590	22.2228
5000	0.85	0.0581	5.1925	2.0541	0.7797	13.7705	0.5242	4989.9329	20.6948
5000	0.8	0.0546	4.9029	2.0608	0.7778	13.8051	0.4949	4711.6159	19.1724
5000	0.75	0.0512	4.6114	2.0675	0.7758	13.8400	0.4655	4431.4905	17.6557
5000	0.7	0.0478	4.3180	2.0742	0.7739	13.8750	0.4359	4149.5390	16.1450

Re = 7500

			Fuel	Air		Velocity	Pilot MKS		Pilot Rotameter
RE	Phi	F/A	ml/min	SCFM	ρ_u [kg/m^3]	U_o	L/min	ml/min2	Air MM
7500	1	0.0683	9.0754	3.0516	0.7856	20.5018	1.0535	10029.5069	50.9421
7500	0.95	0.0649	8.6493	3.0614	0.7837	20.5528	1.0041	9558.5895	47.9005
7500	0.9	0.0615	8.2204	3.0713	0.7817	20.6041	0.9543	9084.6417	44.8842
7500	0.85	0.0581	7.7888	3.0812	0.7797	20.6557	0.9042	8607.6343	41.8937
7500	0.8	0.0546	7.3544	3.0911	0.7778	20.7076	0.8537	8127.5375	38.9298
7500	0.75	0.0512	6.9171	3.1012	0.7758	20.7599	0.8030	7644.3211	35.9932
7500	0.7	0.0478	6.4770	3.1113	0.7739	20.8126	0.7519	7157.9547	33.0846

Re = 10000

| RE | Phi | F/A | Fuel | Air | ρ_u [kg/m³] | Velocity | Pilot MKS | | Pilot Rotameter |
			ml/min	SCFM		U_o	L/min	ml/min2	Air MM
10000	1	0.0683	12.1006	4.0688	0.7856	27.3357	1.4047	13372.6759	73.8101
10000	0.95	0.0649	11.5324	4.0819	0.7837	27.4037	1.3388	12744.7860	69.3447
10000	0.9	0.0615	10.9606	4.0950	0.7817	27.4721	1.2724	12112.8557	64.9302
10000	0.85	0.0581	10.3851	4.1082	0.7797	27.5409	1.2056	11476.8457	60.5678
10000	0.8	0.0546	9.8059	4.1215	0.7778	27.6102	1.1383	10836.7166	56.2589
10000	0.75	0.0512	9.2229	4.1349	0.7758	27.6799	1.0707	10192.4281	52.0047
10000	0.7	0.0478	8.6361	4.1484	0.7739	27.7501	1.0025	9543.9396	47.8066

Bibliography

[1] UEI Administration, *Oil: Crude and Petroleum Products Explained*, tech. rep. (EIA, Sept. 2014).

[2] C Law, *Combustion Physics*, 1st ed. (Cambridge University Press, New York, 2006), pp. 84–140, 137–138, ISBN: 9780521870528.

[3] *All countries compared for Transport; Road; Motor vehicles per 1000 people*, http://www.nationmaster.com/country-info/stats/Transport/Road/Motor-vehicles-per-1000-people.

[4] X Hui and CJ Sung, "Laminar flame speeds of transportation-relevant hydrocarbons and jet fuels at elevated temperatures and pressures", Fuel **109**, 191–200, ISSN: 00162361 (2013) 10.1016/j.fuel.2012.12.084.

[5] AH Epstein, "Aircraft engines' needs from combustion science and engineering", Combustion and Flame **159**, 1791–1792, ISSN: 00102180 (2012) 10.1016/j.combustflame.2012.02.022.

[6] S Khalilarya and M Javadzadeh, "Developing of a New Comprehensive Spark Ignition Engines Code for Heat Loss Analysis within Combustion Chamber Walls", Thermal Science **14**, 1013–1025 (2010) 10.2298/TSCI10041013K.

[7] AM Briones, B Sekar, D Blunck, H Thornburg, T Erdmann, and DT Shouse, "Reacting Flows in Ultra-Compact Combustors with Combined-Diffuser Flameholder", Journal of Propulsion and Power **31**, 238–252 (2015) 10.2514/1.B35141.

[8]   SR Turns, *An Introduction to Combution Concepts and Applications*, 3rd ed. (McGraw-Hill, New York, 2012).

[9]   D Spalding, *Combustion and Mass Transfer*, 1st ed. (Pergamon, New York, 1979).

[10]   V Katre and S Bhele, "A Review Of Laminar Burning Velocity Of Gases And Liquid Fuels", International Journal of Computational Engineering Research **3**, 33–38 (2013).

[11]   K Kumar, JE Freeh, CJ Sung, and Y Huang, "Laminar Flame Speeds of Preheated iso-Octane/O2/N2 and n-Heptane/O2/N2 Mixtures", Journal of Propulsion and Power **23**, 428–436, ISSN: 0748-4658 (2007) 10.2514/1.24391.

[12]   R Kee, J Grcar, and M Smooke, *A FORTRAN program for modeling steady laminar one-dimensional premixed flame*, Report No. SAND85-8240 (Sandia Nation Laboratories, Livermore, 1985).

[13]   R Kee, F Rupley, and J Miller, *Chemkin-II: A FORTRAN chemical kinetics package for the analysis of gas-phrase chemical kinetics*, Report No. SAND89-8009 (Sandia Nation Laboratories, Livermore, 1989).

[14]   R Kee, G Dixon-Lewis, J Warnatz, M Coltrin, and J Miller, *A FORTRAN computer code package for the evaluation of gas-phase, multicomponent transport properties*, Report No. SAND86-8246B (Sandia Nation Laboratories, Livermore, 1998).

[15]   S Davis and C Law, "Laminar flame speeds and oxidation kinetics of iso-octane-air and n-heptane-air flames", Symposium (International) on Combustion **27**, 521–527, ISSN: 00820784 (1998) 10.1016/S0082-0784(98)80442-6.

[16]   AE Bakali, JL Delfau, and C Vovelle, "Experimental Study of 1 Atmosphere, Rich, Premixed n -heptane and iso-octane Flames", Combustion Science and Technology **140**, 69–91 (1998).

[17]   TJ Held, AJ Marchese, and FL Dryer, "A Semi-Empirical Reaction Mechanism for n-Heptane Oxidation and Pyrolysis", Combustion Science and Technology **123**, 107–146 (1997).

[18] HJ Curran, P Gaffuri, WJ Pitz, and CK Westbrook, "A comprehensive modeling study of iso-octane oxidation", Combustion and Flame **129**, 253–280, ISSN: 00102180 (2002) 10.1016/S0010-2180(01)00373-X.

[19] K Kumar, CJ Sung, and X Hui, "Laminar flame speeds and extinction limits of conventional and alternative jet fuels", Fuel **90**, 1004–1011, ISSN: 00162361 (2011) 10.1016/j.fuel.2010.11.022.

[20] X Hui, AK Das, K Kumar, CJ Sung, S Dooley, and FL Dryer, "Laminar flame speeds and extinction stretch rates of selected aromatic hydrocarbons", Fuel **97**, 695–702, ISSN: 00162361 (2012) 10.1016/j.fuel.2012.02.045.

[21] SH Won, B Windom, B Jiang, and Y Ju, "The role of low temperature fuel chemistry on turbulent flame propagation", Combustion and Flame **161**, 475–483, ISSN: 00102180 (2014) 10.1016/j.combustflame.2013.08.027.

[22] P Venkateswaran, A Marshall, DH Shin, D Noble, J Seitzman, and T Lieuwen, "Measurements and analysis of turbulent consumption speeds of H2/CO mixtures", Combustion and Flame **158**, 1602–1614, ISSN: 00102180 (2011) 10.1016/j.combustflame.2010.12.030.

[23] F Gouldin and RK Cheng, *International Workshop on Premixed Turbulent Flames*, 2010, http://energy.lbl.gov/aet/combustion/workshop/workshop.html.

[24] RK Cheng, "Turbulent Combustion Properties of Premixed Syngas", in *Synthesis gas combustion: fundamentals and applications*, edited by T Lieuwen, Y V., and RA Yetter (Boca Raton, FL, 2009), p. 403.

[25] J DRISCOLL, "Turbulent premixed combustion: Flamelet structure and its effect on turbulent burning velocities", Progress in Energy and Combustion Science **34**, 91–134, ISSN: 03601285 (2008) 10.1016/j.pecs.2007.04.002.

[26] R Borghi, "On the Structure and Morphology of Turbulent Premixed Flames", in *Recent advances in the aerospace sciences* (Springer US, Boston, MA, 1985), pp. 117–138, 10.1007/978-1-4684-4298-4{_}7.

[27] S Hemchandra and T Lieuwen, "Local consumption speed of turbulent premixed flames – An analysis of \memory effects"", Combustion and Flame **157**, 955–965, ISSN: 00102180 (2010) `10.1016/j.combustflame.2009.10.007`.

[28] RK Cheng and D Littlejohn, "Laboratory Study of Premixed H[sub 2]-Air and H[sub 2]–N[sub 2]-Air Flames in a Low-Swirl Injector for Ultralow Emissions Gas Turbines", Journal of Engineering for Gas Turbines and Power **130**, 031503, ISSN: 07424795 (2008) `10.1115/1.2836480`.

[29] H Kobayashi, T Tamura, K Maruta, T Niioka, and Fa Williams, "Burning velocity of turbulent premixed flames in a high-pressure environment", Symposium (International) on Combustion **26**, 389–396, ISSN: 00820784 (1996) `10.1016/S0082-0784(96)80240-2`.

[30] S Verma and AN Lipatnikov, "Does sensitivity of measured scaling exponents for turbulent burning velocity to flame configuration prove lack of generality of notion of turbulent burning velocity?", Combustion and Flame **173**, 77–88, ISSN: 00102180 (2016) `10.1016/j.combustflame.2016.08.018`.

[31] FM White, *Fluid Mechanics*, edited by McGraw-Hill, 6 (McGraw-Hill, 2008) Chap. 5, p. 287, ISBN: 9780072938449.

[32] P Venkateswaran, A Marshall, J Seitzman, and T Lieuwen, "Scaling turbulent flame speeds of negative Markstein length fuel blends using leading points concepts", Combustion and Flame **162**, 375–387, ISSN: 15562921 (2015) `10.1016/j.combustflame.2014.07.028`.

[33] R Xu and H Wang, *Personal communication*, unpublished. (2016).

[34] B Bobbitt, S Lapointe, and G Blanquart, "Vorticity transformation in high Karlovitz number premixed flames", Physics of Fluids **28**, ISSN: 10897666 (2016) `10.1063/1.4937947`.

[35] AY Poludnenko, TA Gardiner, and ES Oran, "Spontaneous transition of turbulent flames to detonations in unconfined media", Physical Review Letters **107**, 1–4, ISSN: 00319007 (2011) `10.1103/PhysRevLett.107.054501`.

[36] A Poludnenko and E Oran, "The interaction of high-speed turbulence with flames: Turbulent flame speed", Combustion and Flame **158**, 301–326, ISSN: 00102180 (2011) 10.1016/j.combustflame.2010.09.002.

[37] P Venkateswaran, A Marshal, J Seitzman, and T Lieuwen, "Turbulent Consumption Speeds of High Hydrogen Content Fuels From 1–20 atm", Journal of Engineering for Gas Turbines and Power **136**, 011504, ISSN: 0742-4795 (2013) 10.1115/1.4025210.

[38] A Soika, F Dinkelacker, and A Leipertz, "Measurement of the resolved flame structure of turbulent premixed flames with constant reynolds number and varied stoichiometry", Symposium (International) on Combustion **27**, 785–792, ISSN: 00820784 (1998) 10.1016/S0082-0784(98)80473-6.

[39] H Wang and MA Oehlschlaeger, "Autoignition studies of conventional and Fischer-Tropsch jet fuels", Fuel **98**, 249–258, ISSN: 00162361 (2012) 10.1016/j.fuel.2012.03.041.

[40] J Wang, M Zhang, Y Xie, Z Huang, T Kudo, and H Kobayashi, "Correlation of turbulent burning velocity for syngas/air mixtures at high pressure up to 1.0MPa", Experimental Thermal and Fluid Science **50**, 90–96, ISSN: 08941777 (2013) 10.1016/j.expthermflusci.2013.05.008.

[41] J Wang, S Yu, M Zhang, W Jin, Z Huang, S Chen, and H Kobayashi, "Burning velocity and statistical flame front structure of turbulent premixed flames at high pressure up to 1.0 MPa", Experimental Thermal and Fluid Science **68**, 196–204, ISSN: 08941777 (2015) 10.1016/j.expthermflusci.2015.04.015.

[42] S Kheirkhah and ÖL Gülder, "Consumption speed and burning velocity in counter-gradient and gradient diffusion regimes of turbulent premixed combustion", Combustion and Flame **162**, 1422–1439, ISSN: 15562921 (2015) 10.1016/j.combustflame.2014.11.009.

[43] P Tamadonfar and ÖL Gülder, "Experimental investigation of the inner structure of premixed turbulent methane/air flames in the thin reaction zones regime", Combustion and Flame **162**, 115–128, ISSN: 15562921 (2015) `10.1016/j.combustflame.2014.07.001`.

[44] P Tamadonfar and ÖL Gülder, "Effects of mixture composition and turbulence intensity on flame front structure and burning velocities of premixed turbulent hydrocarbon/air Bunsen flames", Combustion and Flame **162**, 4417–4441, ISSN: 15562921 (2015) `10.1016/j.combustflame.2015.08.009`.

[45] AS Potturi and JR Edwards, "Large-eddy/Reynolds-averaged Navier-Stokes simulation of cavity-stabilized ethylene combustion", Combustion and Flame **162**, 1176–1192, ISSN: 15562921 (2015) `10.1016/j.combustflame.2014.10.011`.

[46] R Zhou, S Balusamy, MS Sweeney, RS Barlow, and S Hochgreb, "Flow field measurements of a series of turbulent premixed and stratified methane/air flames", Combustion and Flame **160**, 2017–2028, ISSN: 00102180 (2013) `10.1016/j.combustflame.2013.04.007`.

[47] F Wu, A Saha, S Chaudhuri, and CK Law, "Propagation speeds of expanding turbulent flames of C4 to C8 n-alkanes at elevated pressures: Experimental determination, fuel similarity, and stretch-affected local extinction", Proceedings of the Combustion Institute **35**, 1501–1508, ISSN: 15407489 (2015) `10.1016/j.proci.2014.07.070`.

[48] H Kobayashi, K Seyama, H Hagiwara, Y Ogami, and R Aldredge, "Burning velocity correlation of methane/air turbulent premixed flames at high pressure and high temperature", Proceedings of the Combustion Institute **30**, 827–834 (2005) `10.1016/j.proci.2004.08.098`.

[49] Sa Filatyev, JF Driscoll, CD Carter, and JM Donbar, "Measured properties of turbulent premixed flames for model assessment, including burning velocities, stretch rates, and surface densities", Combustion and Flame **141**, 1–21, ISSN: 00102180 (2005) `10.1016/j.combustflame.2004.07.010`.

[50] CJ Lawn and RW Schefer, "Scaling of premixed turbulent flames in the corrugated regime", Combustion and Flame **146**, 180–199, ISSN: 00102180 (2006) `10.1016/j.combustflame.2006.03.010`.

[51] S Daniele and P Jansohn, "Correlations for Turbulent Flame Speed of Different Syngas Mixtures at High Pressure and Temperature", Volume 2: Combustion, Fuels and Emissions, Parts A and B, 1195–1201 (2012) `10.1115/GT2012-69611`.

[52] S Daniele, P Jansohn, J Mantzaras, and K Boulouchos, "Turbulent flame speed for syngas at gas turbine relevant conditions", Proceedings of the Combustion Institute **33**, 2937–2944, ISSN: 15407489 (2011) `10.1016/j.proci.2010.05.057`.

[53] D Bradley, M Lawes, and M Mansour, "Correlation of turbulent burning velocities of ethanol–air, measured in a fan-stirred bomb up to 1.2MPa", Combustion and Flame **158**, 123–138, ISSN: 00102180 (2011) `10.1016/j.combustflame.2010.08.001`.

[54] S Kheirkhah and ÖL Gülder, "Turbulent premixed combustion in V-shaped flames: Characteristics of flame front", Physics of Fluids **25**, 055107, ISSN: 10706631 (2013) `10.1063/1.4807073`.

[55] P Tamadonfar and ÖL Gülder, "Flame brush characteristics and burning velocities of premixed turbulent methane/air Bunsen flames", Combustion and Flame **161**, 3154–3165, ISSN: 00102180 (2014) `10.1016/j.combustflame.2014.06.014`.

[56] G Troiani, F Creta, and M Matalon, "Experimental investigation of Darrieus–Landau instability effects on turbulent premixed flames", Proceedings of the Combustion Institute **35**, 1451–1459, ISSN: 15407489 (2015) `10.1016/j.proci.2014.07.060`.

[57] S Shy, C Liu, J Lin, L Chen, A Lipatnikov, and S Yang, "Correlations of high-pressure lean methane and syngas turbulent burning velocities: Effects of turbulent Reynolds, Damköhler, and Karlovitz numbers", Proceedings of the Combustion Institute **35**, 1509–1516, ISSN: 15407489 (2015) `10.1016/j.proci.2014.07.026`.

[58] A Burluka, R Gaughan, J Griffiths, C Mandilas, C Sheppard, and R Woolley, "Turbulent burning rates of gasoline components, Part 1 – Effect of fuel structure of C6 hydrocarbons", Fuel **167**, 347–356, ISSN: 00162361 (2016) 10.1016/j.fuel.2015.11.020.

[59] P Venkateswaran, A Marshall, J Seitzman, and T Lieuwen, "Scaling turbulent flame speeds of negative Markstein length fuel blends using leading points concepts", Combustion and Flame **162**, 375–387, ISSN: 15562921 (2015) 10.1016/j.combustflame.2014.07.028.

[60] H Kobayashi, Y Kawabata, and K Maruta, "Experimental study on general correlation of turbulent burning velocity at high pressure", Symposium (International) on Combustion **27**, 941–948, ISSN: 00820784 (1998) 10.1016/S0082-0784(98)80492-X.

[61] H Kobayashi, "Experimental study of high-pressure turbulent premixed flames", Experimental Thermal and Fluid Science **26**, 375–387, ISSN: 08941777 (2002) 10.1016/S0894-1777(02)00149-8.

[62] H Kido, M Nakahara, K Nakashima, and J Hashimoto, "Influence of local flame displacement velocity on turbulent burning velocity", Proceedings of the Combustion Institute **29**, 1855–1861, ISSN: 15407489 (2002) 10.1016/S1540-7489(02)80225-5.

[63] M Nakahara and H Kido, "Study on the Turbulent Burning Velocity of Hydrogen Mixtures Including Hydrocarbon", AIAA Journal **46**, 1569–1575, ISSN: 0001-1452 (2008) 10.2514/1.23560.

[64] T Kitagawa, T Nakahara, K Maruyama, K Kado, A Hayakawa, and S Kobayashi, "Turbulent burning velocity of hydrogen–air premixed propagating flames at elevated pressures", International Journal of Hydrogen Energy **33**, 5842–5849, ISSN: 03603199 (2008) 10.1016/j.ijhydene.2008.06.013.

[65] D Littlejohn, RK Cheng, DR Noble, and T Lieuwen, "Laboratory Investigations of Low-Swirl Injectors Operating With Syngases", Journal of Engineering for Gas Turbines and Power **132**, 011502, ISSN: 07424795 (2010) 10.1115/1.3124662.

[66] P Venkateswaran, A Marshall, J Seitzman, and T Lieuwen, "Pressure and fuel effects on turbulent consumption speeds of H2/CO blends", Proceedings of the Combustion Institute **34**, 1527–1535, ISSN: 15407489 (2013) 10.1016/j.proci.2012.06.077.

[67] KHH Goh, P Geipel, F Hampp, and RP Lindstedt, "Regime transition from premixed to flameless oxidation in turbulent JP-10 flames", PROCEEDINGS OF THE COMBUSTION INSTITUTE, ISSN: 1540-7489 (2012) 10.1016/j.proci.2012.06.173.

[68] T Edwards, *Personal communication*, unpublished. (2016).

[69] AD Marshall, JM Seitzman, and TC Lieuwen, "Pressure Effects on the Turbulent Consumption Speeds of High H2 Mixtures", 1–11 (2012).

[70] *13 April NJFCP Fuel Data*, tech. rep. (Federal Aviation Administration, (2013).).

[71] R Xu, D Chen, and H Wang, "Hybrid approach to combustion chemistry of jet fuels", International Combustion Symposium Work in Progress Poster Session (2016).

[72] F Egolfopoulos, *Personal communication*, unpublished. (2016).

[73] D Guyot, F Guethe, B Schuermans, A Lacarelle, and CO Paschereit, "CH*/OH* Chemiluminescence Response of an Atmospheric Premixed Flame Under Varying Operating Conditions", in Volume 2: combustion, fuels and emissions, parts a and b (2010), pp. 933–944, ISBN: 978-0-7918-4397-0, 10.1115/GT2010-23135.

[74] TC Lieuwen, V Yang, and RA Yetter, *Synthesis gas combustion : fundamentals and applications* (CRC Press, 2010), p. 403, ISBN: 9781420085341.

[75] HH Bruun, *Hot wire anemometry : principles and signal analysis* (Oxford University Press, 1995), ISBN: 9780198563426.